Single-Molecule Carbon Nanotube Field-Effect Transistors for Genomic Applications

Scott Marshall Trocchia

Submitted in partial fulfillment of the

requirements for the degree

of Doctor of Philosophy

in the Graduate School of Arts and Sciences

COLUMBIA UNIVERSITY

2018

Abstract

Single-Molecule Carbon Nanotube Field-Effect Transistors for Genomic Applications

Scott Marshall Trocchia

Single-molecule carbon nanotube-based field-effect transistors are promising all-electronic devices for probing interactions of various biological and chemical molecules at the single-molecule level. Such devices consist of point-functionalized carbon nanotubes which are charge sensitive in the vicinity of a generated defect on the nanotube sidewall. Of particular interest is the characterization of the kinetic rates and thermodynamics of DNA duplex formation through repeated association (hybridization) and dissociation (melting) events on timescales unmatched by conventional single-molecule methods. In this work, we study the kinetics and thermodynamics of DNA duplex formation with two types of single-walled nanotubes: CVD-grown and solution-processed. In both assessments, we are able to extract kinetic and thermodynamic parameters governing the hybridization and melting of DNA oligonucleotides. In the latter case, devices are spun onto a wafer surface from an organic suspension, revealing consistent electrical characteristics. Significant effort is made to expand this work to wafer-level, in an effort to make the fabrication manufacturable.

Contents

List of Figures

List of Tables

Acknowledgments

First and foremost, I would like to thank my advisor, Prof. Ken Shepard, for all of his guidance and support over my five-year career at Columbia University. Ken has consistently been available to answer my questions and concerns and has significantly helped to shape my pathway towards graduation. For all of this, I thank him wholeheartedly.

Life as a graduate student would not have been smooth without the companionship and kindness of the members of the Bioelectronic Systems Lab. There are too many names to judiciously recognize in this document, but I want to highlight the contributions of a few distinguished individuals. Thank you immensely to the very talented Shepard Lab CNT team, which has evolved over the years: Charishma Puliyanda, Dr. Sefi Vernick (who has basically worked by my side since day one), Dr. Steven Warren (who I owe immensely for helping me with fabrication and circuit design aspects of my research), Dr. Erik Young, Dr. Yoonhee Lee. Thank you to Dr. David Tsai for HDL coding assistance and to Sid Shekar for inspiring me to code with Python and to use PyQt as my software interface. Thank you to the Shepard lab server admin team (Kevin Tien, Adrian Bradd, Girish Ramakrishnan, Yihan Zhang) for maintaining our servers and software packages and for keeping them afloat.

Thanks to my collaborators in the Nuckolls lab – Hasti Amiri, Delphine Bouilly, and Yan Feng – and in the Gonzalez Lab - Nathan Daly and Jason Hon - of the Chemistry department. Without you guys, many parts of this Ph.D. would have seemed insurmountable. Having bright chemists working alongside me truly expedited many of the developments which came about in the past few years.

Thank you to Professor Ruben Gonzalez, who took the time out of his schedule to hear me gripe (at times) about some confusing measurements I had collected. Ruben was gracious enough to assist me in these circumstances and provide some very helpful insight. Professor Colin Nuckolls was also instrumental in helping me develop strategies to tackle challenging aspects of my thesis project, so I thank him kindly for all of his enthusiasm and input.

I credit my parents and my sister for their moral support and inspiration.

A special thank you goes to my fiancée, Melissa, who understood that obtaining a Ph.D. is an arduous journey, but one can muscle through it by remaining strong and persevering.

Chapter 1

Introduction & Background

1.1 Single-walled Carbon Nanotubes

Single-walled carbon nanotubes (SWCNTs) are hollow cylinders which are considered to be tubular 1–D nanomaterials with a unit cell of carbon atoms arranged hexagonally. They are highly touted for their unique set of chemical, electrical, mechanical, and optical properties and have intrigued the scientific community since the early 1990's when they were first discovered by Japanese scientist Iijima [1]. SWCNTs have high aspect ratios, measuring many millimeters long yet only a few nanometers (0.8–2 nm, typically) in diameter [2]. Ten times stronger than steel and five times more thermally conductive than copper (they can tolerate temperatures close to 2800 °C) [3], these nanomaterials truly have the potential to alter technological innovation. Essentially rolled up sheets of graphene, a 2–D allotrope of carbon with disparate properties for a wide range of application spaces, nanotubes contain one shell through which electron/hole conduction occurs. In their native or pristine state, the C–C bonds are sp^2 hybridized, containing three electrons per carbon atom which are shared with an adjacent atom and one delocalized (out-of-plane) π electron [4, 5, 6], giving rise to the extraordinary electrical conductivity for which CNTs are famous.

Carbon nanotubes can be uniquely characterized by a chiral index vector, which

essentially correlates to the amount of twisting of the hexagonal carbon lattice:

$$C_h = na_1 + ma_2 = (n, m)$$

where a_1 and a_2 are the corresponding unit vectors in Figure 1.1b and (n, m) are the integral chiral vector indices [6]. These indices also translate to a specific CNT diameter, expressed by the equation:

$$d = \frac{\sqrt{3}}{\pi} a_{cc} \sqrt{(n^2 + m^2 + nm)}$$

where a_{cc} is the distance between atoms of a single sp^2 C–C bond (1.42 Å) [4].

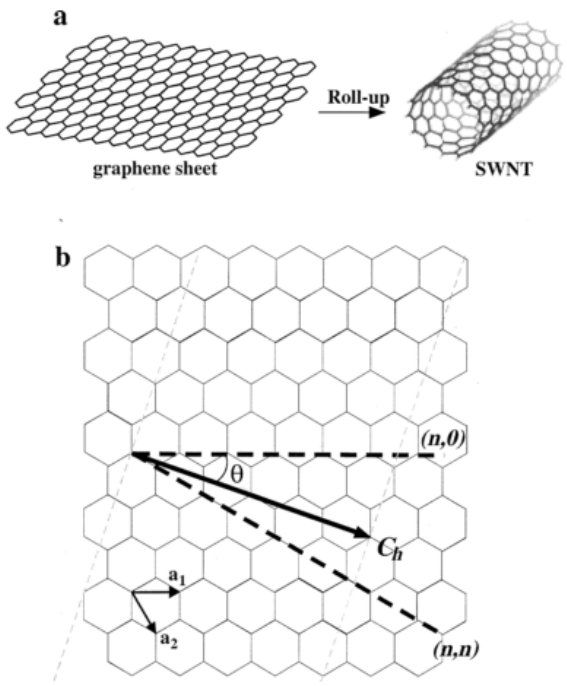

Figure 1.1: a) Schematic depicting rolling a graphene sheet into a single-walled CNT. b) Chiral vectors overlaid on the characteristic hexagonal (honeycomb) carbon lattice. Referenced from [7].

1.1.1 Basic Electrical Properties

Despite the wide spectrum of application spaces in which SWCNTs are useful, only the electronic properties of carbon nanotubes and their feasibility as sensor elements are highlighted in this thesis. Unsurprisingly, an understanding of the fundamental electronic properties of SWCNTs would be incomplete without considering those of graphene, due to their similar

lattice structures. Carbon nanotubes come in two flavors, in terms of electrical transport mechanisms: metallic and semiconducting. Metallic tubes are characterized by a chiral vector for which the absolute value of the difference between n and m is an integer multiple of three [7], i.e. $|n - m|$ modulo $3 = 0$. For all other index pairs, the nanotube is semiconducting by nature. Unlike graphene, semiconducting SWCNTs have an intrinsic energy bandgap inversely proportional to their diameter d, as predicted from a tight-binding model of their band structure: $E_g \approx 0.7$ eV·nm/(d in nm) [8]. Nanotube electronic properties can be further binned into three categories: armchair (n=m≠0), zigzag (n,0), and chiral (n,m). All armchair nanotubes are metallic since they always obey the mathematical relationship governing their chirality. Zigzag nanotubes, on the contrary, may be either metallic or semiconducting, as evidenced in Figure 1.2a.

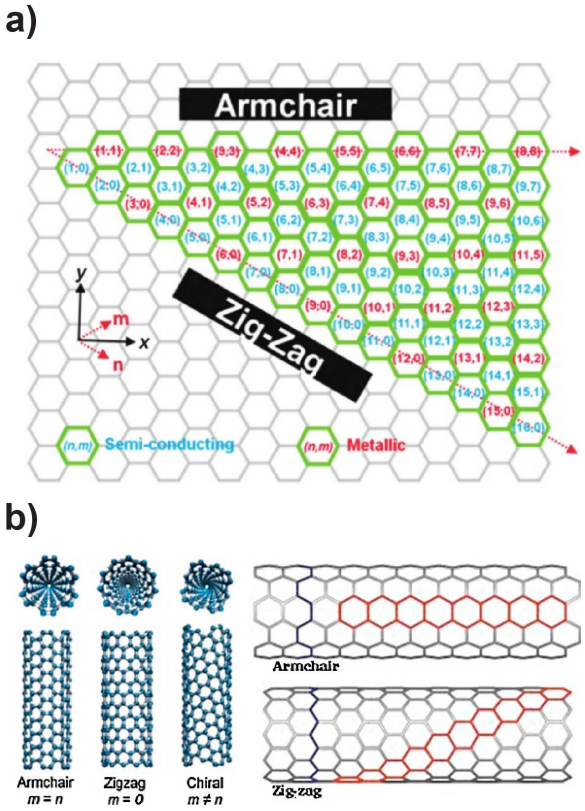

Figure 1.2: Armchair, zigzag, chiral nanotubes. (a) map of chiral indices superimposed on the CNT unit cell. Adapted from [9]. (b) One representative example of an armchair nanotube, one of a zigzag nanotube, and one of a chiral nanotube, each with different (n,m) pairs. Referenced from [10].

1.2 CNTFET Biosensors

Owing to their small diameter and ease of chemical functionalization, SWCNTs are excellent candidates for incorporation in electronic sensors. The majority of biosensing with carbon nanotubes today is ensemble sensing, in which many nanotubes operate in parallel or many functionalization sites are created along a single nanotube. The functionalization process involves the use of spacer or linker molecules on the CNT sidewalls which attach to tethered molecules capable of interacting with target analytes in liquid. More details of various functionalization strategies are provided in subsection 1.2.1.

In particular, electronic biosensors based on a field-effect transistor (FET) topology for the detection of a given target analyte are fascinating. From detection of protein binding [11] to label-free DNA hybridization [12], this sensing modality has been comprehensively explored [10,13]. To form the FET, source and drain metal electrodes are connected to one or more SWCNTs (the organic channel material), as shown in Figure 1.3a. The devices are either back-gated through a conductive substrate like doped Silicon or through an aqueous (DI-based) or organic electrolyte contacting the top of the devices. The latter type of device generally uses an exposed-gate (where the dielectric is the water or organic solvent, rather than a solid insulating layer such as PMMA or HfO_2) so that the nanotubes can undergo chemical functionalization. One such example of this sensing scheme is depicted in Figure 1.3b, where a carbon nanotube is functionalized with a linker compound to which antibodies are affixed. These antibodies, tethered in many locations along the length of the nanotube, are sensitive to specific antigens introduced in a buffer solution. This sort of highly specific binding renders a change in the conductance through the nanotube (between the source and drain electrical contacts) which can be monitored in real-time. In such ensemble studies, non-specific adsorption to the substrate or CNT sidewall of target analytes presents a tangible challenge, which can convolute the electronic signal being collected. Furthermore, charge noise from the interaction of the SWCNT with charge traps in the underlying substrate or with polymer residues (from lithography processing steps or from adsorbates to the sidewall) appears in real-time signals [14]. Oftentimes, to mitigate this

issue, SWCNTs are coated with a blocking layer, such as PEG or a PEG-like derivative [12].

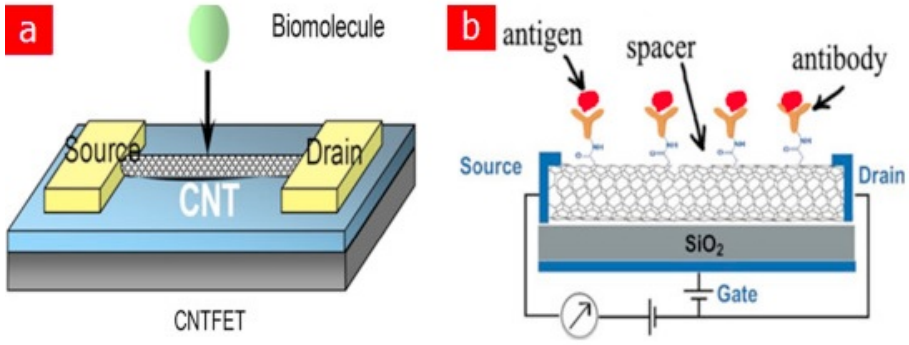

Figure 1.3: a) A carbon nanotube situated between source and drain electrodes on a conductive substrate. The nanotube is able to interact with biomolecules since the device is not top-gated. b) A carbon nanotube functionalized for the detection of antigen-antibody binding. A back-gate voltage is applied to the substrate. Additionally, a source-drain voltage is applied while the current flowing through the nanotube channel is monitored. Referenced from [10].

Note that multi-walled carbon nanotubes (MWCNTs) have also been utilized as ensemble biosensors, but such devices are not discussed here (due to their incompatibility with single-molecule sensing architectures).

1.2.1 Functionalization Strategies

Many chemical functionalization techniques have been highlighted for single-walled carbon nanotubes [15, 16]. Three are commonly reported: electrochemical oxidation, diazonium attachment, and pyrene attachment. These strategies, illustrated in Figure 1.4, can be further binned into two categories: covalent (electrochemical, diazonium) and non-covalent attachment (pyrene) [17]. With all three techniques, the objective is to immobilize biological moieties to the nanotube sidewall; the type of moiety can be tailored by altering the linker group.

Electrochemical Oxidation

In this approach, oxidative defects are introduced on the nanotube sidewall, to which biological moieties can be directly tethered. The native sp^2 orbitals of one or more carbon

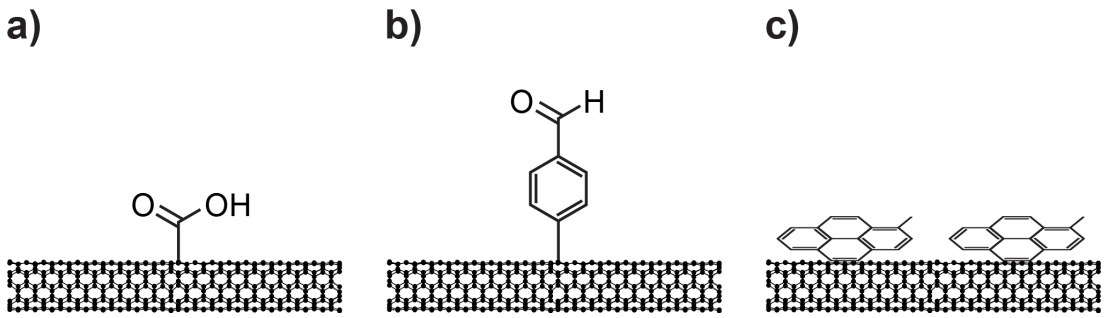

Figure 1.4: Covalent and non-covalent attachment chemistries for CNTs. Covalent: a) electrochemical oxidation with carboxylic acid (-COOH) functional group depicted, b) diazonium attachment with aldehyde (-CHO) functional group. Non-covalent: c) pyrene attachment with generic pyrene molecule.

atoms are disrupted and rearranged to form sp^3 hybridized orbitals. Electrochemical oxidation can be attained with strong acids by modulating oxidation potentials, such that the reaction rate and behavior can be both controlled and monitored in real-time [18].

Diazonium Attachment

Reactions of SWCNT with aryl diazonium salts have been widely studied [19,20,21], making them one of the most convenient routes for CNT covalent functionalization. The introduction of the diazonium molecule disrupts the sp^2 hybridization, which is to be expected from a covalent attachment chemistry. The reaction of the diazonium salt with the SWCNT proceeds through a two-step process – selective adsorption, mediated by electron transfer from the nanotube to the diazonium salt, followed by a covalent reaction which results in localization of electrons and formation of an impurity state at the Fermi level [22]. A second (albeit similar) reaction mechanism is proposed by Wilson et al., whereby a radical is first formed, followed by covalent reaction resulting in sp^3 hybridization. [23].

Pyrene Attachment

In a competing attachment chemistry, functional groups adhere to the nanotube sidewall through van der Waals interactions. A popular molecule for such attachment is pyrene, an aromatic hydrocarbon which is commensurate with the chemical structure of the nanotube and is able to cling to the CNT sidewall through pi-pi stacking [24]. This has the advantage

of not disrupting the molecular hybrid orbitals, therefore maintaining the CNT electronic properties. Pyrene comes in many forms, a few of which are pyrene-NHS ester (optimal for protein tethering [24]), pyrene-maleimide (for DNA polymerase [25] and single-molecule protein engineering studies [26], and pyrene-biotin (for glucose sensing [27]).

Summary of Attachment Types

	Pros	Cons
Covalent		
Electrochemical oxidation	Can be monitored in real-time, has local charge sensitivity	Difficult to generate only a few defect sites (the reaction on one carbon atom tends to promote more atoms to react), hardly reproducible
Diazonium attachment	Controllable, reproducible, has local charge sensitivity	High reactivity, radical reactions are evident
Non-covalent		
Pyrene attachment	Pyrene can be washed away if two-state signal is not collected	Prone to detaching over time from the CNT surface, SNR impact is low

Table 1.1: Comparison of advantages and disadvantages of discussed functionalization strategies

Ultimately, only covalent attachment chemistry with diazonium salt is used in this thesis, since it is more long-lasting compared to non-covalent methods. The ability to record real-time conductance signals for multiple smFET devices over many days is crucial to evolving our understanding of single-molecule dynamics.

1.3 Single-molecule Methodologies - FRET versus FET

In a simple unidirectional chemical reaction, reactant A reacts to form product B:

$A \rightarrow B$. In the characterization of an ensemble population, the concentration of the reactant

A exponentially decays while the concentration of the product B exponentially increases (to a certain finite level). This behavior is depicted in Figure 1.5a. At t = ∞, the rate dependence of the concentration decay/increase of the average number of molecules N can be extracted [28]:

$$< N_A(t = \infty) >= \frac{1}{k_{A\to B}} \tag{1.1}$$

$$< N_B(t = \infty) >= \frac{1}{k_{B\to A}} \tag{1.2}$$

where $k_{A\to B\ (B\to A)}$ denotes the transition from state A to B and B to A, respectively.

Conversely, single-molecule data is characterized by dwell times in states A and B (Figure 1.5b) which are exponentially distributed. If one measures a single-molecule for long enough, i.e. at infinite time, the average dwell times yield rate constants which are analogous to Equations 1.1 and 1.2 [28]:

$$< t_A >= \frac{1}{k_{A\to B}} \tag{1.3}$$

$$< t_B >= \frac{1}{k_{B\to A}} \tag{1.4}$$

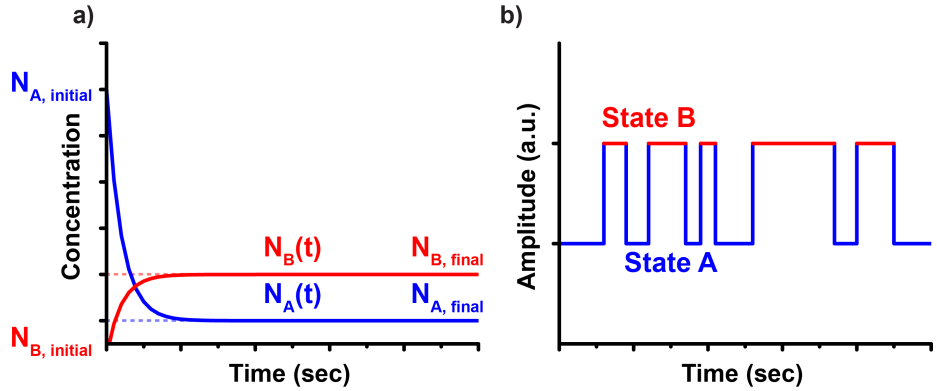

Figure 1.5: Cartoon of a) exponential decay for ensemble populations and b) bistable trajectory for single molecules.

Single-molecule studies are important for revealing biochemical dynamics and functionalities which are otherwise obscured at an ensemble level. For instance, regarding nucleic

acids, single-molecule experiments allow probing the conjugate kinetic processes of association (hybridization) and dissociation (melting) of two single-stranded oligonucleotides at equilibrium. This type of analysis is not possible with ensemble studies.

1.3.1 smFRET

Of all the techniques presently available for probing single-molecule interactions, single-molecule Förster Energy Resonance Transfer (smFRET) is arguably the most prevalent in academia [29]. Conventionally, single-molecule methods rely on fluorescence-based measurements in which optical photons are converted into fluorescent intensities. In these studies, a single molecule is bound to a surface. Upon illumination with incident light, energy transfer occurs between two excited fluorophores attached to this molecule, the donor fluorophore (transmitting energy) and the acceptor fluorophore (receiving energy). The transfer efficiency is directly proportional to the intensity ratio of the acceptor (I_A) to the donor (I_D), and inversely proportional to the distance R between them:

$$E_{FRET} = \frac{I_A}{I_A + I_D} = \frac{1}{(R/R_0)^6}$$

with R_0 being the distance which results in half of the maximum E_{FRET} [29]. Despite the merits of this methodology, it tends to produce low current levels – due to the intrinsic losses associated with transducing optical photons – and operate over small bandwidths – due to the long integration times required for obtaining high signal fidelity. Acceptable bandwidths for smFRET studies are around 1 kHz [30]. smFRET setups tend to be bulky, occupying a large space on a bench-top due to the multitude of optical equipment required [31].

1.3.2 smFET

Recently, in the last half of a decade, there has been significant interest in using carbon nanotube-based sensors, laid out in a field-effect transistor configuration, for sensing single-molecule biomolecules (largely DNA [32] and proteins [26, 33] and chemical redox reaction dynamics [34]. The devices employed in these methods are referred to as single-molecule carbon nanotube field-effect transistors (smFETs). Such transducers, which have emerged

as the ideal all-electronic, label-free single-molecule sensing element, are characterized by a conductance that is sensitive to charges localized within a few Debye lengths of a sidewall chemical functionalization of the SWCNT. This site of point-functionalization serves as the anchor site for a single SWCNT-tethered probe molecule under study. The system is depicted in Figure 1.6. In the smFET configuration, each device is biased with the same liquid gate voltage V_g or V_{lg} (relative to the source terminal of each measured CNT), while each source and drain voltage may vary.

In the case of DNA, this system permits electronic readout of hybridization and melting kinetics and thermodynamics. The concentration is determined by capture (hybridization) kinetics, whereas the melting process is primarily concentration-independent. Under a source-drain voltage bias of 100 mV, the baseline current signal level of a typical smFET device is tens of nA, at least six orders of magnitude higher than analogous detection levels ($\sim$1 fA) from smFRET measurements with charge-coupled image sensors (CCDs) [35]. These signal levels enable high bandwidth measurement capabilities when the device is suitably optimized to limit parasitic capacitance and when it is tightly coupled to underlying measurement electronics [34].

In comparison to bulk ensemble measurements, in which case the relevant signal information is encoded in the signal amplitude, a smFET encodes information temporally. This gives rise to a digital signal which manifests itself as random telegraph noise (RTN) in the time domain. As a result, single-molecule experiments are much more informative [29, 36]. Signal amplitudes can vary as long as there is sufficient signal-to-noise-ratio (SNR) contrast between the conductance states of the system. Moreover, these devices are not susceptible to the non-specific adsorption plaguing ensemble sensors, since the dominant scattering site is localized on the SWCNT sidewall.

The main requirements for an smFET device are two-fold: high transconductance ($g_m = \frac{\partial I_{ds}}{\partial V_{gs}}$) or gain, and spatial localization of this gain in a confined area. High transconductance is relevant for transducing the presence or absence of a target biomolecule to high electrical signal levels on the order of many nanoamperes. Spatial localization is relevant

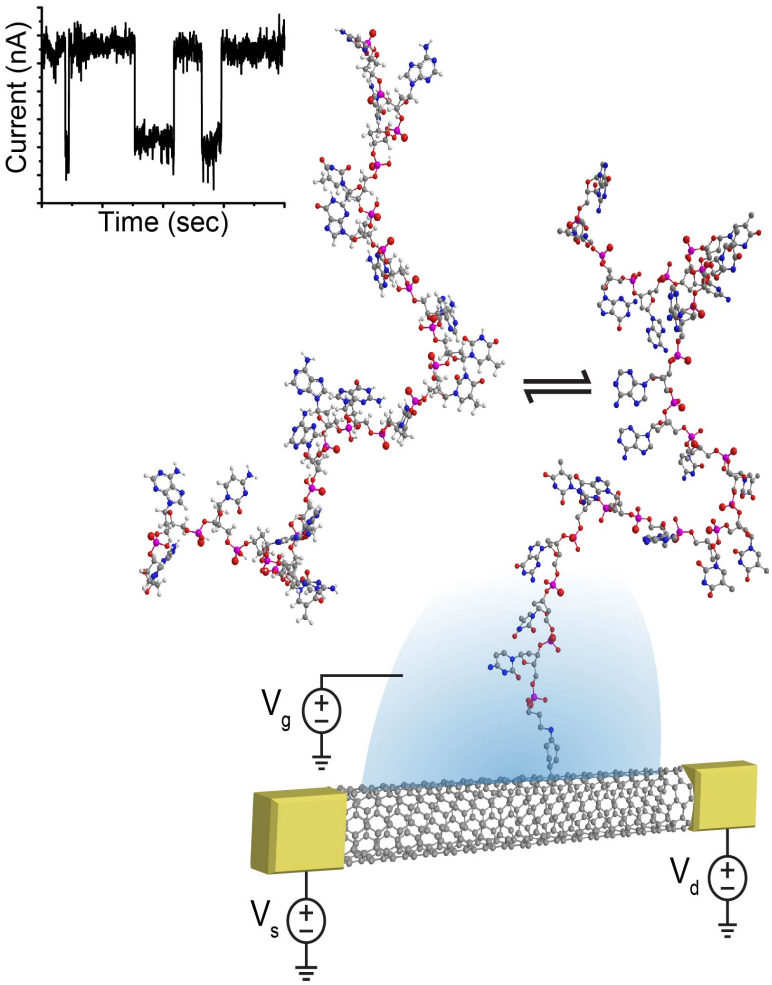

Figure 1.6: The smFET topology depicting DNA hybridization/melting of a 20-mer target oligonucleotide from its complementary tethered strand. The electrolyte solution is drawn as a semicircular color gradient near the nanotube sidewall. The oligos are drawn with the proper number of bases using ChemDraw.

because the biomolecules should be comparably sized (a few nm's) to the defect site generated on the CNT sidewall. The resulting device has dramatically higher sensitivity, capable of detecting a single molecule due to coulomb interactions between the molecule and the defect which modulates scattering in the 1–dimensional nanotube channel.

The smFET, being a device governed by electrostatics, is affected by the Debye length in an electrolyte. The Debye length, given by the following equation, defines the length limit at which the potential in the vicinity of the nanotube surface goes to zero:

$$\lambda_D = \sqrt{\frac{\epsilon_r \epsilon_0 k_B T}{2 N_A e^2 I}} \tag{1.5}$$

where ϵ_r is the relative dielectric constant of the electrolyte medium, k_B is Boltzmann's constant, T is the temperature in Kelvin, N_A is Avogadro's number, e is the elementary charge in Coulombs, and I is the ionic strength (related to the salt concentration). This equation is valid for monovalent electrolytes, which only contain salt ions with either 1+ or 1– charge. Notice that there is an inverse proportionality between the Debye length and the square root of the ionic strength. Assuming prototypical aqueous phosphate buffers (43 mM, $\epsilon_r = 80$, pH 8.0) such as those used in the studies in Chapters 3 and 4, the ionic strength is 80 mM, giving a Debye length at room temperature (25 °C) of 1.09 nm.

1.4 Carbon Nanotube Deposition Approaches

SWCNTs, such as those used in the studies in Chapter 3, are typically grown via catalyst-enhanced chemical vapor deposition (CVD), a method in which long nanotubes (on the order of mm to cm [37]) grow from a catalyst area at high temperatures (many hundreds of degrees Celsius). Alternatively, nanotubes can be cast from a suspension. In one deposition approach, nanotubes suspended in a solvent (aqueous or organic) are randomly spun on a wafer surface (refer to Figure 1.7 for an illustration and to Chapter 4 for more details). Using a variation of the solution-based tactic, dielectrophoresis (DEP) [38, 39, 40] is exploited to generate high local electric fields between pre-patterned electrode pairs, precisely manipulating and aligning individual or groups of SWCNTs suspended in an electrolyte between them (Figure 1.8).

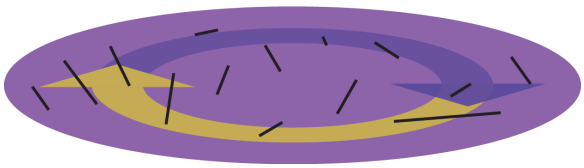

Figure 1.7: Cartoon representing spin-on deposition approach for SWCNTs.

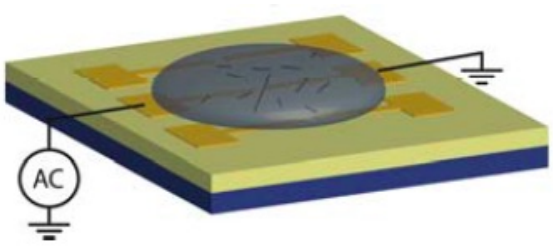

Figure 1.8: Dielectrophoresis with an AC applied voltage. Adapted from [41].

1.5 Outline of This Thesis

This thesis presents a real-time electronic measurement and monitoring platform for single-molecule genomic applications. To better understand the mechanisms behind the hybridization and melting of DNA duplexes, studying single-molecule nucleic acid systems is of critical importance. For such studies, two types of nanotubes – CVD-grown and spin-cast – are experimented with.

Chapter 2 provides a run-through of the measurement electronics and associated software.

Chapter 3 introduces the concept of electrostatically-driven melting and compares it against the conventional Arrhenius model.

Chapter 4 talks about optimization and characterization of spin-cast single-walled CNTs to be used as smFET transducers.

Chapter 5 presents conclusions and future work.

Chapter 2

Measurement Electronics

To enable the real-time measurement of many individual smFET devices in tandem, custom-made testbenches have been constructed. A printed circuit board (PCB) capable of simultaneously acquiring data from 11 uniquely addressable device channels was designed by a colleague, Steven Warren. While the PCB contains active, commercial-off-the-shelf (COTS) electronic components, the chips which interface with it are passive, merely consisting of fabricated metal wires routing from each carbon nanotubes to bond pads. In contrast, integrated circuits can be manufactured in a complementary metal-oxide semiconductor (CMOS) foundry, in which case the nanotubes are integrated in close proximity to active electrode arrays. Applications utilizing such arrays have been demonstrated previously [34, 42], yet are beyond the scope of this work.

Eventually, the previously mentioned real-time measurement platform was extended, leading to a system capable of interrogating up to 58 electrode pairs, each potentially containing a single carbon nanotube sensor. The increase in device count is advantageous for a number of reasons. For one, a richer set of statistics can be collected with larger sample sizes. A proper understanding of how each device behaves electrically is paramount. Secondly, the yield of functional devices – that is, devices which are properly functionalized with diazonium salt and contain an attached biomolecule – is expected to be low. Increasing the sample size is beneficial.

Before beginning a comprehensive overview of the current measurement platform, it is worthwhile to consider the bandwidth constraints and measurement parasitics which impact the system-level design.

2.1 Electrochemical Impedance Spectroscopy of Titanium Electrode

For smFET studies, metal electrodes will be immersed in an electrolyte solution. One should comprehend the electrochemical properties of the electrode metal (titanium (Ti), in this case) in the electrolyte before incorporating the nanotube transducer. For this purpose, it is customary to perform electrochemical impedance spectroscopy (EIS) measurements. This method provides insight into the reaction of salt ions at the metal interface, which can crudely be described with standard circuit elements (resistors and capacitors). In the simplest use case, frequency-dependent impedance data is fit to the well-known Randles model [43], shown in Figure 2.1. The model consists of three components: the series solution resistance, which is usually small for highly conductive electrolytes; the parallel interfacial resistance, which is typically large due to the lack of charge transfer between the electrode and the solution; the parallel double-layer capacitance, which characterizes a thin (single nm) charged layer formed at the interface of the working electrode (e.g. the carbon nanotube and metal electrode connections) and the solution.

An ideal capacitor, with a perfect impermeable dielectric, has an impedance described by $\mathrm{Z}_C = |Z_C|\angle Z_C = \frac{1}{\omega C} e^{-j90^\circ}$. In practice, the double-layer capacitance does not behave in a truly capacitive manner – in other words, the phase angle is not strictly 90 degrees. To compensate for this behavior, a phenomenological factor α ($0 < \alpha < 1$) is often introduced. This new element, referred to as a constant phase element (CPE), has an impedance governed by electrochemical properties rather than purely electrical qualities. The CPE accounts for non-idealities of a dielectric layer (such as water) in an electrolytic environment. The impedance of the CPE is $\mathrm{Z}_{CPE} = |Z_{CPE}|\angle Z_{CPE} = \frac{1}{\omega^\alpha Q_0} e^{-j\alpha 90^\circ}$, where

α is the factor which models capacitive non-idealities, and $Q_0 = \frac{1}{|Z_{CPE}|}$ at f = $\frac{1}{2\pi}$ Hz [44]. Neither Q_0 nor α depend on frequency. If α equals 0, the dielectric is purely resistive; at the other extremity, if α equals 1, the dielectric is purely capacitive.

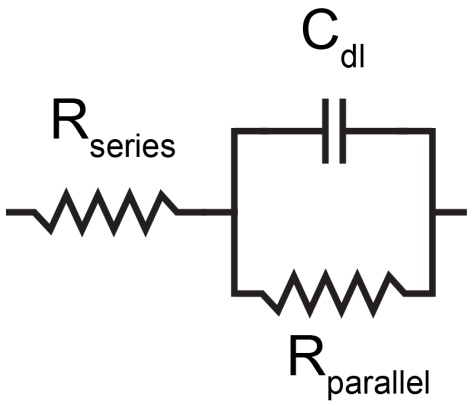

Figure 2.1: The Randles model, depicting solution resistance in series with the parallel combination of the double-layer capacitance and an interfacial resistance.

Impedance measurements for a fabricated Ti electrode, measuring 8 mm long × 20 μm wide, were taken as a function of frequency, shown in Figure 2.2. The solution resistance, R_{series}, is negligible. The interfacial resistance, $R_{parallel}$, is high-impedance (exceeding 100 MΩ), while the shunt capacitance, C_{dl}, is 2.4 nF. This capacitance denotes the series combination of the double-layer capacitance in the electrolyte and the capacitance of the oxide layer which natively forms on Titanium. This oxide layer is very thin and TiO_2 has a high dielectric constant ≈80, yielding a large capacitance. Hence, a valid assumption is that the parallel capacitance is roughly equivalent to C_{dl} (hereafter called C_{sol}). Above 1 kHz, the lumped capacitive element has an impedance below 66 kΩ, three orders of magnitude lower than the interfacial resistance. This observation indicates that the solution is mostly capacitively coupled to the electrode surface.

For the data shown in Figure 2.2a, the magnitude of the impedance is roughly capacitive (slope ≈ –1 on a log-log scale) at low frequencies, and only begins to deviate >1 kHz. In the high-frequency regime (1 kHz – 100 kHz), a CPE should be used to represent the impedance, as evidenced by the deviation from 90° phase angle for the fitted curve in Figure 2.2b at ∼5 kHz.

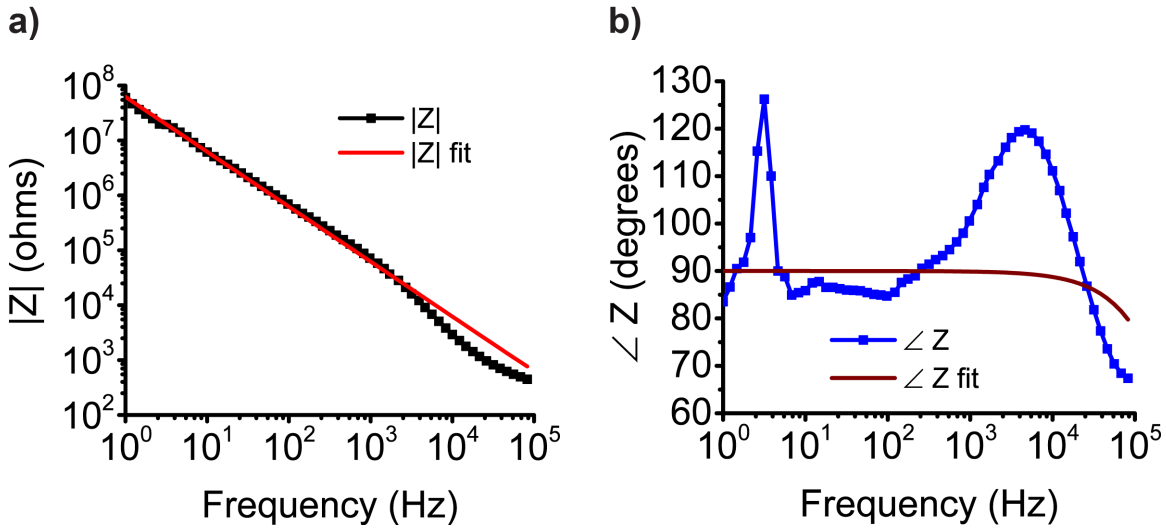

Figure 2.2: EIS magnitude and phase angle as a function of frequency (1 Hz – 100 kHz).

2.2 Measurement Parasitics

Other parasitics besides the solution capacitance impact the acceptable signal bandwidth. Particularly, the parallel-plate oxide capacitance is an important quantity. In standard silicon wafer processing, silicon oxide is grown epitaxially to a thickness of a few hundreds of nm, resulting in fairly low coupling capacitance to the substrate. This geometric capacitance is defined as $C_{ox} = \frac{\epsilon_r \epsilon_0 A}{d}$, where ϵ_r is the relative dielectric constant of the silicon oxide (3.9), A is the area of the metal contact electrodes, and d is the thickness of the oxide layer. In the studies presented in Chapters 3 and 4, wafers with 285 nm of oxide are used, yielding capacitance from electrodes measuring 15 μm wide by 4–8 mm long to the substrate of 7.3–14.5 pF. The lower bound of the length range indicates the electrode length (from the bond pad to the end of the electrode) used in spin-cast SWCNT fabrication in Section 4.3; the upper bound indicates the length used in fabrication with CVD-grown CNTs, as described in Section 3.2.1. Notably, $C_{sol} >> C_{ox}$, especially for thin (nm scale) oxide layers and large (hundreds of μm^2) electrodes contacting the electrolyte.

The metal electrode resistance represents another parasitic component. Below are DC and small-signal (AC) models of the electrode connections to the CNT and the front-end amplifier (Figures 2.3a and b, respectively). The diagram of the small-signal configuration

shows that the parallel RC combination of the parasitic electrode resistance (calculated to be ∼5 kΩ from a DC two-terminal measurement) and the total input capacitance (mostly influenced by the solution capacitance) is relevant. Thus, there exists a dominant low-frequency pole: $f_{3-dB} = \frac{1}{2\pi R_{Ti} C_{sol}}$. The value of this pole, 15.9 kHz, is three times higher than the signal bandwidth of interest, 5.3 kHz. For this PCB design, anti-aliasing filters constructed in hardware restrict the signal bandwidth to DC – 5.3 kHz.

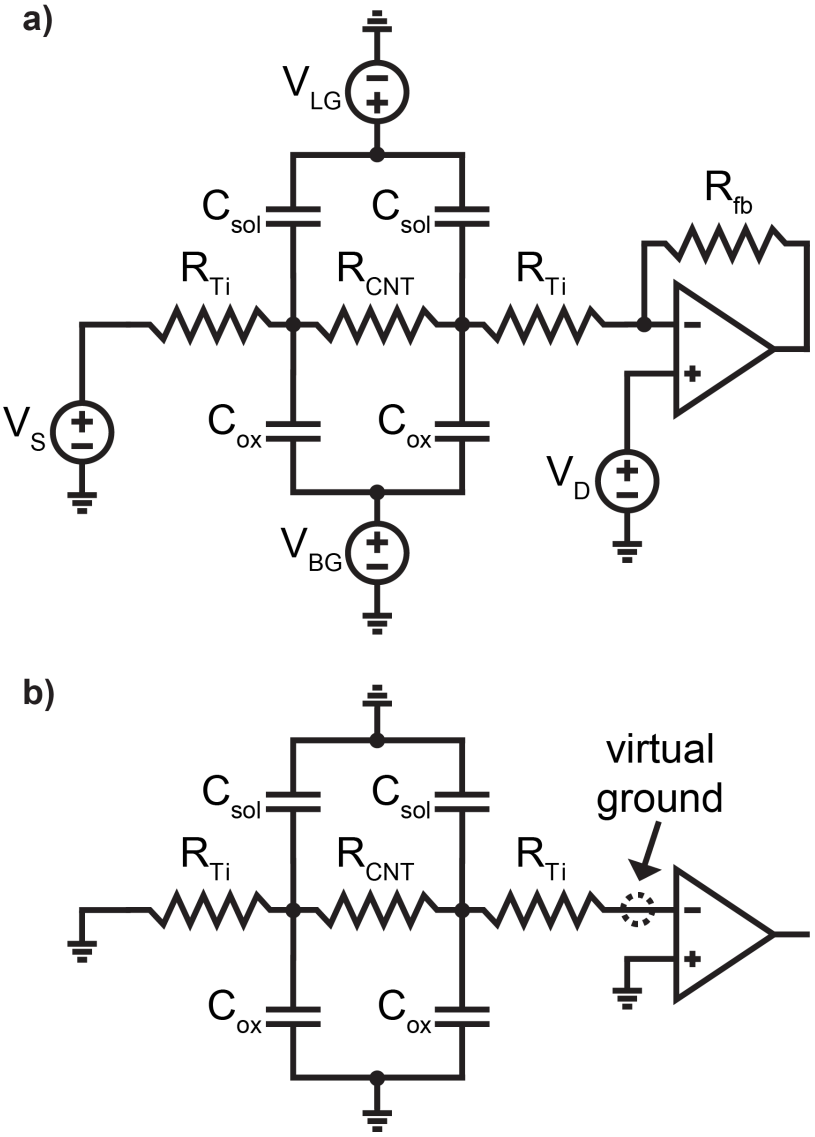

Figure 2.3: Measurement circuit parasitics. a) large-signal (DC) and b) small-signal (AC) circuits for electrode, solution, and oxide parasitics.

2.3 Hardware

With the aforementioned system constraints in place (e.g. permissible bandwidth and parasitics), we can conceive a real-time multiplexed measurement platform for measuring electrical current from individually addressable device channels. We limit the number of channels to 58 due to chip packaging design choices. Currently, fabricated chips are wirebonded to custom ball-grid-array (BGA) packages containing 232 pins (58 pins per side) on the periphery. The custom-made packages interface with the corresponding socket via pogo pins, obviating the need for BGA re-balling. Since only use left and right fingers of the BGA are routed on the PCB, the device count is capped.

High-level features of the PCB are as follows. Each of 64 signal chains incorporates tunable drain and source potentials controlled via independent digital-to-analog converters (DACs) and is composed of two gain stages: a front-end transimpedance amplification stage with a fixed resistive gain of 1 MΩ, followed by an inverting voltage amplifier with variable gain from 2 to 200 V/V, which is set by digitally-controlled potentiometers. A separate DAC is employed to control the potential of the conductive electrolyte gating the nanotubes. Each channel furthermore utilizes a second-order active filter topology, limiting the signal bandwidth to ∼5 kHz. Readings from each channel are sampled at a rate of 25 kSps, affording temporal resolution of 40 μs. The hardware-software interface is controlled by an Opal Kelly XEM6010 FPGA module, which connects to multiplexers, decoders, and analog-to-digital converters (ADCs) on the PCB and to the PC through a USB 2.0 connection. On the FPGA, large built-in memory (128 MB) and smaller FIFOs (4 kbytes) are used to buffer chunks of data before pushing it to the PC.

The PCB contains only off-the-shelf passive elements (resistors and capacitors), analog ICs, and digital ICs. In total, 897 components were soldered. Figures 2.4 and 2.5 show photographs of the finalized circuit board. The PCB is double-sided, a design decision which was made to accommodate all components in a reasonable sized (8.5" wide × 8.1" tall) area.

Figure 2.6 displays a full block diagram for the PCB. Front-end IC components

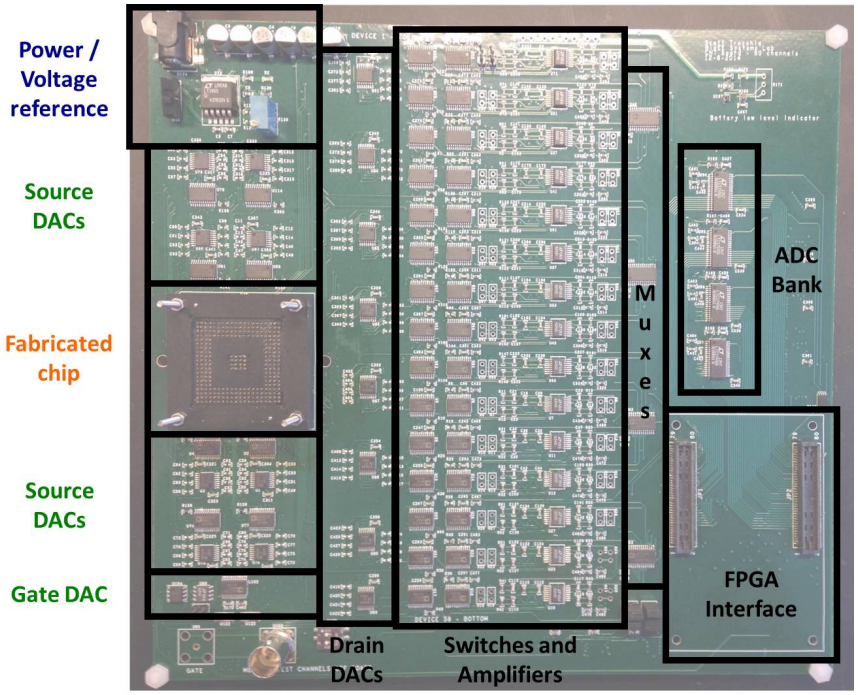

Figure 2.4: Photograph of the assembled circuit board for simultaneous, multiplexed CNT measurements, with sections highlighted.

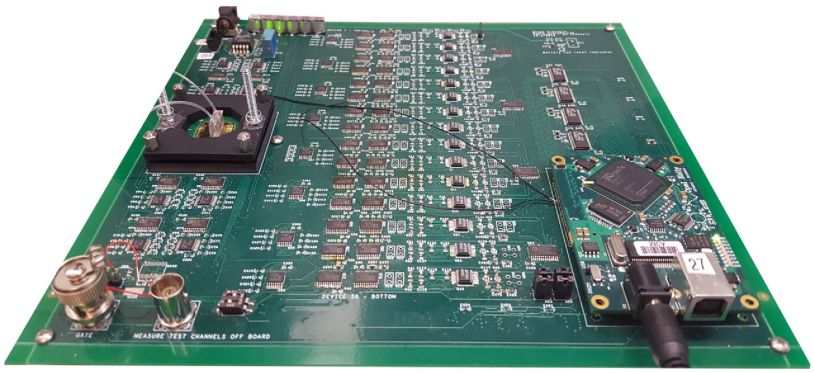

Figure 2.5: Angled view of the assembled circuit board with fabricated chip inserted into the testing socket, microfluidics (detailed in Section 3.4), power connections, and mounted FPGA.

include switches connected to each CNT, distinct source and drain DAC lines, and the TIA. The second stage cascades to the TIA output. Sixteen signal chains feed one multiplexer (MUX)-ADC combination. There are four of these, giving a total of 64 independent measurement channels.

Component Name	Component Value
R_{fb}	1 MΩ
C_{fb}	30 pF
R_1	1 – 100 kΩ
R_2	200 kΩ
C_2	150 pF
R_{AA}	200 Ω
C_{AA}	1 nF

Table 2.1: Passive component values for each signal path.

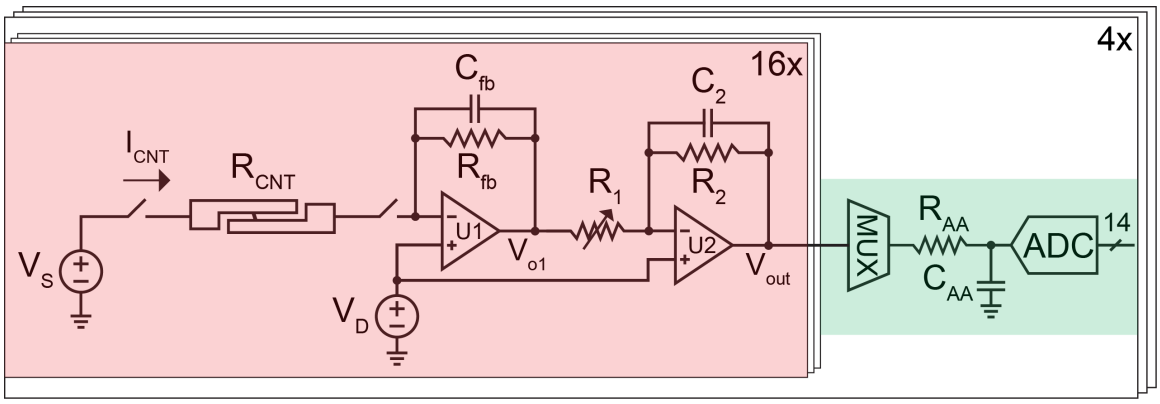

Figure 2.6: Full block diagram for PCB.

We will now dissect each PCB block.

2.3.1 Signal Path

The signal path circuitry is color-coded light red in Figure 2.6.

Front-end Circuitry: Transimpedance Amplification

Transimpedance amplifiers (TIAs) compose the front-end circuitry. Each TIA converts electron/hole currents I_{CNT} from individual CNTs into measurable voltages through a feedback network around operational amplifier U1 in Figure 2.6. Assuming the CNT is predominantly a p-type device, the current direction indicated by the I_{CNT} arrow in Figure 2.6 agrees with the conventional signal direction for a p-type silicon MOSFET.

The transimpedance gain V_{o1}/I_{CNT} is equal to the magnitude of the impedance of the feedback network, Z_{fb}, which is typically complex and has the form $R_{fb} \parallel C_{fb}$. The feedback capacitor serves to stabilize the poles of the amplifier. The resistive feedback gain (R_{fb}) of each TIA is 1 MΩ, consistent with previous iterations of the electronic recording platform for single-molecule CNT studies. The value for C_{fb} must abide by the following equation related to stability [45]:

$$C_{fb} > \frac{1}{4\pi R_{fb} GBW}\left[1+\sqrt{1+8\pi R_{fb} C_{in} GBW}\right] \approx \sqrt{\frac{C_{in}}{2\pi R_{fb} GBW}} \tag{2.1}$$

where C_{in} is the total input capacitance present at the input terminals of the TIA and GBW is the gain-bandwidth product of the amplifier. The approximation is true for large $R_{fb}\,C_{in}\,GBW$ products. For the values given in Table 2.1, C_{in} = 6.5 pF, and GBW = 18 MHz, the feedback capacitance must exceed 244 fF. The feedback capacitor for each TIA was chosen to be 30 pF, thus satisfying the stability requirements. This capacitor serves a second purpose: in parallel with the feedback resistance, this passive RC combination creates a first-order pole at 5.3 kHz, restricting the signal bandwidth in turn.

The particular model of U1 was chosen because it can accommodate rail-to-rail outputs and is powered with a single-supply (V_{DD} = 5 V). Quad op amps (two dedicated to each channel, one for the front-end TIA and one for the second stage voltage amplification) are used to reduce the PCB footprint. Each signal chain contains dedicated and tunable digital-to-analog converters (DACs) for altering the source, V_S, and drain, V_D, biases of each channel. Octal DAC ICs are used due to space constraints. In normal operation, V_D is held at mid-rail (e.g. 2.5 V) to permit the most signal swing between V_{DD} and ground.

Second Stage: Voltage Amplifier with Variable Gain

The second op amp stage of each signal chain amplifies the output voltage V_{o1} of the transimpedance stage by an adjustable closed-loop voltage gain, controlled by external resistors R_1 and R_2. Op amp U2 is configured as a non-inverting amplifier with input resistance R_1, which operates as a digitally-controlled potentiometer with programmable values between 1 kΩ and 100 kΩ (the terminal resistance). The feedback resistor, R_2, is fixed at 200 kΩ; thus, the DC gain of the second stage can vary from 2 to 200 V/V, inclusive. This stage also provides low-pass filtering to incoming signals due to the inclusion of a 150 pF capacitor (C_2) in parallel with R_2 in the feedback loop, yielding a cutoff frequency of 5.3 kHz.

Cascaded Stages

Having propagating through the cascaded stages – TIA followed by voltage amplifier – input current signals present at the TIA are low-pass filtered at $f_{cutoff} = 5.3$ kHz with a roll-off of 40 dB/decade. The closed-loop gain of the cascaded amplifiers, which is the product of the transimpedance gain Z_{fb} and the closed-loop gain $\frac{Z_2}{R_1}$ of the inverting amplifier itself, can be effectively tuned between 2 and 200 MΩ, allowing for a wide range of current levels to be acquired and resolved. As shown in Figure 2.7, the DC gain degrades by a factor of $\sqrt{2}$ once the cutoff frequency is reached.

Noise Implications

Noise analyses of certain elements of each signal chain provide insight into the minimum detectable analog signals. In the subsequent analyses, one should assume that:

- An individually isolated single-walled nanotube conducts 1 nA under 100 mV source-drain bias (meaning that the CNT's DC resistance is 100 MΩ) is exposed to aqueous electrolyte and is connected to the signal path
- The DC closed-loop gain of the signal path is 200 MΩ

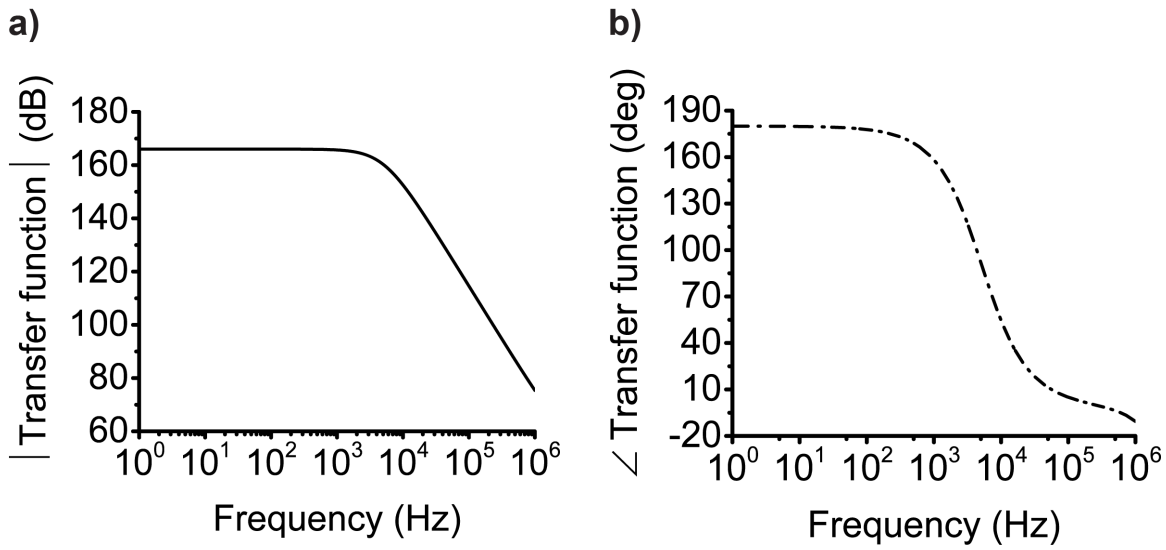

Figure 2.7: Simulated closed-loop gain transfer function magnitude (panel a) and phase (panel b) for the cascaded amplifiers comprising each signal chain.

- The 'on' resistance and parasitic capacitance of the switches are irrelevant
- DC leakage currents from any circuit element are negligible

Regarding the two cascaded amplifier stages, three voltage noise sources (units: $V/\sqrt{Hz}$) are pertinent: the spectral voltage noise e_{n1} of the TIA op amp (in series with the gate of the FET at the positive input terminal), the spectral voltage noise e_{n2} of U2 (in series with the gate of the FET at the positive input terminal), and the spectral voltage noise $e_{n,\,drain\ DAC}$ of a single DAC (present at the positive terminal of both op amps in the signal path). Other spot noise sources are apparent, including the voltage noise $e_{n,\,source\ DAC}$ of DAC connected to the source side, input current noise i_n to both U1 and U2, and resistor Johnson (white) noise $\sqrt{4k_BTR}$, but under the assumptions established earlier, their contributions to the output noise are insignificant.

Figure 2.8 shows the circuit used for noise analysis of the full signal path, with DC sources included. Noise contributions are calculated for each of the aforementioned spectral noise sources individually, i.e. with all other noise and DC sources nullified.

Uncorrelated noise from e_{n1} generates a corresponding noise current across the op amp input capacitance, the electrolyte capacitance, and the CNT resistance. From e_{n1}

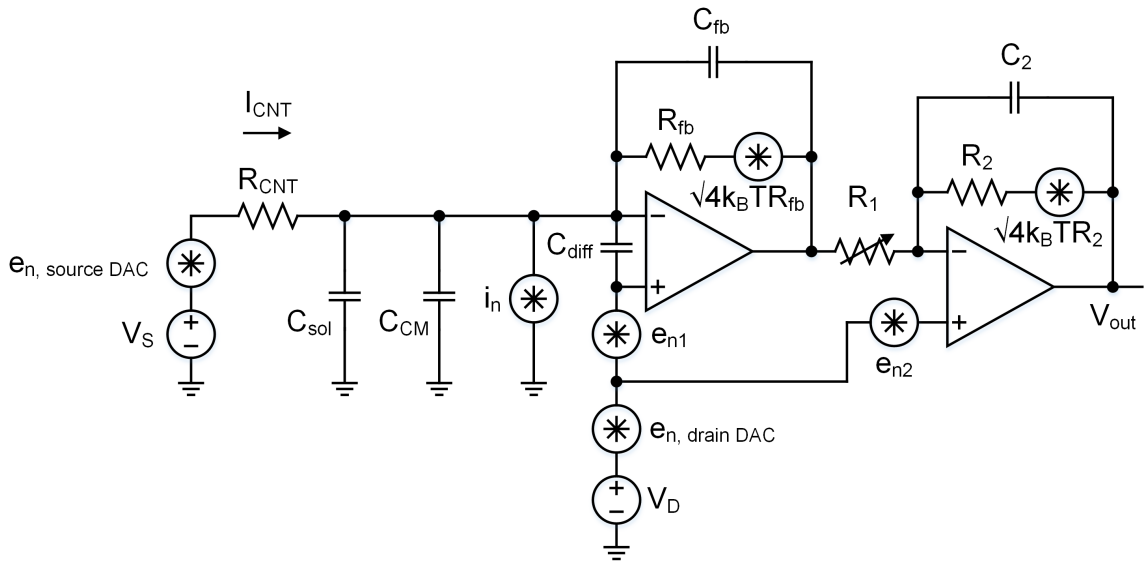

Figure 2.8: Full signal chain with associated noise sources.

to V_{out}, the noise propagates through both amplifier feedback loops, according to this expression:

$$\left|\frac{V_{out}}{e_{n1}}\right| = (1 + \frac{Z_{fb}}{Z_{IN}})(\frac{Z_2}{R_1}) \tag{2.2}$$

This transfer function is the product of the noise gain (NG $= 1 + \frac{Z_{fb}}{Z_{IN}}$) of the TIA stage and the closed loop gain of the inverting amplifer. Z_{fb} is the TIA feedback impedance, $R_{fb} \,||\, C_{fb}$. Z_{IN} is the input impedance; considering all of the capacitive elements tied to the negative input node,this is $R_{CNT} \;||\; [C_{CM} + C_{diff} + C_{sol}]$). The input capacitance of one op amp is 3.5 pF differentially and 3.5 pF in common mode, and the solution capacitance was quantified earlier. The dominant capacitive element is the solution capacitance (i.e. $C_{sol} >> [C_{CM} + C_{diff}]$). Z_2 is the complex feedback impedance of the voltage amplifier, $R_2 \,||\, C_2$.

From e_{n2} to the output node, the noise voltage only sees the inverting gain of the second stage; any noise originating from the TIA is nullified since its input terminals are shorted to ground:

$$\left|\frac{V_{out}}{e_{n2}}\right| = \frac{Z_2}{R_1} \tag{2.3}$$

From $e_{n,\ drain\ DAC}$ to the output node, the noise voltage is also dependent upon the impedances of both feedback loops, as evidenced by the transfer function:

$$\left|\frac{V_{out}}{e_{n,\ drain\ DAC}}\right| = \left|1 - \frac{Z_{fb}Z_2}{Z_{IN}R_1}\right| \approx \left|\frac{Z_{fb}Z_2}{Z_{IN}R_1}\right| \tag{2.4}$$

Given the values listed in Table 2.1, the magnitude of the transfer function (TF) from each independent noise source to the output node V_{out} is verified by circuit simulations (AC analysis). This information is conveyed in Figure 2.9.

At a specific frequency, the total noise present at V_{out} is computed by summing the uncorrelated noise contributions in quadrature:

$$\sqrt{(e_{n1} \cdot |TF_{e_{n1}}|)^2 + (e_{n2} \cdot |TF_{e_{n2}}|)^2 + (e_{n,\ drain\ DAC} \cdot \left|TF_{e_{n,\ drain\ DAC}}\right|)^2} \tag{2.5}$$

The values for e_{n1} and e_{n2} are equal to the spot noise specified in the quad op amp datasheet (7 nV/$\sqrt{Hz}$), and the value for $e_{n,\ drain\ DAC}$ is equal to the voltage noise density of a single DAC in the octal IC package (120 nV/$\sqrt{Hz}$). It is clear from Figure 2.9 that both e_{n1} and $e_{n,\ drain\ DAC}$ dominate the noise present at the output node of the amplifier chain, with $e_{n,\ drain\ DAC}$ representing the predominant noise source due to its large spectral value and transfer function magnitude.

It is convenient to express noise in terms of input-referred quantities since one can directly compare the magnitude of the input signal (current in nA, in this circumstance) to the input noise. To convert, one divides the output voltage noise by the magnitude of the cascaded closed-loop gain (previously plotted versus frequency in Figure 2.7a), giving an input-referred current noise 6.1 pA/$\sqrt{Hz}$ at f_{ENB} = 4.06 kHz. This frequency represents the the equivalent noise bandwidth (ENB), which is equal to $1.22 \cdot f_{3-dB}$ for a two-pole filter. Integrated over ENB, this noise density equates to an input noise current of 240 pA_{RMS}. Because only low bandwidth (much lower than the GBW of either op amp), band-limited signals will pass through each signal chain, and DC signal levels of individually isolated single-walled CNTs are expected to be at least 2x the thermal noise floor, the noise penalties are not detrimental to the overall system performance.

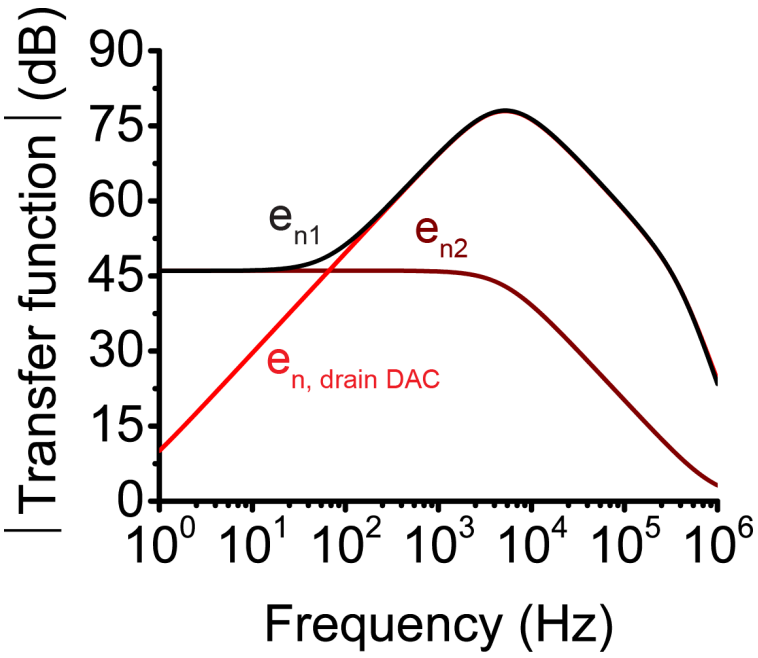

Figure 2.9: Magnitude of the spectral noise transfer function for three uncorrelated spectral noise sources. The analyzed circuit includes parasitic solution capacitance. Square boxes indicate the magnitude at the signal bandwidth upper limit (5.3 kHz).

In the absence of the electrolyte, the parasitic input capacitance reduces to 6.5 pF. Then, the input-referred current noise is 8.3 pA_{RMS} over ENB. It is no longer proper to ignore the Johnson noise $\sqrt{4k_BTR_{fb}}$ of the large feedback resistor R_{fb}, which now contributes the most noise since the TIA noise gain approaches one; recall that this gain exceeded 50 when considering the solution capacitance. Shown in Figure 2.10 is a comparison of the output spectral noise with and without solution capacitance. The RMS voltage is lower in the latter case, indicative of diminished noise gain.

2.3.2 Multiplexed Data Acquisition

The data acquisition circuitry is colored light green in Figure 2.6. Sixteen device channels, each representing the output from one signal chain, route to one 16-to-1 analog MUX. This configuration is instanced four times in order to accommodate the voltage signals from all 64 signal paths. The first 58 channels are used for sensing CNT devices, while the last six channels are designated for testing and debugging.

The output from each of the four anti-aliasing passive filters is DC-coupled to a

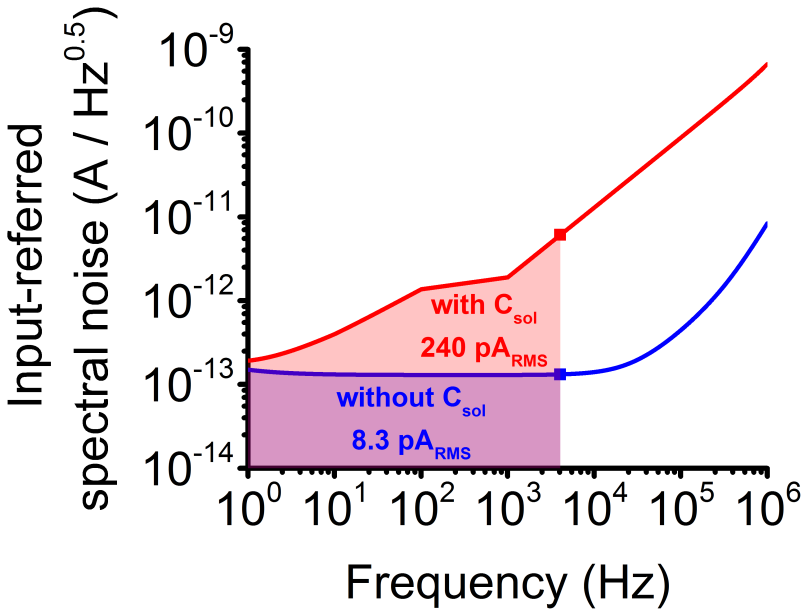

Figure 2.10: Total input-referred spectral noise with (red color) and without (blue color) including C_{sol} in the measurement circuit. The RMS current is calculated by integrating the output spectral density over ENB. Colored squares represent the input-referred spot noise at f_{ENB}.

dedicated sample-and-hold (S/H) pipelined ADC with 14-bit resolution and parallel digital output lines, affording signal resolution of 305 μV (with V_{DD} = 5 V). In comparison, a 1 nA SWCNT signal will generate a 2 mV voltage output from the signal chain if the smallest (worst-case) closed-loop gain (2 MΩ) is used.

Between each multiplexer and its corresponding ADC, an anti-aliasing filter (comprised of R_{AA} and C_{AA}) is employed to attenuate signals with frequency components exceeding the small-signal bandwidth of the ADC's S/H circuitry. Resistor and capacitor values of the anti-aliasing filter are chosen to mitigate device crosstalk, enabling reliable per-channel measurements.

The multiplexers and ADCs are clocked synchronously. Each multiplexer cycles between channels at 400 kHz and each ADC acquires data at the same rate, allowing for a per-channel sampling rate of 25 kSps. The clocking mechanism is dictated by a finite state machine coded in Verilog.

2.3.3 Example Baseline Measurements

Figure 2.11 shows input-referred spectral densities for one measurement channel without a nanotube device connected. The RMS noise, computed by integrating over ENB, is 10.73 pA_{RMS} for this particular channel, in good agreement with the value obtained from noise simulations (8.3 pA_{RMS}) in Section 2.3.1. Baseline measurements were also performed for all 58 device channels, and the RMS current noise was computed for each channel (Figure 2.12). The expected value is 10.8 $\pm$ 0.18 pA_{RMS}, representative of consistent multiplexed recordings across the signal chain array, which spans more than 8" on the circuit board.

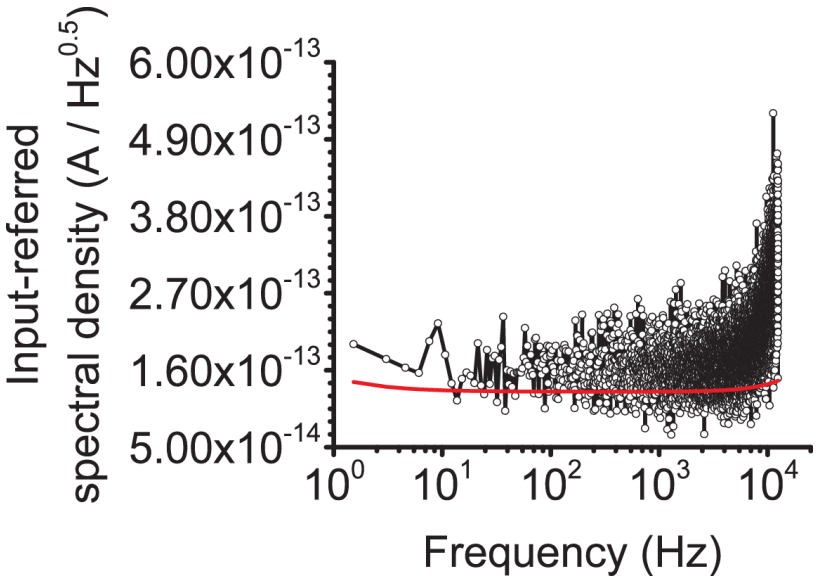

Figure 2.11: Single channel measurement of input-referred noise (black line and open circles) compared to the input-referred noise determined from simulations (red). Switches are deactivated. The closed-loop gain is set to 200 MΩ.

2.3.4 Nanotube Noise

Even though the nanotube was modeled as a large-valued resistor before, in reality, it is predominantly affected by flicker (pink) noise:

$$\frac{A}{\sqrt{Hz}} \propto \frac{\alpha}{\sqrt{f^{\beta}}} \tag{2.6}$$

where α is the flicker coefficient and β is a fitting variable which accounts for non-ideal pink noise behavior. It has been experimentally demonstrated that β usually ranges between 1

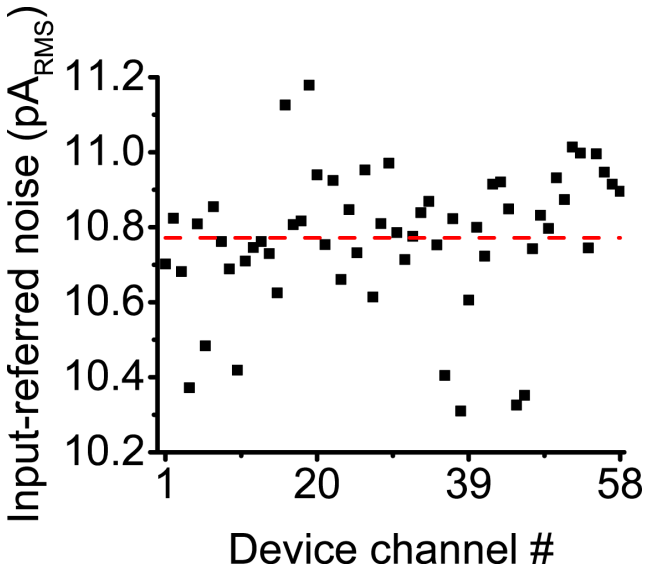

Figure 2.12: Baseline RMS input-referred current (in pA_{RMS}) for each of the 58 device channels. For each channel, the drain-source switches are disconnected and the closed-loop DC gain is programmed to 200 MΩ (e.g. 1 MΩ from the TIA stage and 200 V/V from the voltage amplification stage).

and 1.1 [46]. Naturally, at low frequencies, this flicker noise has a greater magnitude than any of the noise characterized thus far. The input-referred noise of a nanotube connected to the measurement electronics (including all measurement and electrolyte parasitics) is shown in Fig 2.13, demonstrating that the nanotube noise is greater than the white noise floor across all frequencies of interest. At low frequencies, the value of β is 0.9911, very close to true pink noise.

2.3.5 Digital Control with Decoders

In this PCB design, 23 switch ICs, 15 potentiometer ICs, and 16 source and drain DAC ICs (eight in each grouping) are utilized. Each of these components communicates with the FPGA via a serial peripheral interface (SPI), which has three signaling lines – serial data in (SDI), serial clock (SLCK), and chip/slave select (SS). SDI and SCLK are shared amongst ICs of the same type (switches, potentiometers, or DACs). Nevertheless, each IC requires an unshared SS digital line to uniquely activate it. Taking into account the number of parallel lines needed to carry the ADC digital outputs ($14 \frac{lines}{ADC} \times 4\ ADCs$), the number

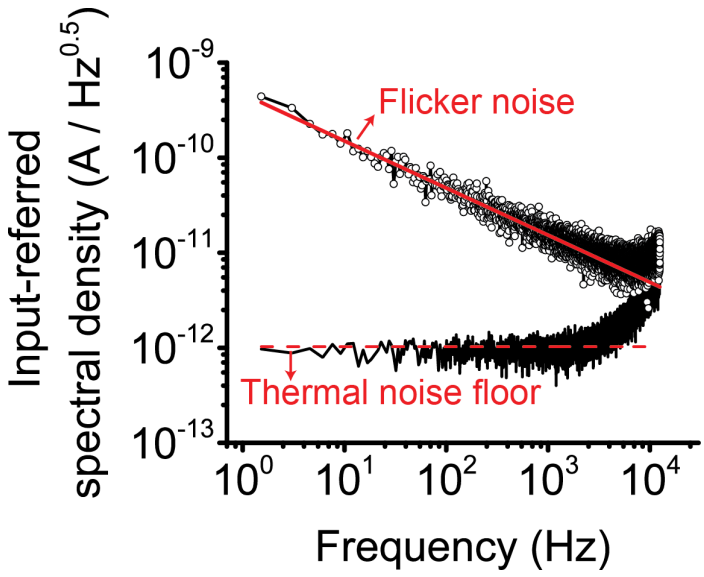

Figure 2.13: Input-referred current spectral densities measurements with and without CNT connected to one signal chain. Both measurements were conducted with the same gain setting (2 MΩ, 1 MΩ from the TIA stage and 2 V/V from the voltage amplification stage). The nanotube noise, fit to $\approx \frac{10^{-6}}{\sqrt{f}}$ (solid red line), is above the thermal noise floor (dashed red line) for the electronics at all frequencies of interest.

of available input/output (I/O) ports (110+ for the chosen FPGA) would quickly deplete, if this signaling scheme were used exactly.

To alleviate this resource demand, each select line of a switch, potentiometer, or DAC component is wired to one active-low output of a 3-to-8 decoder. Multiple 3-to-8 decoders are joined together to form one 5-to-32 decoder (Figure 2.14). This arrangement substantially reduces the number of control I/O: for every eight SPI components, only five control bits are necessary.

2.3.6 Power Supplies

The board has one global ground plane but dedicated positive voltage planes. All analog components are powered with a single supply of $V_{DD} = 5$ V, derived from an LDO voltage regulator[1] powered with 6 V input voltage. The total current draw for all analog components is 455 mA (translates to 2.3 W, conservatively).

The ADC ICs are powered by two positive voltage domains: 5 V for the internal

[1] The nominal drop-out voltage is 310 mV.

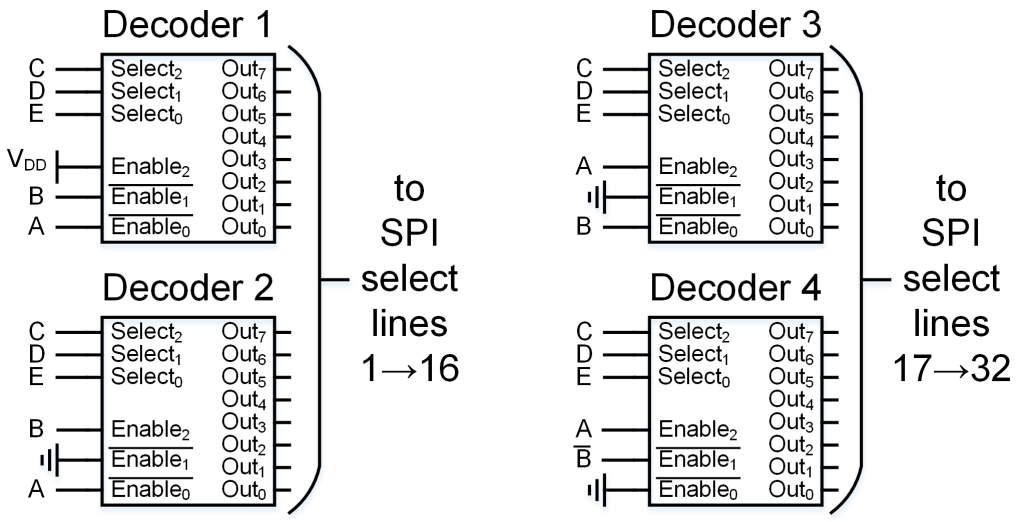

Figure 2.14: 5-to-32 decoder built from 3-to-8 decoder ICs. A and B input lines are used to select the proper decoder, while C, D, and E lines are used to select the appropriate decoder output. Although only four decoder blocks are drawn, seven decoder ICs are populated on the PCB to drive a total of 54 SS control pins.

analog-to-digital conversion circuitry, and 3.3 V – which is directly output from a switching regulator (2 A current capacity) on the Opal Kelly – for the digital output buffers. The Opal Kelly FPGA is powered separately with V_{DD} = 5 V and draws 115 mA in an idle state and 470 mA when programmed.

Furthermore, bypass capacitors are used near the connection point of each voltage source to reduce high-frequency noise and interference as much as possible. The positive power terminals for all IC components (analog and digital) are decoupled with 0.1 μF and 10 μF capacitors in parallel, providing adequate power supply rejection over large (MHz) bandwidths.

Although unused, a battery indicator circuit was included to monitor the decreasing power levels when the board is powered by batteries (optional).

2.4 Temperature Heating / Sensing

Monitoring and regulating the temperature of the electrolyte interfacing with the nanotubes is critical for biosensing applications. In the DNA studies presented in Chapters 3 and 4,

a wide range ($\sim\Delta$20 °C) of temperatures is used, demanding precise heating/cooling control in the salt solution. Heating elements, such as Peltier (thermoelectric) semiconductor devices, are suitable for this task. When a DC voltage is applied, heat is absorbed on one side (the "hot" side) of the thermoelectric device and released on the other side (the "cool" side). If the polarity of the DC voltage is reversed, the direction of heat transfer reverses as well. Generally speaking, these devices require heat sinks for efficient thermal management.

One proposed heating & sensing scheme incorporates the use of a Peltier module underneath the fabricated chip to heat the surrounding environment in close proximity to the chip surface. A resistive temperature device (RTD) would sense the temperature in solution and provide feedback to the Peltier control circuitry to adjust the temperature accordingly. Due to its small form factor and ease of fabrication, an RTD is a convenient temperature control element compatible with the PDMS microfluidic system detailed in Section 3.4. Peltiers are not used in the DNA studies in Chapters 3 or 4 because resistive heaters are easier to implement.

To control the resistive heater, a few power MOSFETs are driven by a filtered pulse-width modulation (PWM) signal from a microcontroller, thereby generating a pseudo-DC signal at the gate terminal of each FET. Un-filtered PWM is also realizable, but not without the risk of electromagnetic interference or excess coupling due to an oscillating square wave. The proposed control circuitry appears in Figure 2.15a. The branch composed of a power transistor and a small series resistor can be copied N times, depending on the power requirements of the heating element. Power transistors are used to accommodate high current levels (>1 A) required to heat low-impedance resistive heaters. Such transistor packages ordinarily include flyback diodes to quench transient currents arising from inductive loads, although the heaters used in this application are largely resistive (which outweighs the reactance).

Pertaining to monitoring the temperature in a given environment, the circuitry for this purpose is shown in Figure 2.15b. To avoid self-heating of the RTD, excitation currents are limited to below 1 mA by tuning the value of $R_{limit,\,RTD}$. A voltage divider is used

to sample the voltage drop across the RTD, which is then buffered, low-pass filtered (to attenuate intrinsic noise from the RTD itself) and subsequently digitized.

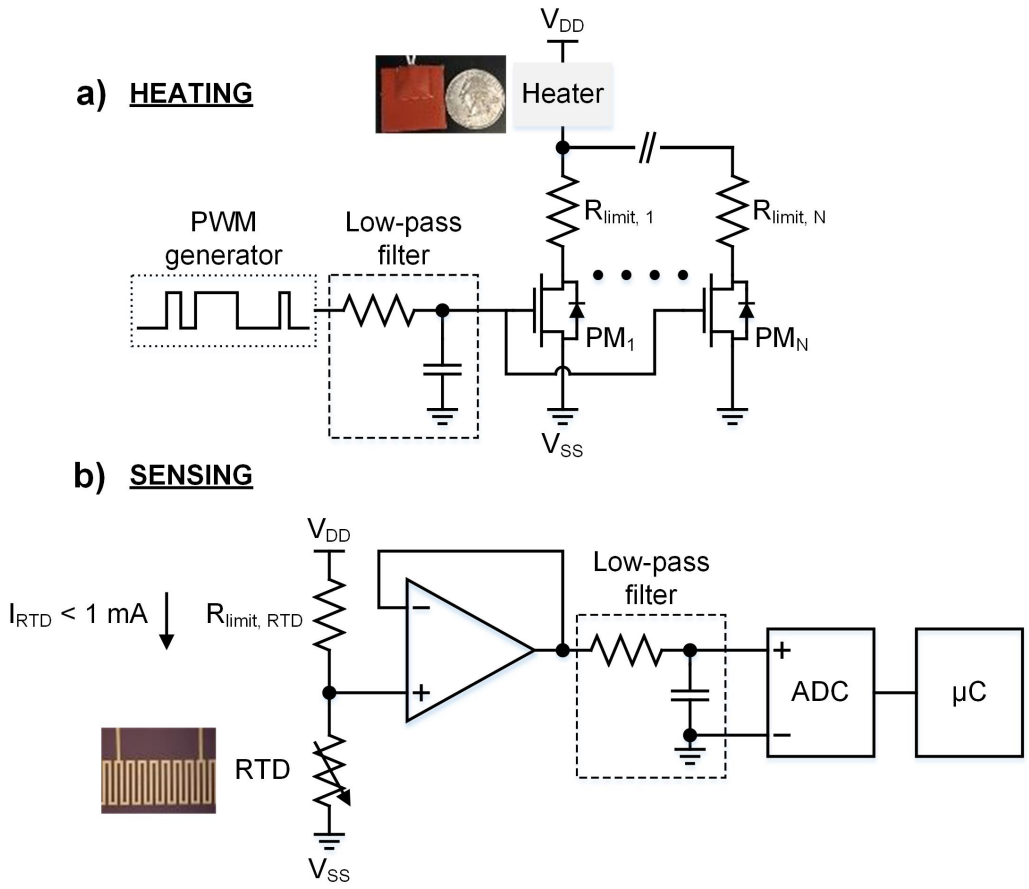

Figure 2.15: a) Resistive heater heating circuit. The gate terminals of a few power FETs (PM_1 to PM_N) are tied together, resulting in multiple drain-source current branches. Current-limiting resistors ($R_{limit,1}$ to $R_{limit,N}$) are utilized to precisely define the current each power transistor is permitted to drive. b) RTD measurement circuit.

2.4.1 RTD

RTDs were fabricated using Titanium (to prevent DC current paths between the electrode metal and the electrolyte) and calibrated in the following fashion. Chips containing RTDs were mounted on a small PCB placed on top of a hotplate and covered to localize the heating above the hotplate surface. A thermocouple was placed in close proximity to the chip surface. The hotplate temperature was set and allowed to stabilize for five minutes. Then, the voltage across the RTD was recorded and its resistance was back-calculated. A

2-wire measurement was performed, where the RTD sinks 0.5 mA current sourced from a precision current source (either a Keithley 2400 sourcemeter or a breadboard-compatible IC current source). This configuration is shown in Figure 2.16a. The thermocouple reading was also noted. The hotplate setpoint was steadily increased over the range 25 – 60 °C. Immediately thereafter, the setpoint was slowly ramped down, and new resistance recordings were made. On a different day, a 3-point calibration was executed. Thermocouple readings were collected at 4 °C (inside a closed refrigerator), at room temperature (in an ambient laboratory environment), and at 100 °C (inside an oven).

Figure 2.16b shows the measurement results from the three distinct trials – heating up, cooling down, and three-point calibration – for one RTD (nominal resistance at room temperature is ~9.7 kΩ). The linear fits for the red and blue curves closely match – exhibiting slopes (absolute value) of 3.07 and 3.19 Ω/°C and y-intercepts of 9.102 and 9.104 Ω, respectively – indicating that the RTD behaves linearly regardless of the polarity of temperature change. The three-point measurement corresponds to a slightly smaller slope and intercept (2.738 Ω/°C and 9.095 Ω, respectively), but given the measurement simplicity, this is a practical option for calibrating a fabricated RTD.

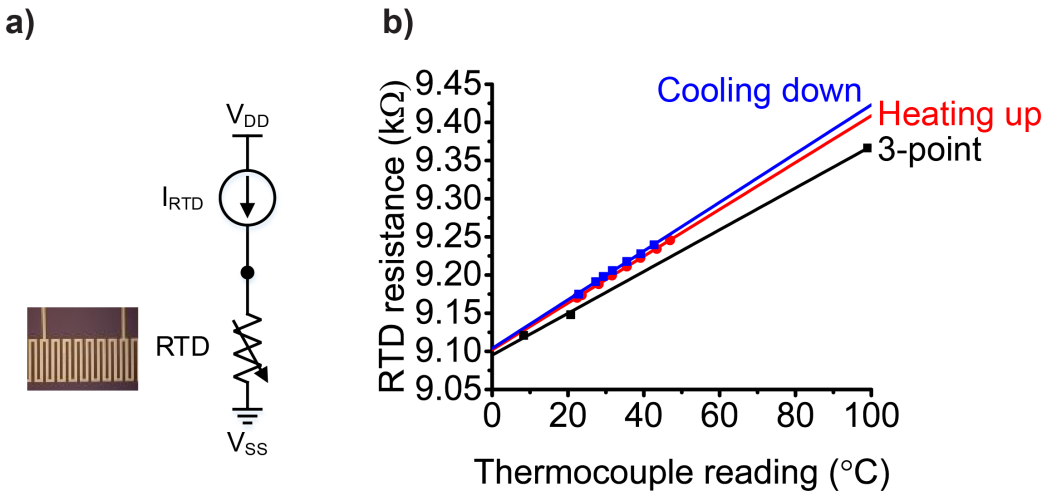

Figure 2.16: a) RTD calibration measurement circuit. b) RTD calibration curves – heating up, cooling down, and three-point calibration. Measured points are indicated as filled squares or circles; extrapolated fits are indicated as solid lines.

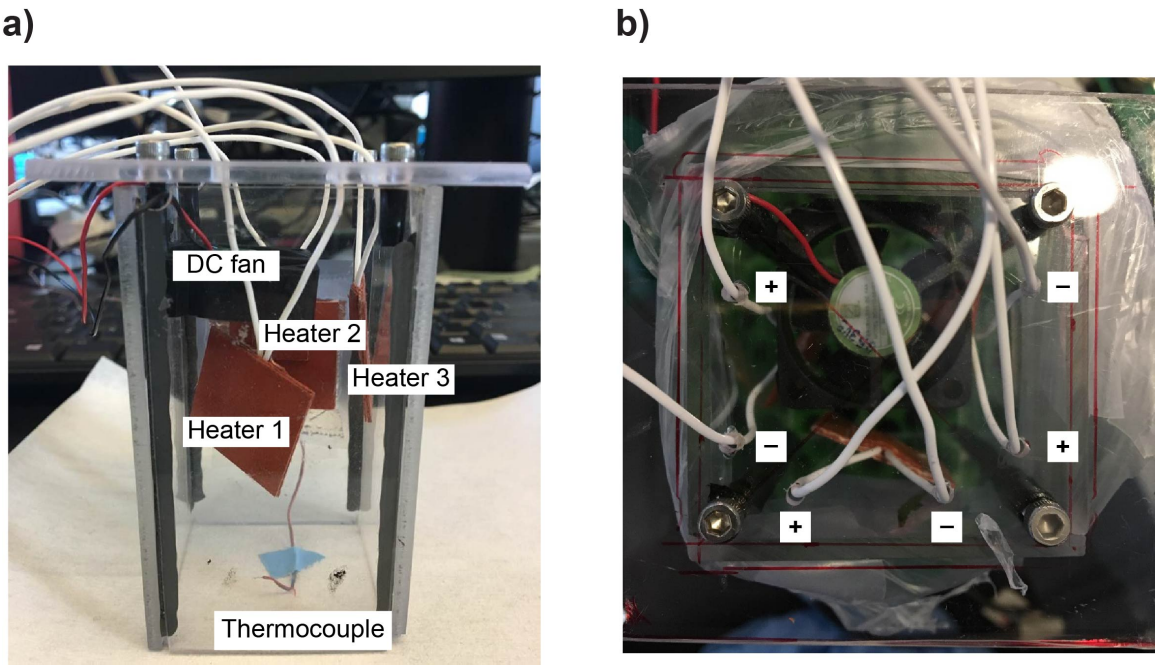

Figure 2.17: a) Temperature housing unit side view, exhibiting three Silicone heaters mounted within a rectangular plastic enclosure. In an effort to prevent thermal damage to the interior sidewalls, care is taken to ensure the backside of the heaters do not touch them. b) Top view, showing connectivity

2.4.2 Utilized Scheme

In the studies of Chapters 3 and 4, neither Peltiers nor fabricated RTDs are utilized. Instead, three resistive silicone heaters are mounted inside and connected in parallel within a custom plastic enclosure, as seen in Figure 2.17. The heater power is controlled by a standard bench-top power supply (12 V_{max}). One miniature DC fan is mounted near the top to improve air circulation. A thermocouple is inserted near the bottom of the enclosure to monitor the temperature in close proximity to the microfluidic cell stamped on the chip.

2.5 Software

In addition to the measurement circuitry, custom-built software was coded to communicate with the FPGA on the PCB. A graphical user interface (GUI) (screenshot in Figure 2.18) was designed using Python in tandem with PyQt, a Python binding for the Qt software suite. The software is multi-threaded. Individual processing threads are triggered at appropriate

times to allow the software to run smoothly.

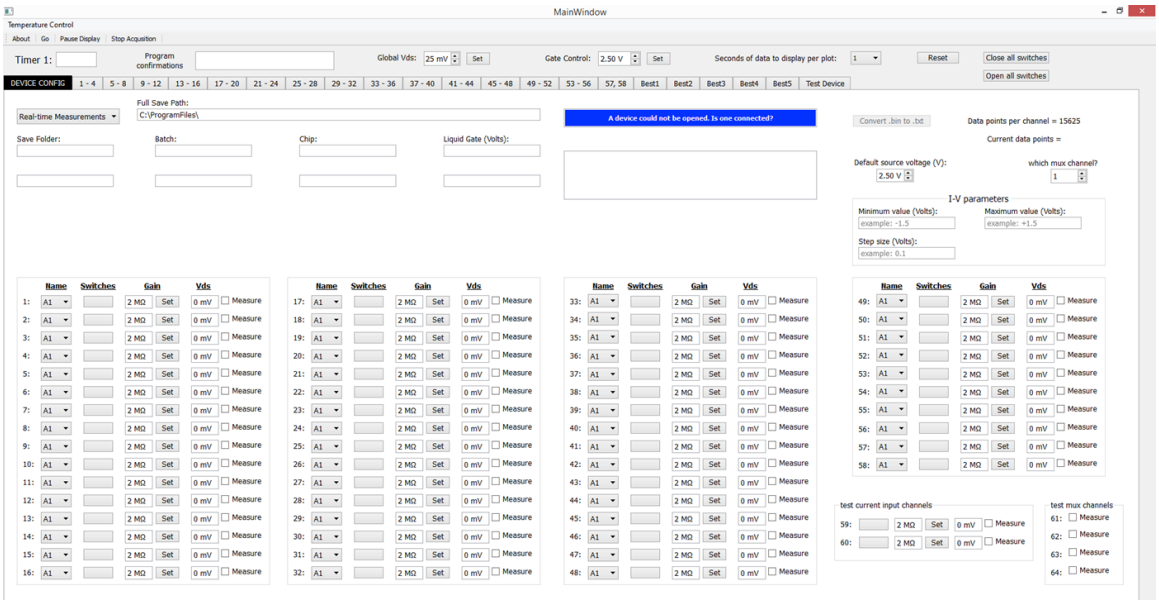

Figure 2.18: The device configuration tab of the designed graphical user interface. The user has the ability to switch on/off devices and control the voltages of each. Controls for 58 device channels and six test channels are shown.

The FPGA communicates with the PC via USB. Incoming bitstreams to the PC, containing data from all ADCs, are parsed in software. Data flags are used to align the incoming bitstream with the correct graphical viewing window.

In an effort to maximize control over the electrical biasing of each smFET device, certain features are implemented in software. First, source-drain potentials for each smFET device can be independently calibrated. Secondly, gain settings are fully customizable from 1–200 MΩ. Additionally, multiple measurement modes, each of which is outlined in detail below, are available.

2.5.1 Measurement Modes

The software is designed with four principal operating modes in mind:

1. Liquid-gate I_{ds}-V_{lg} sweeps mode – for characterization of the devices in aqueous and organic electrolytes post-wirebonding

2. Real-time mode – for monitoring real-time currents, such as stochastic single-molecule

signals

3. Hold mode – for use in regulating the reaction rates of diazonium functionalization

4. Automated I-V and real-time sequences

I-V Sweep Mode

In this mode, the user has the ability to control parameters related to I_{ds}-V_{lg} sweeps in an aqueous or organic buffer. The allowable liquid gate range, which is hard-coded in software, is $V_{lg} < |1.5\ V|$. Individual gate sweeps are defined by a measurement time (during which data collection occurs) and settle time (during which the gate value changes and settles before further data acquisition). The user can opt to run multiple sweeps to understand hysteresis effects of the smFETs in an electrolyte. An example I-V measurement is shown in Figure 2.19.

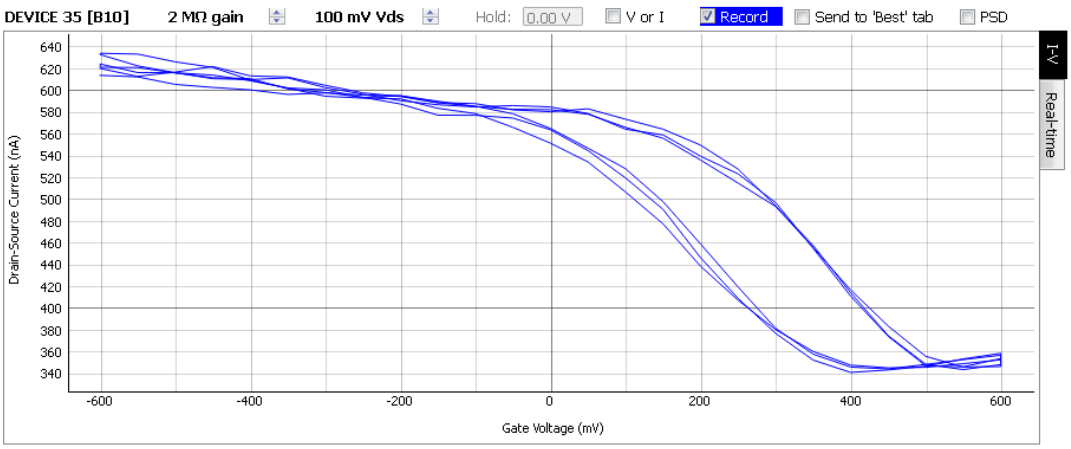

Figure 2.19: The I-V display graph for one device channel, showing multiple electrolytic gate sweeps (in aqueous phosphate buffer) for an ambipolar nanotube device with high current levels.

Real-time Mode

Transient signals can be recorded at programmable gate biases. The user has the option to run this mode continuously or for a finite period of time, both with or without saving data to hard disk. A screenshot for a 1-second recording appears in Figure 2.20.

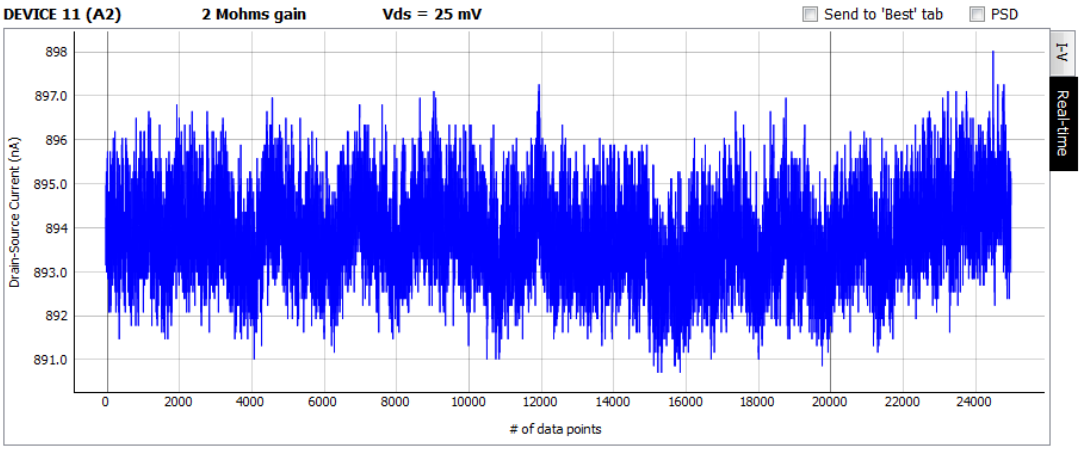

Figure 2.20: The real-time display graph for one device channel, showing a nanotube device with high current levels and 1/f noise behavior. Pertinent device settings are shown above the plot window.

Hold Mode

The flexibility of the DACs gives rise to a third measurement mode, in which the source and drain potentials of a given device are 'held' at the same value. To achieve this, the V_{ds} is zeroed while the DC offset of both source and drain potentials is manipulated. This functionality is important for regulating CNT sidewall defect generation with diazonium salts, whereby the Fermi level of the nanotube (relative to the common V_{lg}) can be adjusted separately from device to device.

Automation Sequences

This mode was created to enable streamlined experiments consisting of multiple of I-V and real-time measurement trials. Multiple experimental conditions (temperature, salt concentration, liquid gate bias, etc.) are written into a plain text file, which then is loaded into the user interface. These text files contain special lines of text corresponding to pre-defined commands in software.

Chapter 3

Bias-dependent Melting of DNA Duplexes

Dr. Sefi Vernick was instrumental in shaping the thoughts and concepts in this chapter.

3.1 Introduction

The study of DNA hybridization kinetics and thermodynamics is foundational to many genomic diagnostic technologies. The formation of a double-stranded DNA (dsDNA) helix (a duplex) from single-stranded DNA (ssDNA) has been well characterized by the all-or-nothing, two-state model (ssDNA $\rightleftharpoons$ dsDNA) which describes extreme thermodynamic processes – the enthalpically favored base-pairing (related to hybridization) and the entropically favored single-stranded random coil (relating to melting) [36,47]. Single-molecule techniques, ideal for investigating DNA dynamics at equilibrium, have evolved and have led to both experimental [48, 49] and theoretical discoveries [50, 51]. The majority of methods for single-molecule studies have only become available in the last decade, with developments in the field of fluorescence-based (smFRET) [31] and force-based methods

[0] Information from this chapter is derived from S. Vernick, S. M. Trocchia, S. B. Warren, E. F. Young, D. Bouilly, R. L. Gonzalez, C. Nuckolls, and K. L. Shepard, "Electrostatic melting in a single-molecule field-effect transistor with applications in genomic identification," *Nature Communications*, vol. 8, p. 15450, May 2017.

(AFM, tweezers) [29]. Prior studies employing electronic transducers, such as nanotubes or nanowires [10, 52, 53], have also been performed, whereby signal levels were determined by an ensemble measurement of many molecules bound to the sensor surface. Such "analog" measurements are susceptible to non-specific adsorption, high sensor-to-sensor variability, and poor reproducibility.

In contrast, the all-electronic smFET platform introduced in Section 1.3.2 is ideal for "digital" measurements which elucidate hybridization kinetics without fluorescent labeling and with superior time-resolution to standard bench-top equipment. As long as there is sufficient signal-to-noise (SNR) contrast between the discretized states of the signal, conductance differences (ΔI) can be resolved. In the case of genomic identification, the electronic system is characterized by two distinct states representing hybridized and non-hybridized dispositions for the tethered probe molecule. When the temperature is kept near the theoretical melting temperature, T_m, frequent hybridization (association) and melting (dissociation) of the target DNA molecule to the SWCNT-tethered probe DNA molecule produces conductance versus time trajectories, from which the target DNA concentration, hybridization rate (k_{hyb}), melting rate (k_{melt}), and equilibrium hybridization constant ($K_{eq} = K_A$) can be determined as a function of temperature. At different target concentrations, the single-molecule trajectories exhibit Arrhenius-like melting rates that are exponentially sensitive to temperature (but relatively insensitive to concentration) and non-Arrhenius hybridization rates mostly unaffected by temperature (but relatively sensitive to concentration).

In an ensemble experiment, DNA melting curves describe the fraction of DNA hybridized as a function of temperature, from which the theoretical melting temperature, T_m, can be extracted. The T_m is defined as the temperature at which *half of the DNA concentration* exists as a duplex and half exists in a single-stranded state. Compare this to the corresponding definition for a single-molecule melting curve: the T_m denotes the temperature at which DNA *spends half of the measured time* as a duplex and half of the time in a single-stranded state. In essence, we trade the notion of concentration of DNA duplexes

for dwell time of DNA duplexes.

Efforts to extend single-molecule DNA studies to interrogate longer oligomers (>15-20 mers) are desired, yet not without significant challenges. First, the pi-stacking driven adsorption of single-stranded DNA to the CNT sidewalls is increased [54]. Second, required melting temperatures now often exceed 60 °C, affecting the SNR (by increasing low-frequency noise) and sensitivity (by lowering the baseline current signal [55, 56]) of the device and reducing sensor reliability (by introducing technical challenges pertaining to temperature cycling). Lastly, the hybridization kinetics become more complex, involving intermediate states. The study of hybridization kinetics of longer oligonucleotides is, however, of utmost importance. Revealing the mechanisms of single-molecule DNA interactions would not only benefit the field of genomic assays but may also pave the way towards clinically relevant applications.

In this study, we address these issues with the first demonstration of electrostatic control of hybridization kinetics applied to smFET-based genomic identification. Traditionally, in ensemble experiments of the interactions of many DNA molecules, one can alter the system's temperature to track the fraction of DNA hybridized and melted, providing insight into the thermodynamics of the system through the free energy change ΔG°. Here, instead of modulating the temperature, we use the applied solution potential (relative to the CNT) to induce changes in the hybridization and melting rates (k_{hyb} and k_{melt}, respectively) of a single-molecule duplex, which would otherwise be time-averaged in ensemble studies. Electrostatic modulation of binding kinetics allows bias, an intrinsic tunable variable of this all-electronic platform, to act as a proxy for temperature, with electrostatic melting (e-melting [57]) possible at a fixed temperature. This alleviates the need to operate devices at elevated temperatures. Finally, the e-melting mode allows for straightforward identification of single nucleotide polymorphisms (SNP) in target detection through a characteristic effective melting potential, E_m [58], an electrostatic analogue for the traditional melting temperature, T_m.

3.2 Device Realization and Characteristics

Carbon nanotube smFETs are based on the introduction of a single point functionalization on an isolated SWCNT sidewall with, in our case, nano-confined covalent modification with a diazonium salt reagent. Recently, we have increased the fabrication yield and reproducibility of single-molecule devices by confining the defect-generation chemistry using lithographically patterned nanowells on the surface of individual SWCNT [59]. This nano-confinement is necessary to ensure a single reaction because the diazonium reagent chemistry is not yet sufficiently regulated to create only one single defect on a pristine nanotube. To generate a sidewall defect, we use the diazonium reagent formylbenzenediazonium hexafluorophosphate (FBDP, shown in Figure 3.1) for this study because of its stability and compatibility with classic bio-conjugation methods. This molecule also obviates the need for further linkage or activation steps [60]. We synthesize this compound according to a published protocol [20].

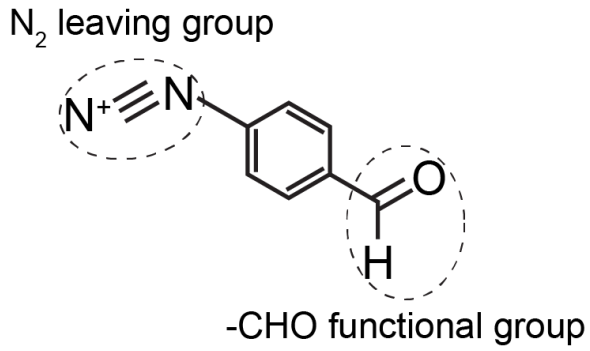

Figure 3.1: FBDP molecule, with triple-bonded N_2 leaving group and aldehyde functional moiety available to react with biomolecules of interest.

FBDP was electrochemically characterized before use in this study. Cyclic voltammetry measurements of FBDP were performed with a CHI 760D potentiostat (employing an electrochemical cell with Au working electrode, Ag/AgCl reference electrode, and Pt wire counter electrode, all from BASi®). FBDP was diluted in either organic or aqueous solvent, revealing an irreversible electro-reduction of FBDP at low anodic (e.g. oxidation) potentials and demonstrating the chemical stability of the triple-bonded, positively charged

N_2 leaving group. At a potential of 200 mV versus an Ag/AgCl reference electrode, FBDP is electrochemically reduced and grafts to the working electrode, completely fouling the surface. After three voltammetry cycles, no electrochemical activity can be recorded with the working electrode (Figure 3.2), as demonstrated with the ferrocyanide/ferricyanide redox couple $[Fe(CN)_6]^{3-}/[Fe(CN)_6]^{4-}$ and with ferrocene $(Fe(C_5H_5)_2)$.

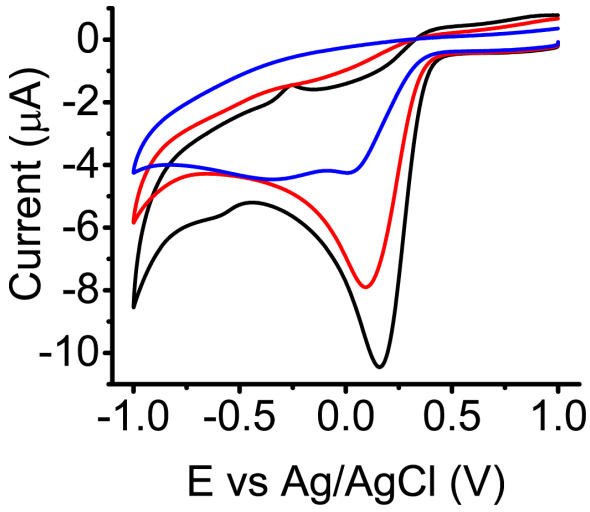

Figure 3.2: Cyclic voltammetry (-1 V to +1 V at a scan rate of 500 mV/sec in acetonitrile with tetrabutyl ammonium hexafluorophosphate salt (NBu_4PF_6)) showing the irreversible electro-reduction of FBDP to a gold working electrode at $E_p = +200$mV. This results in in complete passivation of the electrode surface.

3.2.1 Fabrication

smFETs are fabricated in the following manner. First, as shown in Figure 3.3a, nanotubes are grown by CVD with a ferritin catalyst at 890 °C on the surface of 1x1 cm^2 bare Si (500 μm heavily-doped p^{++})/SiO_2 (285 nm). The average spacing between grown nanotubes is ∼1 nanotube per 100 μm. Secondly, 64 source and drain electrodes (each 8 mm × 15 μm, segmented into 16 blocks of four pairs) are patterned orthogonal to the growth direction of nanotubes using a bi-layer-resist photolithography process (Figure 3.3b). The gap between electrodes is 4 μm, defining the nanotube channel length. Titanium metal (∼70 nm) is deposited through electron-beam evaporation to define these electrode pairs (Figure 3.3c), and the photoresist stack is lifted off. A micrograph of a sample chip after titanium

deposition is shown in Figure 3.4. Large rectangular bars are photo-lithographically defined above and below the electrode pattern (Figure 3.3d), and e-beam platinum (∼100 nm) is deposited to act as a pseudo-reference gate electrode (Figure 3.3e). Devices are characterized by scanning electron microscopy (SEM) to identify the location of nanotubes which bridge source-drain electrode pairs, and by atomic force microscopy (AFM) to determine diameter. Those containing single SWCNTs which span the source-drain electrode gap are protected with photoresist, while all other nanotubes are etched away with an oxygen plasma in a Technics RIE tool (250 mTorr O_2, 50 Watts, 20 seconds). Figure 3.3f shows this last step.

A typical CNT is shown in the SEM image at Figure 3.5a and AFM scan at Figure 3.5b. Typically, a CVD-grown chip contains a few nanotubes which span >5 mm, allowing a large number of devices to be fabricated from a single CNT.

3.2.2 Metrology

Before isolation of a CNT, a resonant Raman spectroscopy analysis (Renishaw in-via confocal Raman microscope using either 532 nm or 630 nm laser) is performed to infer band structure, defect density information, and the likelihood of the nanotube being single-walled (evidenced by a single peak at the radial breathing mode (RBM) wave vector). Calculation of the tube diameter d from the RBM of isolated SWCNTs according to this formula:

$$\omega = \frac{248\ cm^{-1}}{d} \tag{3.1}$$

consistently yields a diameter <2 nm [61, 62]. Double-walled carbon nanotubes, detected infrequently by their RBM signature, are discarded. The ratio of the D band (so-called disorder mode) to the tangential G band is measured, which serves as an indicator of the density of intrinsic CNT defects. In addition, the electronic structure is made evident by analyzing the G mode components. Only CNTs demonstrating no scattering at the D band (apparent relatively pristine nanotubes) are isolated for device fabrication. Typical Raman spectra of a CNT grown on Si/SiO_2 is shown in Figure 3.5c.

Following isolation of SWCNT devices, SEM scans are captured again to identify individual nanotube devices (Figure 3.5d). Devices are electrically probed using the con-

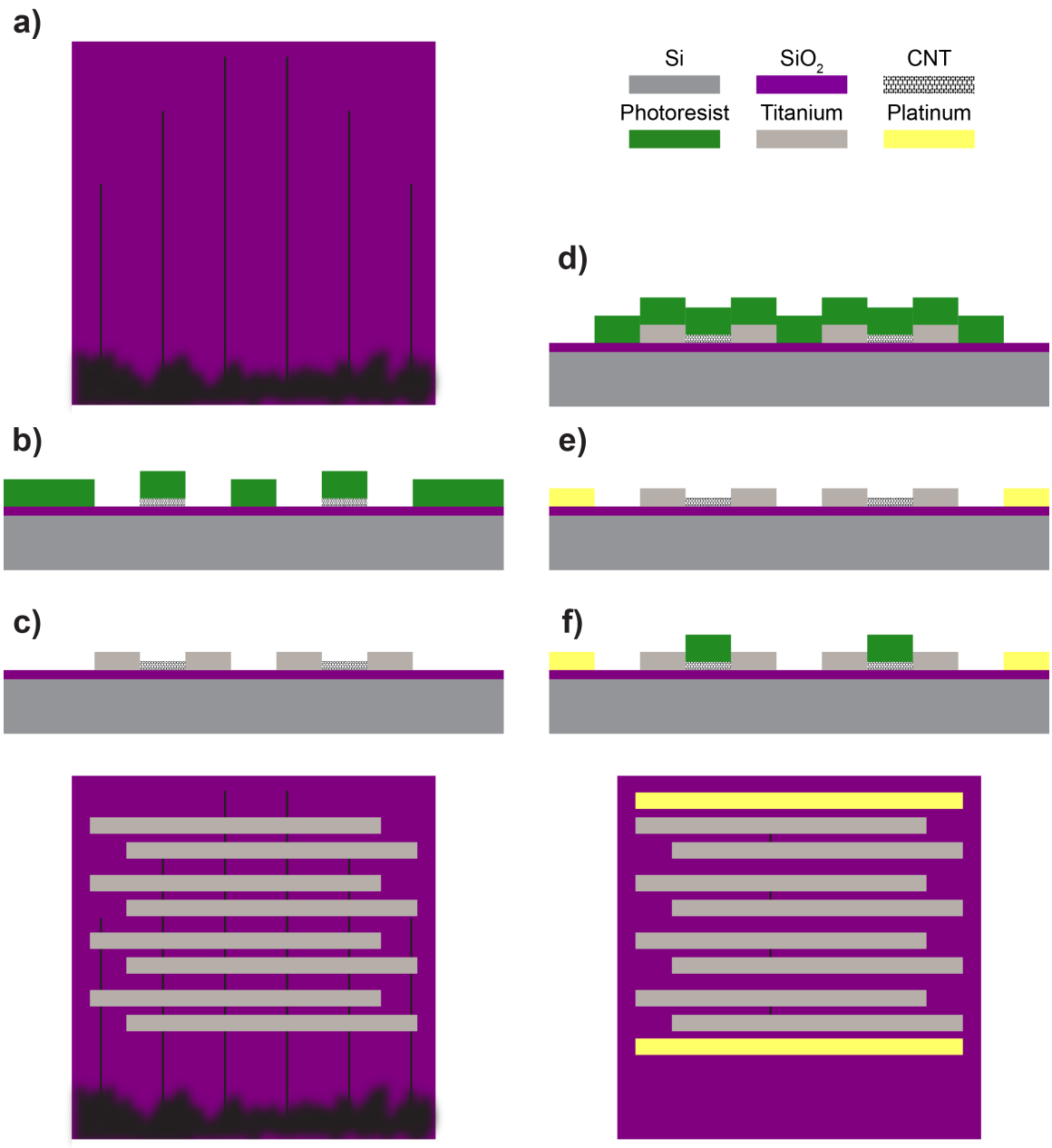

Figure 3.3: a) Catalyst-assisted CVD growth of carbon nanotubes, some of which span a distance close to the length of the chip. A top-down view of the chip surface is shown adove a profile view. b) Lithography patterning for source and drain titanium electrical contact array. c) Titanium deposition and subsequent photoresist removal. Top-down graphic shows the titanium deposition after photoresist lift-off. d) Patterning for pseudo-reference platinum gate electrodes. e) Platinum deposition and subsequent photoresist removal. f) Patterning for etching of non-passivated nanotubes, outside the device channels, with oxygen plasma. Top-down graphic shows individually contacted nanotube devices after the oxygen plasma step.

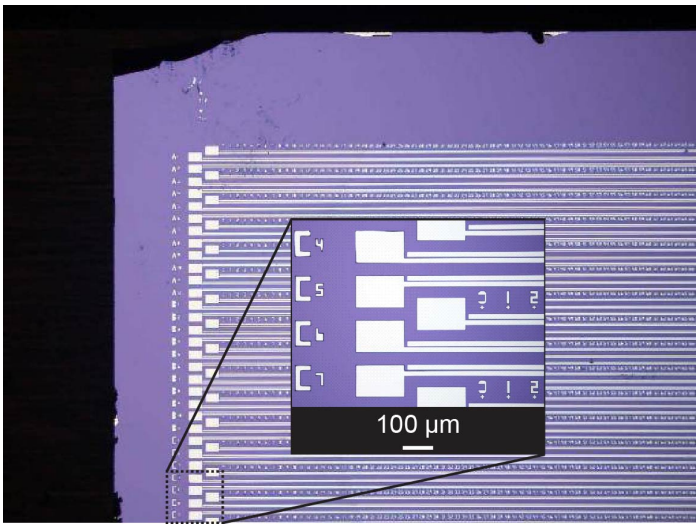

Figure 3.4: Micrograph of fabricated chip with CVD growth electrode pattern. Scale bar is indicated for the inset only.

ductive backgate. The I-V characteristics of isolated devices are measured by backgating in air (V_{bg} from –10 V to +10 V at a fixed source-drain bias of 100 mV) as shown in Figure 3.5e. The transport mechanisms in all of these I_{ds}-V_{bg} curves reveal high current levels at negative V_{bg} while the n-type conductance at positive V_{bg} is significantly lower, a result that is typical of semiconducting nanotubes because the work function of the contact metal gives rise to a high series contact resistance for the n-type branch [63]. Devices are also gated in an electrolyte with a solution potential (V_g) applied through the on-chip platinum pseudo-reference electrode.

Subsequently, nanowells are patterned in a thin electron beam resist (950K PMMA A2), as formerly described [59]. The resist is diluted by 25% before use in order to achieve a nominal layer thickness of approximately 30 nm. Then, it is spun at a spin speed of 8000 rpm for one minute. The sample is baked on a hotplate at 180 °C for two minutes and loaded into a high-resolution e-beam lithography writer (Nanobeam nB4). Nanowells measuring 24 μm long by 30 nm wide are written using 0.5 nA beam current, producing a 1:1 aspect ratio (Figure 3.6). The pattern is developed for 100 seconds in a cold mixture of 3:1 IPA:DI H_2O (4 °C), and the width of nanowells is assessed via AFM. This array of 30-nm-deep exposed windows is used to confine the covalent modification to a single site.

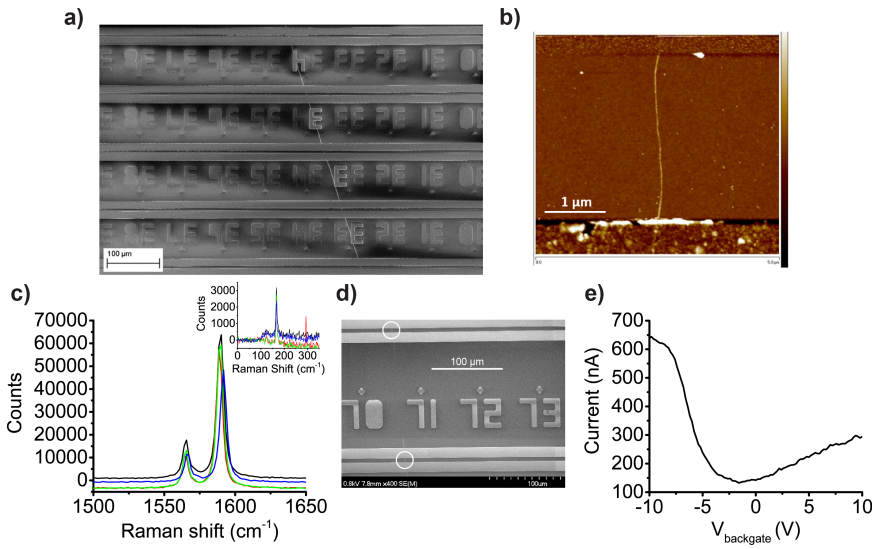

Figure 3.5: a) SEM image of a non-isolated CNT spanning five electrode pairs. b) AFM image of a CNT fragment capped by source and drain Titanium electrodes. c) Raman spectra collected from individual CNT fragments isolated from the same CNT shown in a, demonstrating reproducible Raman features, with ω_G^+ and ω_G^- located at 1588 cm^{-1} and 1566 cm^{-1} ,respectively. Inset shows the RBM spectra of the same nanotubes, located at 170 cm^{-1}, corresponding to a diameter of 1.45 nm. d) SEM image showing two CNT fragments after O_2 plasma isolation. e) I-V curve of an ambipolar (both n-type and p-type transport) SWCNT device back-gated in air.

Within the wells, devices are reacted with diazonium. Bouilly has previously reported on the yield of this modification has been [59].

3.2.3 Chip Preparation

Chips are wirebonded to ball-grid array (BGA) packages using an in-house automated wirebonder, and subsequently stamped with a polydimethylsiloxane (PDMS) flow cell placed directly above the isolated devices, which includes inlet and outlet for the facile introduction of different reagents (see Section 3.5). The chip is mounted on a custom-made printed circuit board extensively described in Chapter 2. Devices are functionalized with amine-modified oligonucleotide probe like so: wirebonded chips are exposed under the stamp to 10 μM of probe DNA in a 100 mM sodium phosphate buffer (pH 8.0) and with 200 μM sodium cyanoborohydride ($NaBH_3CN$) dissolved in 1 M NaOH. The second component is used to reduce the Schiff base formed between the amine (on the 3' end of the DNA) and the

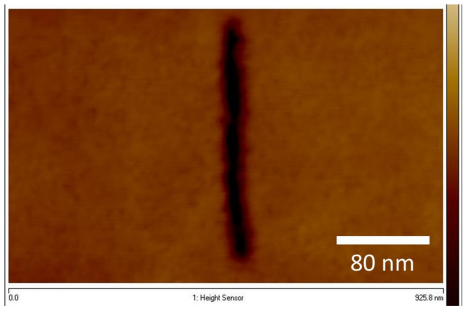

Figure 3.6: 30 nm deep nanowells (with 30 nm width) developed in a thinned down PMMA layer. The well is centered laterally between two metal contact electrodes (source and drain). Reproduced from [59].

aldehyde (on the free end of the diazonium), converting it into a stable secondary amine [60].

3.2.4 Probe Oligonucleotide Design

For the tethered probe design, we use a conserved sequence from the nucleoprotein (NP) gene of Ebolavirus Zaire, 5' (Amino-C3)-CTGTGATTTCAAATTCAGTG [1]. The target sequences studied include a 20-mer fully complementary sequence (5' CACTGAATTTGAAATCACAG), a 20-mer non-complementary sequence (5' GTGATTTCACTTGCAATGTC), and a single-nucleotide-polymorphism (SNP) sequence with a single-base-mismatch at the 3' end (5' CACTGAATTTGAAATCACAC).

3.3 Results

After diazonium modification, the sp^2 molecular orbitals are re-hybridized to sp^3, reducing the baseline nanotube conductance (Figure 3.7a). Before and after functionalization (diazonium modification followed by probe DNA attachment), the current noise spectrum is dominated by 1/f noise (flicker noise) as shown in the representative power spectral density of Figure 3.7b, calculated for a fixed source-drain bias of 100 mV for four representative smFETs. Following diazonium modification, the defect site dominates charge carrier scattering, making the rest of the CNT surface less sensitive to charge traps and resulting in reduced flicker noise.

[1] Amino-C3 denotes an amino modification positioned at the 5' end through a linker three carbons long.

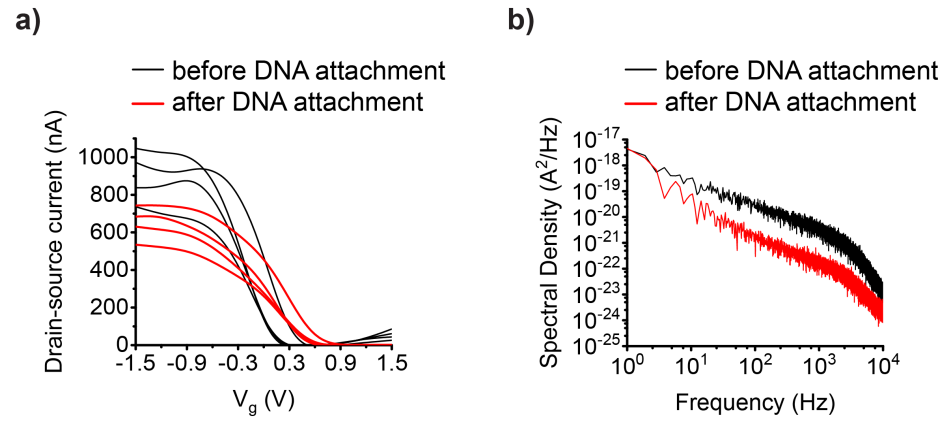

Figure 3.7:

Upon the introduction of complementary ssDNA in solution, the appearance of large conductance fluctuations is immediately observed. Frequent transitions to an additional conductance state result in a random telegraph noise between two discrete conductance levels. These stochastic trajectories are generally fit with an idealized trace showing transitions between discrete states (as shown in Figure 3.8a as a function of temperature). To accomplish this, a computationally efficient iterative event detection algorithm [64] (further described in Section 3.5) is used, which assumes a two-state model, with wandering baseline correction imposed on the trajectory. High and low conductance states are assigned. Complementary cumulative distribution functions (CCDFs), or survival probability plots, are constructed from the idealized traces and fit to an exponential function from which the characteristic time constants τ are extracted. Rate constants k (equal to the reciprocal of the corresponding time constants, i.e. $k = \frac{1}{\tau}$), describing transitions between states, are calculated. The average dwell times $<\tau>$ for the high (low) state indicates the time that the single-molecule resides in that state before transitioning to the other state, i.e. $\tau_{low} = \frac{1}{k_{low->high}}$ and $\tau_{high} = \frac{1}{k_{high->low}}$ [28,65]. Survival plots of the melted and hybridized states are shown in Figure 3.8b for 100 nM complementary ssDNA at the theoretical melting temperature of 50 °C. These same plots were also generated at the other experimental temperature points (30 °C, 40 °C, 60 °C); refer to Figure 3.9.

In contrast to smFRET studies – in which single-exponential functions are fit to

idealized trajectories – these survival probabilities are fit to a double exponential function, from which two rate constants are deduced: τ_{hyb}^{fast} and τ_{hyb}^{slow} for the hybridized state, and τ_{melt}^{fast} and τ_{melt}^{slow} for the melted state. Treating each carbon nanotube device in liquid as p-type, we can assign the high and low conductance states due to DNA hybridization and melting as follows. The presence of negatively charged hybridized DNA in the vicinity of the localized charge-sensitive defect on the nanotube creates a low resistance path for holes flowing through the transistor channel, leading to a high conductance state. Conversely, melted DNA (tethered probe only), carrying less negative charge than the duplex, induces fewer holes in the transistor channel, leading to less charge carrier scattering and a low conductance (high resistance) state. Double-stranded DNA thus scatters positive charge carriers more than single-stranded DNA does. To be consistent with analogous ensemble studies, we always choose the rate constant which best represents a 3D diffusion process (see Section 3.3.4 for more details). At low concentrations, this means choosing τ_{hyb}^{slow} and τ_{melt}^{slow}; at high concentrations, τ_{hyb}^{fast} and τ_{melt}^{fast} are used.

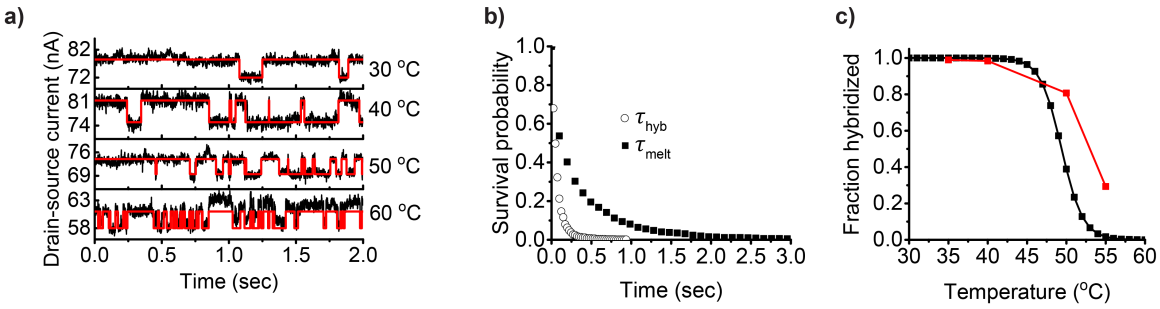

Figure 3.8: a) Time traces of 300-second recordings for 100 nM complementary DNA target. Overlaid raw data (black) and idealized fits (red) for a temperature series from 30 °C to 60 °C are shown. b) A representative survival probability curve for the curve at 50 °C from panel a. The event count is 763. The fit error is characterized by R^2=0.999 and R^2=0.998 for $\tau_{low \to high}$ and $\tau_{high \to low}$, respectively. c) Comparison of T_m from nearest-neighbor (NN) model (52.7 °C) to experimentally derived T_m (49.7 °C).

3.3.1 Single-molecule Kinetics of 20-mer Hybridization and Melting

The temperature-dependent reaction of the DNA duplex formed by the tethered probe sequence and 100nM complementary ssDNA is shown in Figure 3.8a. The higher conductance

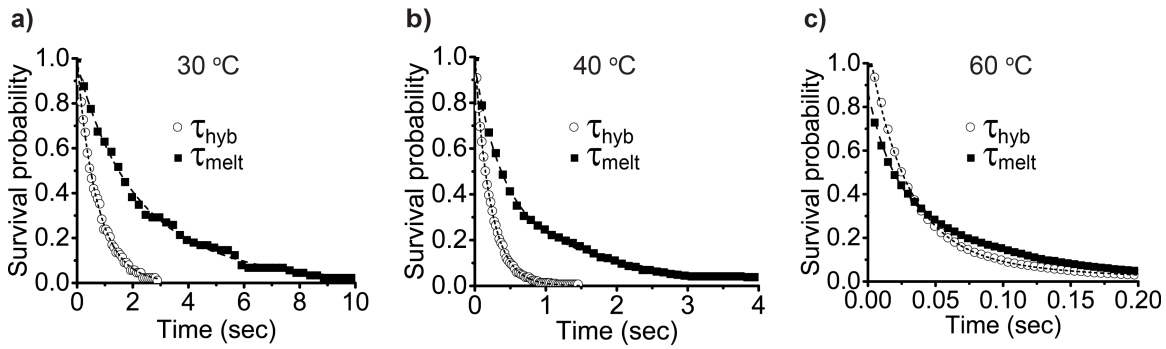

Figure 3.9: Double-exponential fits, from which hybridization and melting time constants, τ_{hyb} and τ_{melt}, are calculated. The x-axis represents the characteristic lifetimes (τ's) of survival.

state dominates at 30 °C, but gradually shifts with increasing in temperature to a dominant lower conductance state (at 60 °C). This random telegraph noise (RTN)-like behavior is attributed to carrier scattering from localized energy states [66] at the point of attachment which is modulated by charge within a few Debye length (typically 3 nm or so) of the defect site [67]. These fluctuations are neither observed in a control experiment containing no target DNA nor in a control containing a non-complementary ssDNA, shown in Figure 3.10. This sequence was measured at the same temperatures and concentration as the fully complementary strand to confirm the apparent two-state activity is neither caused by non-specific adsorption to the CNT sidewall nor by a doping mechanism.

From the corresponding survival probability plots shown in Figure 3.8b, the hybridization rate is $k_{hyb} = 1/\tau_{hyb}^{fast} = 45.30\ s^{-1}$, while the melting rate is $k_{melt} = 1/\tau_{melt}^{fast} = 11.82\ s^{-1}$. Plots of fraction of probe hybridized as a function of temperature (Figure 3.8c) can be derived (at equilibrium) from melting curves experimentally determined at the 100 nM target DNA concentration, following this equation [68]:

$$fraction\ hybridized = \frac{1}{1 + \frac{k_{melt}}{k_{hyb}}} \tag{3.2}$$

This results in a T_m of 52.7 °C, in good agreement with a melting curve with a T_m of 49.7 °C predicted using a nearest-neighbor (NN) model calculation (`http://biophysics.idtdna.com`).

The temperature dependence of k_{hyb} (k_{melt}) at a fixed bias shows an Arrhenius be-

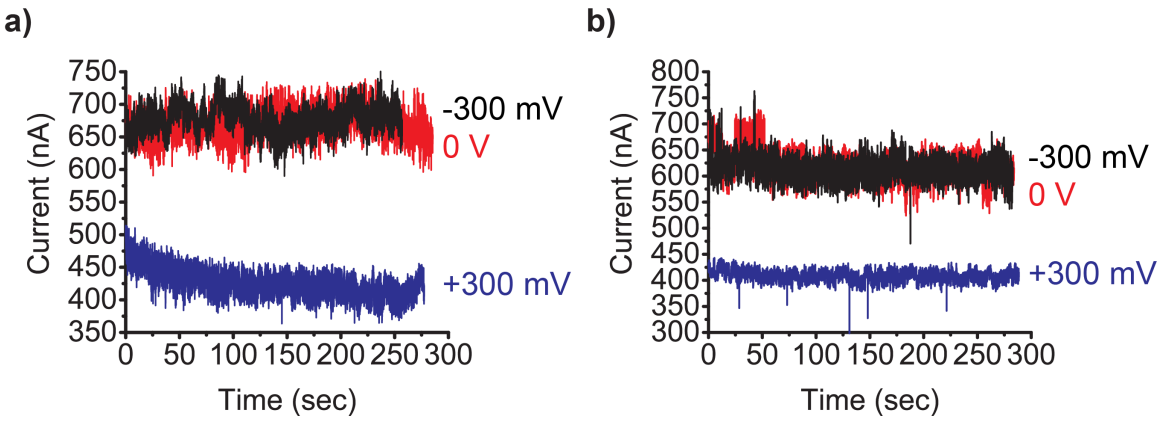

Figure 3.10: a) smFET conductance measurements (V_{ds} = 100 mV) of a CNT device with a tethered ssDNA probe in 43 mM phosphate buffer at 50 °C. The signal shows stable 1/f noise behavior, with no RTN observed over a period of ∼280 seconds. Conductance drops from V_g = -300 mV (∼650 nA) to V_g = +300 mV (∼425 nA) reflect the I-V gating characteristics of the p-type device. b) Control measurement of a functionalized CNT device in the presence of 100 nM fully non-complementary 20-mer oligonucleotide at 50 °C. RTN is not observed over a ∼290 second period. The gating trends from panel a still hold.

havior following $k = Ae^{\frac{-E_a}{RT}}$, with A being the pre-exponential factor, E_{aH} the apparent activation energy of hybridization and E_{aM} the apparent activation of melting. As shown in Figure 3.11a, the temperature dependence of k_{hyb} and k_{melt} demonstrates Arrhenius-like behavior, with apparent activation energies of E_{aH} and E_{aM} of –54.5 kJ/mol and 149.87 kJ/mol, respectively. As expected, k_{melt} shows a strong Arrhenius-like temperature dependence, while k_{hyb} shows a weak anti-Arrhenius relationship, reflecting the reduced enthalpy of hydrogen bonding at elevated temperatures. At lower target DNA concentrations (10 nM and 1 nM in Figures 3.11b and c, respectively), the hybridization and melting kinetics follow a similar temperature trend, but the activation energies are noticeably altered. At a target concentration of 10 nM and 1 nM, E_{aM} equals 113.2 kJ/mol and 167.97 kJ/mol, respectively. E_{aH} is lower at 10 nM (–56.4 kJ/mol) and significantly reduced at 1 nM (–28.3 kJ/mol), as shown in Figure 3.11b and Figure 3.11c, respectively, indicating that the hybridization reaction is less temperature-dependent (shallower slope).

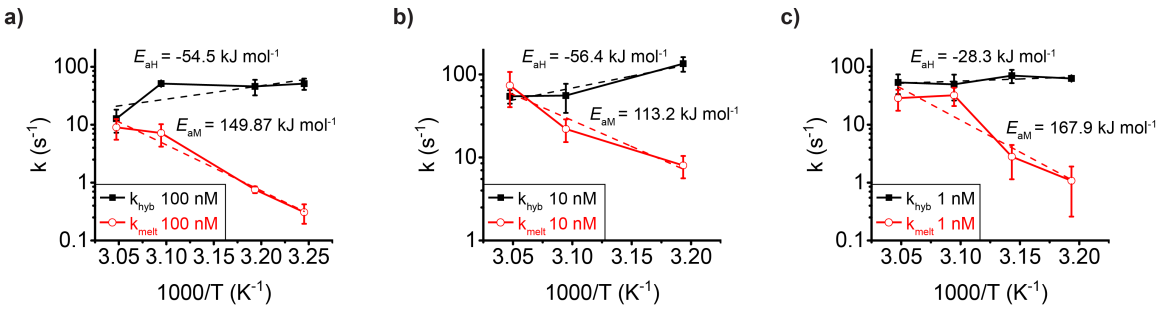

Figure 3.11: Arrhenius plots for 100 nM, 10 nM, and 1 nM target concentrations (at 0 V solution bias), showing the temperature dependence of the melting and hybridization rates. Error bars are calculated from five different 60-sec intervals at each temperature.

3.3.2 Impact of Electrostatic Bias on Hybridization and Melting Kinetics

Typically, temperature is used to control hybridization and melting rates, as evidenced in Section 3.3.1. However, for large device arrays and high temperatures, this becomes untenable. Electrochemical melting, developed over 40 years on macro-electrodes for ensemble studies [69, 70], has been demonstrated previously [57] for DNA strands longer than 20 nucleotides. Yet, to the best of our knowledge, a comprehensive analysis of bias-dependent, electrostatically-driven kinetics has not been published. This represents a paradigm shift from the traditional understanding of kinetics governed by temperature to kinetics manipulated by solution bias V_g.

The electrostatic force generated by the application of V_g = 300 mV provides sufficient energy to alter melting and hybridization rates compared to those observed at 0 V. The temperature-dependent reaction at an applied gate bias of 300 mV is shown in Figures 3.12a-c for the fully complementary oligonucleotide target at three different target concentrations (100 nM, 10 nM, 1 nM).

The effect of the applied bias on reaction rates can be analyzed using transition-state theory [71], in which case the Eyring equation is pertinent [72]:

$$k_{hyb(melt)} = \frac{k_B T}{h} e^{\frac{\Delta S^{\ddagger}_{hyb(melt)}}{R}} e^{\frac{-\Delta H^{\ddagger}_{hyb(melt)}}{RT}} \tag{3.3}$$

where k_B is Boltzmann's constant (in units of Joules/Kelvin), h is Planck's constant (units: Joules-seconds), $\Delta S^{\ddagger}_{hyb(melt)}$ is the activation entropy for hybridization (melting), R is the

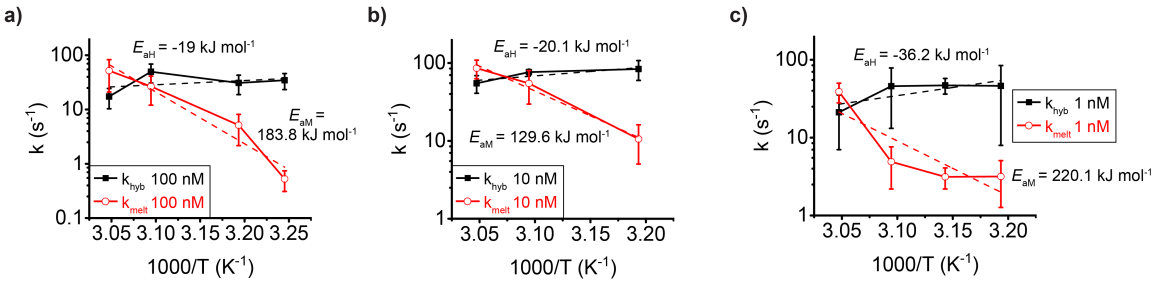

Figure 3.12: Arrhenius plots showing how application of gate bias affects the kinetics of melting and hybridization for a) 100 nM, b) 10 nM, and c) 1 nM complementary target. Upon the application of V_g = 300 mV, the entropy of activation for the melting reactions increases whereas while the enthalpy of activation for the hybridization reaction slightly decreases.

gas constant (units: Joules/Kelvin-mole), and $\Delta H^{\ddagger}_{hyb(melt)}$ is the activation enthalpy for hybridization (melting). The ‡ notation is conventional for parameters describing a transition state, defined as the state with the highest potential energy along the reaction coordinate (reactants ↔ products) [73].

By comparing Figures 3.11a-c (0 V) against Figure 3.12a-c (300 mV), one can calculate the energy differences between applied bias and zero-bias conditions: $\Delta S^{\ddagger}$ increases by 115, 58, and 157 J/(K-mol) for 100 nM, 10 nM and 1 nM target concentrations, respectively. These differences suggest that melting becomes more entropically favorable when bias is applied. More positive values indicate a more disordered transition state with higher degrees of freedom, which is more energetically favorable. Similarly, one can calculate the energy differences associated with the activation enthalpies of hybridization ($E_{aH} \approx \Delta H^{\ddagger}_{hyb}$, for temperatures ~25 – 60 °C). $\Delta H^{\ddagger}_{hyb}$ increases by 35.5 kJ/mol, 36.3 kJ/mol and 7.9 kJ/mol for 100 nM, 10 nM and 1 nM target concentrations, respectively, revealing the increased enthalpic penalty of hybridization due to 300 mV bias. More positive values indicate the reaction becomes more endothermic, which is less favorable. This is a direct result of the repulsive electrostatic force present in the vicinity of the nanotube, which promotes melting but inhibits hybridization. Positive solution bias mitigates the steric hindrance and electrostatic effects by repelling adsorbed DNA, increasing hybridization rates; more information on this point is presented in Section 3.3.4.

3.3.3 T_m versus E_m – Bias Acts as a Proxy for Temperature

The effects elucidated in the previous section suggest that electrostatic modulation may be effective for studying hybridization and melting kinetics and thermodynamics at a fixed temperature but various V_g values. Instead of using temperature, we bias the salt solution at a positive V_g relative to the nanotube (alternatively, the nanotube has a negative potential relative to the surrounding electrolyte) to induce melting and slow down hybridization. The strongest bias dependence occurs for the melting reaction; although hybridization is affected, the change is modest. Both modulation schemes are contrasted in Figure 3.13.

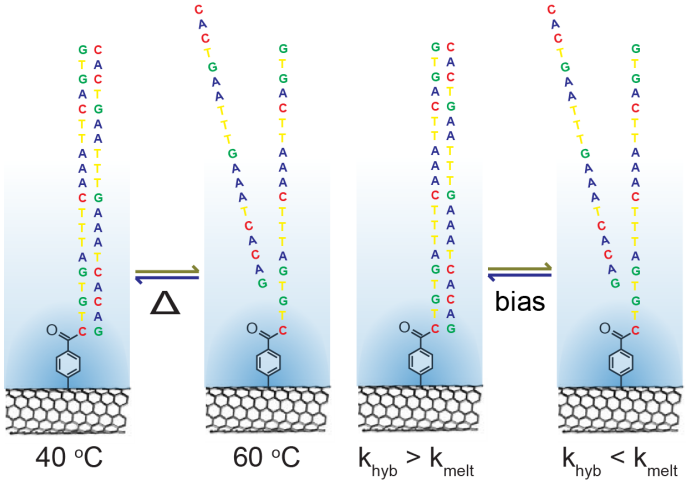

Figure 3.13: Comparison of traditional temperature-dependent melting to bias-dependent melting. With increasing temperature, the melting rate (k_{melt}) increases and the hybridization rate (k_{hyb}) decreases. Analogously, an increase in gate (solution) bias favors the melting process.

Figure 3.14a shows raw and idealized transient trajectories for one measured device at a fixed temperature (40 °C) over a range of applied solution potentials relative to the nanotube. At 0 V, only one conductance state is apparent. With increased bias, the reaction favors transitioning to the low conductance (melted) state. Control measurements with a fully non-complementary DNA target strand measured over the same range of biases and at the same fixed temperature do not exhibit such two-state activity (Figure 3.15).

Figure 3.14b and c show k_{melt} and k_{hyb} as a function of V_g for both the fully complementary and a SNP target sequences at a temperature of 40 °C and 100 nM target

concentration. These curves show electrostatically modulated kinetics which bears a striking resemblance to temperature-dependent kinetics. As expected, k_{melt} rates are larger for the SNP, since the unmatched last base pair (proximal to the nanotube) is unable to completely hybridize. Quantitatively, $\Delta H^{\ddagger}_{melt}$ for unzipping the fully complementary strand is six times larger compared to the SNP – 3.57 kJ/mol versus 0.553 kJ/mol – a remarkable single-molecule recognition sensitivity. k_{hyb} is less sensitive to bias. At higher bias values, the hybridization rate of the complementary target decreases, indicating that base pairing is slightly affected, while the SNP does not show this effect.

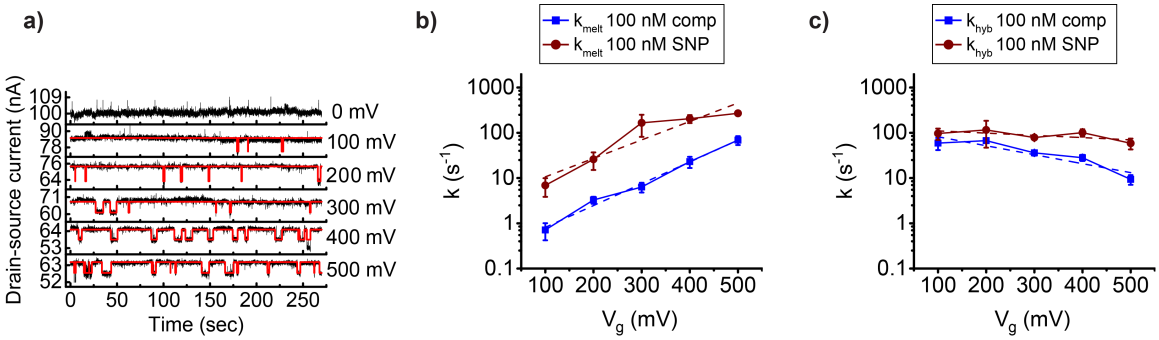

Figure 3.14: a) Comparison of temperature and bias-dependent melting. With increasing temperature, the melting rate increases and hybridization rate decreases. b) c)

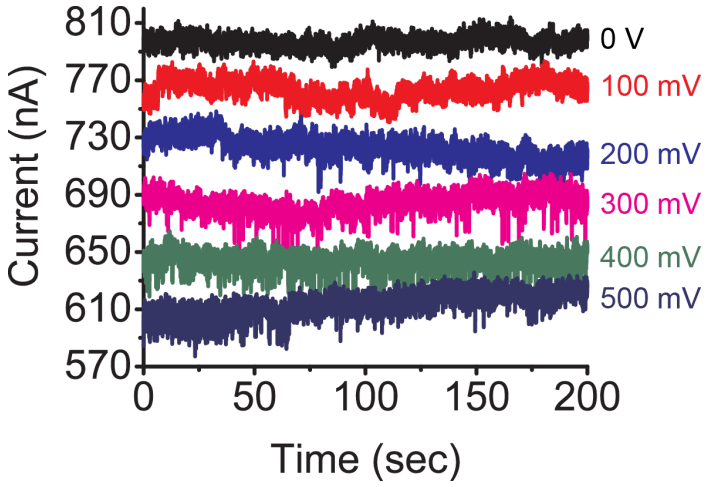

Figure 3.15: smFET control measurements with electrostatic control over a positive solution bias range (0 to 500 mV). Some baseline current levels are offset for viewing clarity, but the gating trends are still largely preserved.

The bias dependence can be modeled by a modified Kramer's rate model for hy-

bridization and melting processes, a formula which has used been used to study DNA unzipping times in nanopores [74, 75, 76, 77]:

$$k_{hyb\,(melt)} = Ae^{-\frac{\Delta H^{\ddagger} - Q_{eff}V_g}{k_B T}} \tag{3.4}$$

where A is the pre-exponential factor (related to activation entropy), $\Delta H^{\ddagger}_{hyb(melt)}$ is the activation enthalpy for hybridization (melting) without applied bias, V_g is the solution bias as defined before, and Q_{eff} is the effective molecular charge detectable within the Debye sphere. One can see that, in addition to temperature, the rate is bias-dependent ($Q_{eff}V_g$). Furthermore, regarding the melting reaction, as V_g becomes more positive, the argument of the exponential term becomes more negative. Physically, this signifies a reduction of the energy barrier required for melting; melting becomes easier. The activation enthalpy for this voltage-driven melting reaction is 3.57 kJ/mol (extracted from the slope of the k_{melt} versus 1/T curve) for the complementary target compared with 149.8 kJ/mol (extracted from the intercept of the k_{melt} versus V_g curve) in the absence of applied bias.

The effective charge Q_{eff} associated with duplex formation is slightly higher for a complementary target in comparison with the SNP ($0.40q$ vs. $0.28q$, respectively). Additionally, according to Sauer-Budge, the effective charge per nucleotide is 0.1q/nt, which is less than a theoretical value of one charge per nucleotide due to electrostatic screening effects [78]. With this in mind, the effective number of sensed nucleotides is 4 nucleotides for the complementary strand versus 2.8 nucleotides for the SNP, close to the expected difference of one nucleobase reacting within the Debye sphere.

Thermodynamic parameters, as a function of temperature, can also be extracted with the application of bias. The van't Hoff expression

$$K_{eq} = e^{\frac{-\Delta G^{\circ}}{RT}} = e^{\frac{-\Delta H^{\circ}}{RT} + \frac{\Delta S^{\circ}}{R}} \tag{3.5}$$

determines the parameters of the reaction at equilibrium. The slope of the K_{eq} versus 1/T curve is the activation enthalpy ΔH°. The $^{\circ}$ superscript is conventional notation for describing equilibrium parameters. The dependence of the equilibrium rate constant on temperature is shown for a 100 nM complementary target in Figure 3.16a with and without

the application of 300mV bias. In the absence of bias, the enthalpically favored duplex formation with ΔH° = –211.7 kJ/mol drives a spontaneous reaction (i.e. $\Delta H^\circ < 0$ and $\Delta S^\circ > 0$) for temperatures below 52 °C. When the bias is raised to 300 mV, ΔH° increases to –205 kJ/mol, due to less favorable base-pairing (i.e. a less spontaneous energy for the hybridization reaction). This has the effect of reducing K_{eq} by one order of magnitude.

The van't Hoff plots and enthalpies obtained for 10 nM and 1 nM concentrations (shown in Figure 3.16b and c, respectively) also reveal large and negative enthalpies ΔH° = –178.5 kJ/mol for 10 nM and ΔH° = –231.1 kJ/mol for 1 nM without bias. The reaction enthalpy is also increased at these lower concentrations, with ΔH° = –140 kJ/mol and ΔH° = –156.4 kJ/mol for the 10 nM and 1 nM concentrations, respectively.

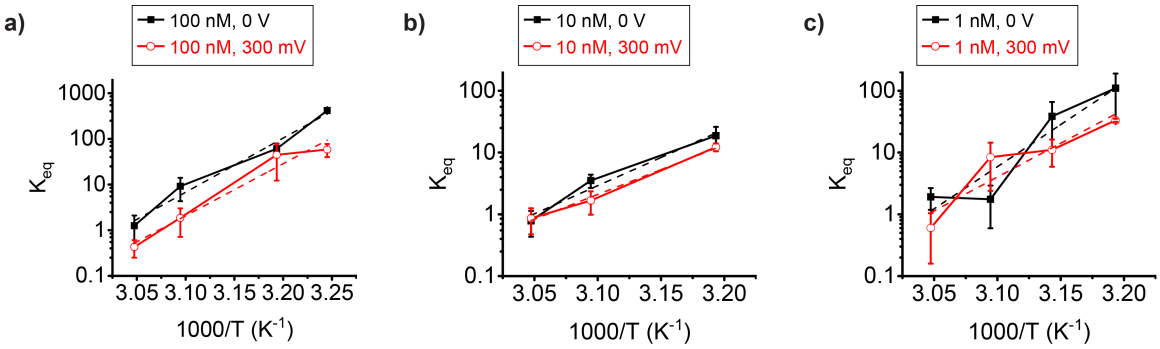

Figure 3.16: van't Hoff plots depict the effect of bias on the free energy landscape, revealing an order of magnitude lower K_{eq} and higher enthalpy for the 300 mV biased reaction at: a) 100nM complementary target, where an increase in ΔH° of 6.5 kJ/mol makes hybridization less favorable; b) at 10 nM, with an enthalpy increase of 38.46 kJ/mol; and c) at 1 nM, with an enthalpy increase of 74.78 kJ/mol. Error bars are calculated from five different 60-sec intervals at each temperature.

The Arrhenius-like plots of K_{eq} as a function of V_g allow one to easily extract Gibbs free energy, ΔG°. Changing the target DNA proximal base (i.e. on the 5' end) from a guanine to a cytosine in the SNP sequence is the most destabilizing mismatch in terms of enthalpy [79], reducing the melting temperature by ∼2.6 °C, as calculated from the NN model. A similar change is observed in Figure 3.17a, for the bias-dependence of K_{eq}. We can define a melting potential (E_m) as the potential at which $K_{eq} = 1$. Using this definition, E_m is 400 mV for the complementary target but only 326 mV for the SNP.

A reaction is more thermodynamically favorable than another if the Gibbs free en-

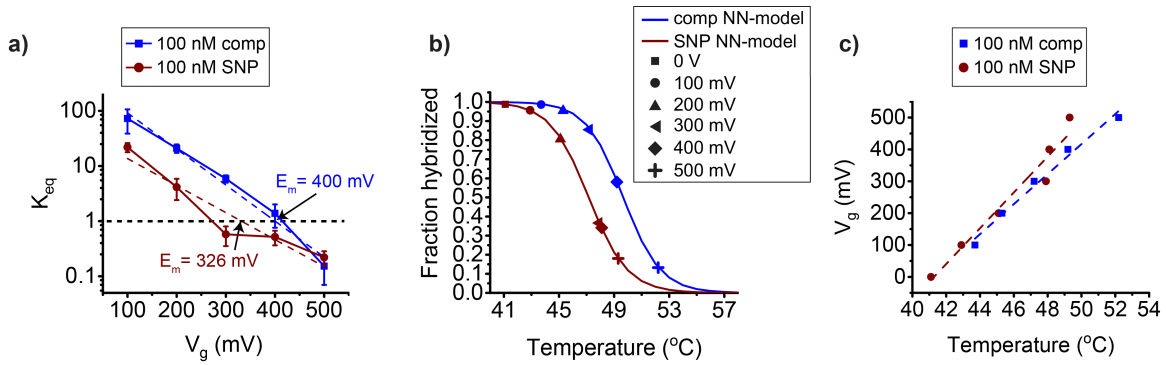

Figure 3.17: a) K_{eq} versus V_g dependence, demonstrating higher values for the complementary strand across the bias range. $K_{eq} = 1$ defines an effective melting potential E_m, which is 400 mV for the complementary strand and 326 mV for the SNP. b) Extrapolated "effective T_m" for both target oligonucleotides. c) Calibration curves for both target oligonucleotides. Bias is a proxy for temperature.

ergy is more negative. The ΔG° is –15.39 kJ/mol for the complementary target and –9.92 kJ/mol for the SNP target, reflecting that single-molecule duplex formation is more thermodynamically favorable for the complementary target. Further evidence of this assertion is illustrated in Figure 3.18. There are three bias points for which the SNP has positive values of ΔG° (indicating a non-spontaneous reaction), whereas there is only one bias point for which the complementary strand has a positive ΔG° value, suggesting that the SNP is more likely to melt from the probe than the complementary strand is.

Lastly, In Figure 3.17b, we correlate the bias-dependent melting trend at 40 °C with a predicted model for the melting temperature of the Ebolavirus DNA complementary and SNP strands under investigation. From the fraction of DNA hybridized (duplex) as a function of bias, we extract an "effective T_m" at 49.5 °C for the complementary target and 47.05 °C for the SNP. The delta between these two values (2.45 °C) is in good agreement with the expected melting temperature difference (2.6 °C) between the two strands mentioned in the previous paragraph. For each strand, it is clear that we can alter the fraction hybridized by roughly 90%; a similar observation would have been made if we had instead altered the temperature of the system by ∼8 °C. The end effect is clear: with electronic control, we can influence equilibrium in a manner commensurate with temperature and provide a calibration between them (Figure 3.17c).

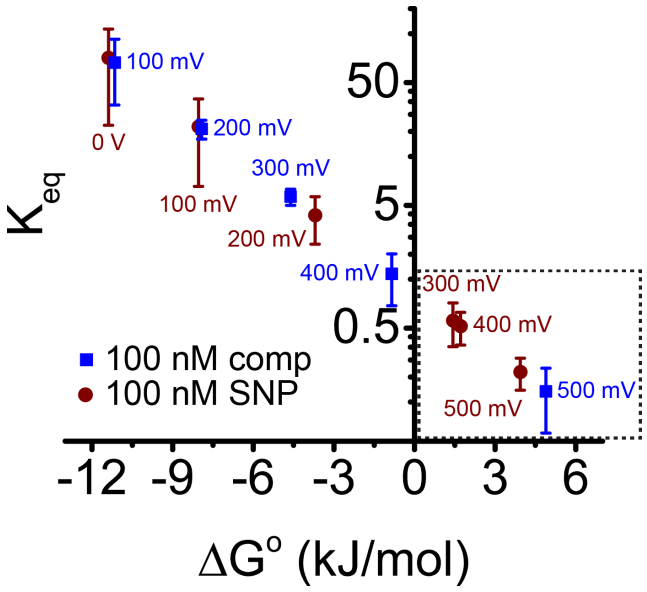

Figure 3.18: Equilibrium constant K_{eq} versus ΔG° for 100 nM fully complementary and SNP strands.

SNR for Bias-dependent Studies

Once a complementary ssDNA is introduced at a system temperature of 40 °C, bias-dependent melting and hybridization events are not observed unless a potential is applied, as illustrated in Figure 3.19. With increasing potential, melting events, reflected by a lower conductance state, become longer and more frequent. The SNR, calculated in this context as the difference between conductance states divided by the full-width half maximum (FWHM) of the upper conductance state ($\frac{\Delta I}{I_{high,\ FWHM}}$), is sufficient to resolve ΔI's at all bias points.

Signal specificity was further demonstrated by analysis of SNR of a two-state signature of a fully complementary strand. The dependence of SNR on gate bias, as shown in Figure 3.20, reveals an increasing trend indicating that bias-modulated performance of the device was not responsible for the obtained signals.

3.3.4 Surface versus Solution-based Hybridization Diffusion

The concentration dependence of k_{hyb} in our system is noteworthy. In order to better understand this, one should comprehend the discrepancy between surface-based (1D) and

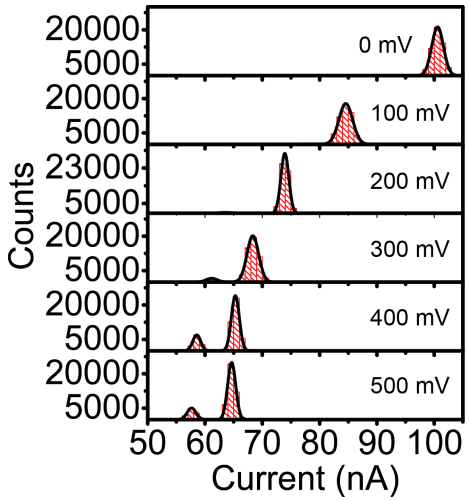

Figure 3.19: At $V_g = 0$ V, one state is evident, whereas at all other solution biases, two-state activity is evident.

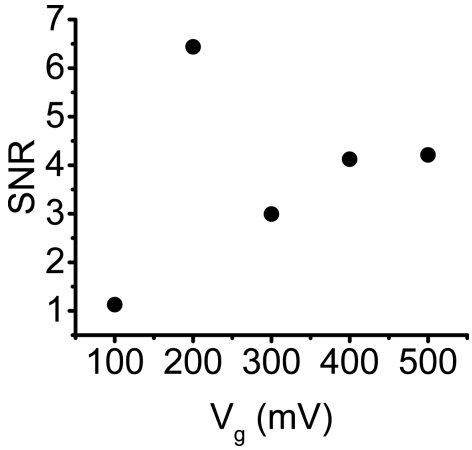

Figure 3.20: Even though the smFET device performance is modulated by the solution bias, there is also a general trend toward higher signal-to-noise ratio (SNR) with increased bias. This observation signifies that we are sensing a single-molecule and not just purely changing device characteristics.

bulk (3D) diffusion modes impacting hybridization. Different rate constants were used to describe the dominant hybridization mode of the lower (1 nM, 10 nM) and higher (100 nM) target concentrations. At low concentrations, 1D diffusion coefficients are faster due to reduction-of-dimensionality (RD) enhancement [80] and fewer target molecules adsorbed to the CNT surface. Above a certain concentration, however, 1D diffusion coefficients are considerably decreased (1D diffusion coefficients are inversely proportional to adsorbed targets concentration [81]), leading to a faster 3D diffusion which now dominates the hybridization rate and is better described by the fast rate constant. From the perspective of RD rate enhancement, which has previously been validated in biochemical systems [80], these distinctions are expected.

The rate assignments are summarized in Table 3.1 and illustrated in Figure 3.21. At 100 nM concentration, the 1D diffusion is slow; at low (1 nM, 10 nM) concentrations, the 1D diffusion is fast (Figure 3.21a), consistent with surface-based ensemble studies [82, 83]. This behavior arises from the fact that the reaction on the surface is diffusion-limited for the high concentration, but reaction-limited for lower concentrations. Conversely, at 100 nM concentration, the 3D diffusion is fast (reaction-limited); at lower concentrations, the 3D diffusion is slow (diffusion-limited), as shown in (Figure 3.21b). Bias helps elevate k_{hyb} only for (1D) surface mode at the higher concentration (100 nM), meaning that potential energy is used to overcome steric hindrance and electrostatic effects. Upon the application of 300 mV bias (Figure 3.21c), the 1D hybridization with 100 nM is increased (versus the scenario with no applied bias, $V_g = 0$ V).

Despite all of this, the two hybridization modes are not completely deconvolved by taking the low and fast time constants from double-exponential fits to the appropriate survival plots. At low target concentrations, the slow rate is dominated by the 3D mode but is still influenced by 1D binding. Similarly, for higher concentration, the fast rate (representing the 3D mode, as alluded to before) is likely to be influenced by 1D hybridization events as well. The transition between the dominant rate constants is revealed based on the ratio of 1D to 3D diffusion and on the target concentration. This transition point be-

tween rate-determining steps, occurring at a concentration of 100 nM, has been previously quantified [82].

The melting rates (chosen to represent the 3D process, as is the case for the hybridization reaction) show no concentration dependence but a strong temperature dependence (Figure 3.21d).

	Surface (1D diffusion)	Solution (3D diffusion)
100 nM	τ_{slow} diffusion-limited due to steric effects at CNT surface	τ_{fast} reaction-limited due to large number of DNA molecules available to hybridize
1 & 10 nM	τ_{fast} reaction-limited due to reduced competition from adsorbed DNA species	τ_{slow} diffusion-limited due to low number of DNA target molecules

Table 3.1: Surface versus solution diffusion modes describing hybridization.

3.4 Measurement Setup

The measurement setup consists of a polydimethylsiloxane (PDMS) microfluidic channel for interfacing solution with the fully fabricated smFET devices, a custom-made printed circuit board (PCB) for data acquisition, and a temperature sensor/controller for setting and modulating the temperature in the vicinity of the chip surface. A cartoon of the PDMS channel and fabricated chip juxtaposed is shown in Figure 3.22. All details regarding the electronic hardware were thoroughly outlined in Chapter 2.

The PDMS microfluidic mold is formed from a thick patterned SU-8 layer. Cured microfluidic channels have the following dimensions: 7 mm long, 750 μm wide, and roughly 500 μm tall. Inlet and outlet holes are punched into the channel, and two sterile tubing segments are inserted. A syringe pump connected to the outlet terminal withdraws fluid exiting the channel, thus allowing full control of flow rates.

Temperature control is achieved by using a commercially-available Thermostream©

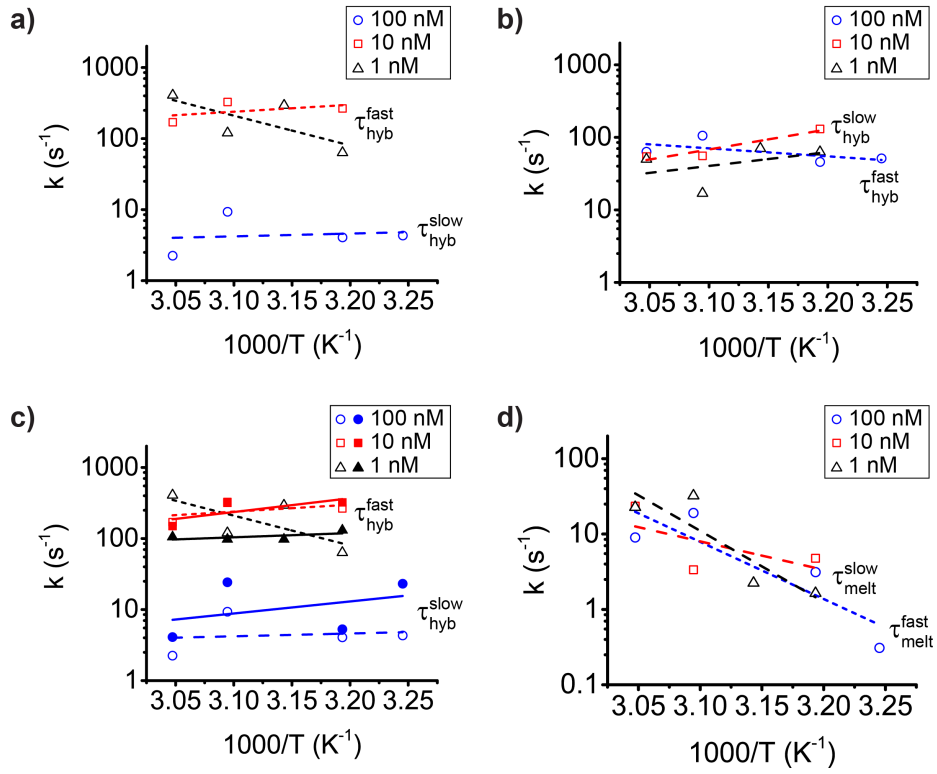

Figure 3.21: a) Surface-based (1D) hybridization as a function of temperature, characterized by τ_{hyb}^{slow} for 100 nM (blue circles) and τ_{hyb}^{fast} for 10 nM (red squares) and 1 nM (black triangles). The rates are comparable for 1 and 10 nM concentrations, but reduced for 100 nM. b) Solution-based (3D) hybridization as a function of temperature, characterized by τ_{hyb}^{fast} for 100 nM (blue circles) and τ_{hyb}^{slow} for 10 nM (red squares) and 1 nM (black triangles). The rates for the 100 nM concentration are no longer considerably reduced. c) Surface-based hybridization, as a function of temperature, with and without applied bias. Open shapes and dashed lines indicate rates at $V_g = 0$ V, and filled shapes and solid lines designate rates at $V_g = 300$ mV. With applied bias, rates for 100 nM are increased, but are hardly affected for 1 and 10 nM. d) Solution-based melting rates as a function of temperature at $V_g = 0$ V. Melting rates are not concentration-dependent.

unit capable of monitoring and modulating the temperature of forced air within a manufactured enclosure surrounding the fabricated chip and microfluidics. The temperature is allowed to reach steady-state before an experimental condition is recorded.

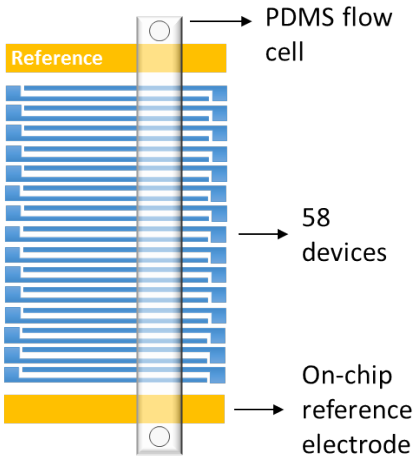

Figure 3.22: An illustration of a PDMS flowcell superimposed on a 58-device electrode pattern. The pseudo-reference electrodes are situated near either end of the flowcell.

3.5 Data Analysis

All data presented is analyzed off-line after the completion of a single-molecule experiment. Once acquired through the FPGA-to-PC interface, data is post-processed using customizable MATLAB scripts. Local drift for five minutes of transient recording from each measurement channel is systematically removed. Resulting signals are low-pass filtered with a 4^{th} order Butterworth filter to 1 kHz to eliminate noise close to the cutoff frequency of the anti-aliasing filter of each measurement channel. Every trace is further analyzed using the aforementioned iterative event detection algorithm [64]. Traditionally, this single-molecule data analysis methodology is applied to evaluate current blockades due to nanopores, but the same technique can be extended to any signature with two-state RTN.

The Hidden Markov Model (HMM) is the hallmark of analysis techniques for transient single-molecule data. Many software packages have been created for this – notably, QuB [84] and vbFRET [85]. Compared to the Markovian signal processing paradigm, the iterative detection algorithm utilizes rudimentary statistical metrics (moving average, RMS noise level, etc.) rather than Markovian matrices and machine learning principles [86]. The figure below (Figure 3.23) shows a comparison of 1-second real-time signal trajectories overlaid with idealized trajectories generated via iterative event detection and HMM tech-

niques. The outputs are comparable, yet the execution times for 5-minute long traces are longer with HMM analysis (60 minutes versus <2 minutes for the iterative event detection algorithm). Faster execution speed allows for more rapid tuning of parameters by the user.

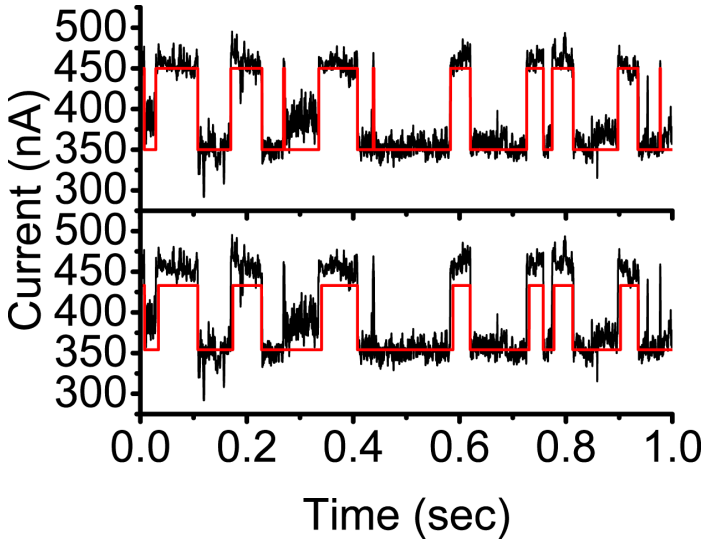

Figure 3.23: Identical 1-second long real-time traces (black) overlaid with red idealized traces output by iterative event detection algorithm (top panel) and HMM analysis (lower panel). The latter analysis is unable to track some events recognized by the former algorithm.

Idealized traces are used to extract single-molecule binding kinetics information. Each idealized data trace for a given experimental condition is divided into five equal parts, from which dwell time histograms (and subsequently survival probability plots) are constructed for high and low conductance states (assuming the same two-state model as before). Average kinetic DNA hybridization/melting rates and associated error bars are calculated from them. Algorithms for this portion of the analysis are adapted from HaMMy scripts previously written in MATLAB [87].

A sample data analysis flow, encapsulating the preceding information, is shown in Figure 3.24.

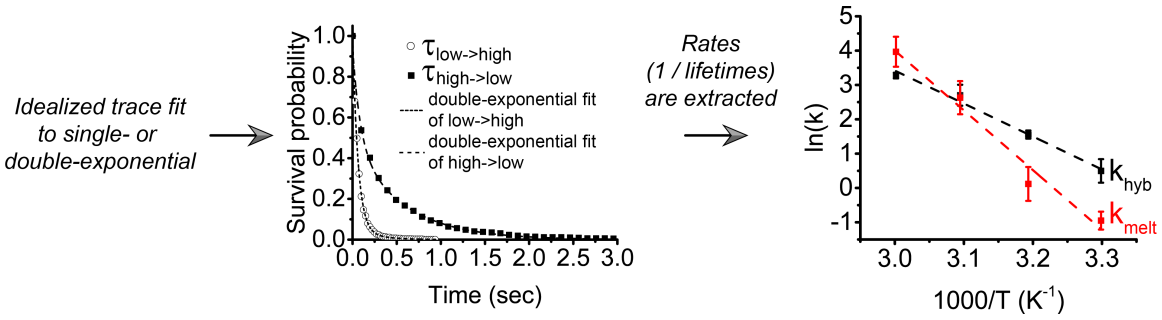

Figure 3.24: Data analysis flowchart.

3.6 Enhancements to This Study

Further enhancements to this study include:

- Increasing the yield of devices with single tethered probe DNA oligos. This involves tuning the reaction chemistry to achieve, on average, one sidewall defect per nanotube across the device array.

- Elucidating the mechanisms governing the concentration-dependent hybridization and melting kinetics as a function of both temperature and bias

3.7 Electrostatic-driven Melting Summary

In summary, we have developed an all-electronic approach to observe hybridization kinetics as a function of temperature and solution bias. We have demonstrated that, with electronic control, we can influence the melting kinetics and reaction thermodynamics in a manner equivalent to temperature. An array of smFET devices was utilized to transiently sense differences of two different 20-mer oligonucleotide sequences – a complementary strand and a single-nucleotide polymorphism of an Ebolazaire virus strain – thus demonstrating the single-nucleotide sensitivity of this sensing modality. These proof-of-concept studies pave the way for further work in the application of smFETs to genomic assays.

Chapter 4

Wafer-scale Fabrication of Spin-cast smFETs

4.1 Introduction

Applications involving single-walled carbon nanotubes (SWCNTs), such as display technologies, next-generation field-effect transistor architectures, and biotechnology, have been explored for more than two decades. Thin-film transistor applications, making use of networks of nanotubes to provide enhanced mobility and electrical transport characteristics for displays [88, 89] and high drive currents for digital logic [90], have been heavily studied. In semiconductor FET applications, for instance, the inclusion of metallic SWCNTs in the FET channel reduces the on/off current ratio, in turn diminishing device performance. Sensors have been designed using arrays of nanotubes, which are compatible with conventional carbon chemical functionalization strategies [2], as the channel material. In the majority of these application areas, nanotubes are generally grown on a catalyzed flexible or solid substrate to form randomly- or directionally-oriented CNT networks, in an effort to maximize the number of nanotubes. Growth conditions typically yield tube lengths on the order of a few millimeters, allowing for electrical contact to many devices [37]. Despite the generally pervasive use of as-grown nanotubes today, traditional fabrication approaches employing

[0] Information from this chapter is unpublished (at the time of this writing).

them with custom-fashioned electrodes are tedious [91], yielding very few devices for significant fabrication effort, and not scalable to wafer-scale processing. Additionally, the chirality of each nanotube, indicative of the carbon lattice structure and the diameter, can vary [92], increasing the amount of characterization required per device during fabrication.

Attention has recently been devoted to solution-processable nanotubes. While these types of nanotubes tend to be shorter than the CVD-grown variety (single μm versus many μm) due to sonication, they enable more rapid, simplified device fabrication. In one deposition approach, dielectrophoresis is exploited to achieve deterministic nanotube alignment, yet this technique presents significant manufacturing challenges. Sorted nanotubes wrapped in polymer have been studied as well, by which the solubilized polymer helps to reduce inter-tube interactions – thereby limiting bundling – and preferentially sorts for p-type semiconducting tubes – yielding nanotubes with similar electronic properties. Studies of concentrated solutions of polymer-wrapped nanotubes range from improved photoluminescent properties [93, 94] to solution-processed nanotube networks composed primarily of semiconducting SWCNTs [95, 96]. Still, such networks are prone to significant device-to-device variability due to the large variance in inter-nanotube resistance.

Although dense nanotube networks are advantageous for the application spaces above, they are not conducive for real-time single-molecule sensing, which relies on the successful incorporation of one SWCNT bridging each source-drain electrode pair. We seek a deposition approach (as opposed to a growth process) which is simple, scalable, and reproducible. We wish to deposit nanotubes *in-situ* onto alternate substrates for large-scale production, without having to rely on mechanical transfer [97].

Instead of fashioning electrodes to nanotubes as they appear on an as-grown substrate, we develop a streamlined fabrication flow for spin-cast smFET transducers on 100-mm wafers. We attain this by utilizing a single spin cycle to randomly deposit as-grown (unsorted) CNTs dispersed in deionized (DI) water onto a SiO_2 surface in lieu of growing them *in-situ*, thus avoiding arduous processing steps. We obtain a yield of single-nanotube crossings close to 30% with the patterning of a fixed electrode configuration. In order for

this spin-cast process to be manufacturable at the wafer-level, it must be simple enough for fabrication engineers to reproduce and compatible with conventional lithography and physical vapor deposition equipment. None of the previously mentioned fabrication approaches satisfy both requirements.

For the first time, we demonstrate the feasibility of sensing the hybridization and melting behavior of a tethered 20-mer oligonucleotide from the Ebolavirus sequence and its fully complementary strand, which manifests itself as a random-telegraph-noise (RTN)-like signal, using solution-processed SWCNTs. Real-time biosensing with smFET transducers has been previously reported on [32, 34, 59], but they were designed with CVD-grown devices. We further demonstrate the benefit of our scalable method by fabricating spin-cast devices on 4" wafers, which augments fabrication throughput and enables translation of our approach to wafer-scale production of CMOS die.

4.2 Simulations for smFET Yield

Prior to fabrication of field-effect transistors, simulations of randomly distributed CNTs were performed to model the expected number of nanotubes bridging zigzag-shaped electrode pairs as a function of areal nanotube density (in CNTs/μm^2) and electrode width (in μm, analogous to MOSFET width). Our principal goal is to incorporate one nanotube per electrode pair. Wide electrodes are expected to permit multiple contacted nanotubes; higher nanotube densities, to an extent, are likely to cause nanotube aggregates. Either situation is detrimental for the smFET sensor topology. Hence, understanding the impact that altering nanotube density and electrode width has on the number of CNTs is critical.

To assess how the number of nanotube transits scales with density and electrode width, statistics are collected over 500 electrode pairs. We make the following assumptions:

- The placement of nanotubes follows a continuous uniform probability distribution
- The density of nanotubes in a constrained simulated area is uniform
- A log-normal distribution with random variable X, a mean of $\log(X)$ of -0.36 μm, and

a standard deviation of $\log(X)$ of 0.6 μm governs the nanotube length. These values were computed from more than 1200 CNTs identified with scanning electron-beam microscopy (SEM), and is also commensurate with statistical data provided by the SWCNT vendor.

- Channel length (spacing between electrodes) is fixed at 0.5 μm, consistent with the device pattern to be fabricated
- Electrode height is fixed at 10 μm.
- The only tunable parameters are nanotube density and electrode width

Simulations are run with a nanotube density ranging from 0.05 CNTs/μm^2 to 0.2 CNTs/μm^2 and electrode width from 15 μm to 25 μm. Two representative simulation outputs are shown in Figure 4.1. Both increased nanotube densities and wider electrodes are expected to lead to a higher occurrence of nanotube-electrode contacts.

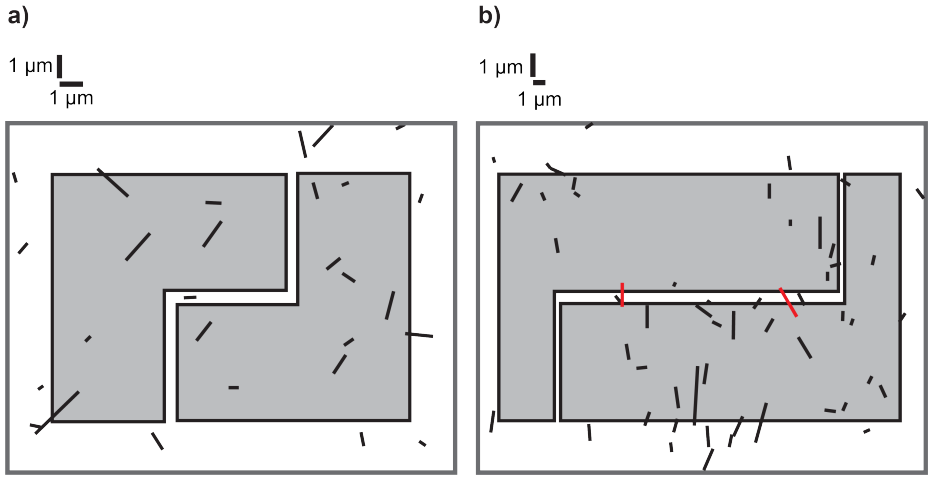

Figure 4.1: Representative simulation outputs for zig-zag electrode pairs, with a) nanotube density of 0.1 nanotubes per μm^2 (corresponding to 28 nanotubes simulated) and short electrodes (5 μm), and b) nanotube density of 0.1 nanotubes per μm^2 (corresponding to 56 nanotubes simulated) and wide electrodes (25 μm). The thick outer bounding box delineates the area over which nanotubes are allowed to deposit. The filled gray rectangles denote the source and drain electrodes. Black lines indicate deposited CNTs that are not properly oriented to transit the electrode gap, and red thick lines indicate CNTs that do traverse the gap. Clearly, simulations with the wider electrodes show that the probability of trapping two CNTs is higher. In both instances, the electrode gap is 0.5 μm and the electrode height is 10 μm.

Figure 4.2 presents contour plots of the percentage of zero, one, and multiple simulated nanotubes per electrode pair as a function of electrode width and CNT density. There is inherently a tradeoff between optimizing for one nanotube crossing while limiting the number of zero or few crossings. As the nanotube density and electrode width increase, the probability of zero crossings decreases, yet the likelihood of having double crossings increases. The probability of incorporating only one nanotube between an electrode pair increases with electrode width and nanotube density. For instance, the probability of incorporating exactly one nanotube between a 20 μm wide electrode pair is slightly greater than 30% for nanotube densities between roughly 0.15 and 0.2 CNTs/μm^2. The theoretical maximum yield of single CNT crossings, dictated by Poisson statistics, is $P(1) = 1/e \approx 36\%$.

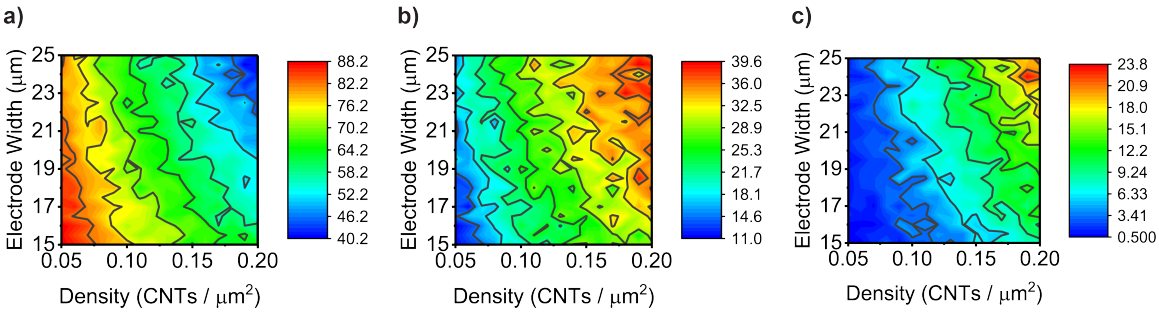

Figure 4.2: Simulated percentages of (a) zero, (b) one, and (c) multiple (2+) CNT crossings per electrode pair as a function of electrode width and CNT density.

4.3 4" Wafer-scale Fabrication

Previously, passive smFET arrays employing nanotubes grown by chemical vapor deposition were fabricated in Columbia's fabrication facility. However, the CVD growth parameters limited the number of usable biosensors per chip, as well as the chip size.

Using the simulation results as a guide, passive arrays of spin-cast smFET devices are fabricated on 100-mm oxidized silicon (Si/SiO_2) wafers. To realize these arrays, nanotubes from a stock suspension of as-grown nanotubes (via arc discharge method) in deionized (DI) water with sodium cholate (SuperPureTubes) were purchased from NanoIntegris, Inc.

These suspensions are further diluted in DI water without additional surfactant, rendering them stable and free from nanotube agglomeration over periods longer than one month. Suspensions are briefly vortexed and sonicated before spinning. The sonication time is short, which is advantageous for preserving nanotube length and minimizing sidewall damage [98].

Before spinning nanotubes, wafers are treated with oxygen plasma to promote wetting and surface adhesion of the aqueous nanotube suspensions. To fully coat the wafer top surface, $\geq$1-2 mL diluted aqueous suspension is pipetted. We employ a two-step spin-coat recipe (400 rpm and 100 rpm/second for 20 seconds, followed by 3,000 rpm and 10,000 rpm/second for 45 seconds). The first step is optimized to slowly spread the solvent across the sample surface. The second step, occurring at a faster spin speed, is intended to rid excess solvent, obviating the need for additional wash or rinse steps. Consequently, nanotubes are randomly aligned on the sample surface.

We find that the dispersal of nanotubes across the sample surface is weakly dependent upon the final spin speed. In this regard, we believe optimization is strongly dependent on two fundamental spin coating parameters: solution concentration and mask geometry. The surface concentration of nanotubes used is 0.13 $\pm$ 0.18 CNTs/μm^2, assessed from eleven SEM micrographs (field of view is 500 μm^2) of the wafer post-spinning.

After spinning nanotubes, bi-layer DUV resist is spun (copolymer EL7 at 4,000 rpm for 1 minute, followed by 950K PMMA A2 at 2,000 rpm) and exposed using a DUV stepper. electrical contact areas are patterned in a vertical pattern spanning 8 mm of each chip length (Figure 4.3a); on one wafer, forty-five 1$\times$1.1 cm^2 die are patterned. Titanium (50 nm) is deposited in these regions, making 280 source-drain electrical pairs (organized into 70 groups of four). The area over which a single SWCNT can bridge source and drain electrodes is restricted geometrically: 20 μm wide with a contact separation of 0.5 μm (Figure 4.3b,c).

After liftoff of the Ti layer, two platinum (Pt) bars (each $\sim$100 nm thick), acting as on-chip pseudo-reference (gate) electrodes, are deposited on either end of the electrode array (Figure 4.3d,e). Candidate individual SWCNT devices are electrically isolated in a

similar fashion to the CVD-grown devices: in an additional lithography step, nanotubes between the electrodes are protected by photoresist, while all other nanotubes are blasted away with oxygen plasma for 20 seconds at 50 W (Figure 4.3f). Compared to an example process for CVD-grown nanotubes (Figure 3.3), which involves a time-consuming growth procedure (step a) followed by a labor-intensive search for CNTs via SEM, it is clear that the spin-cast process is more streamlined.

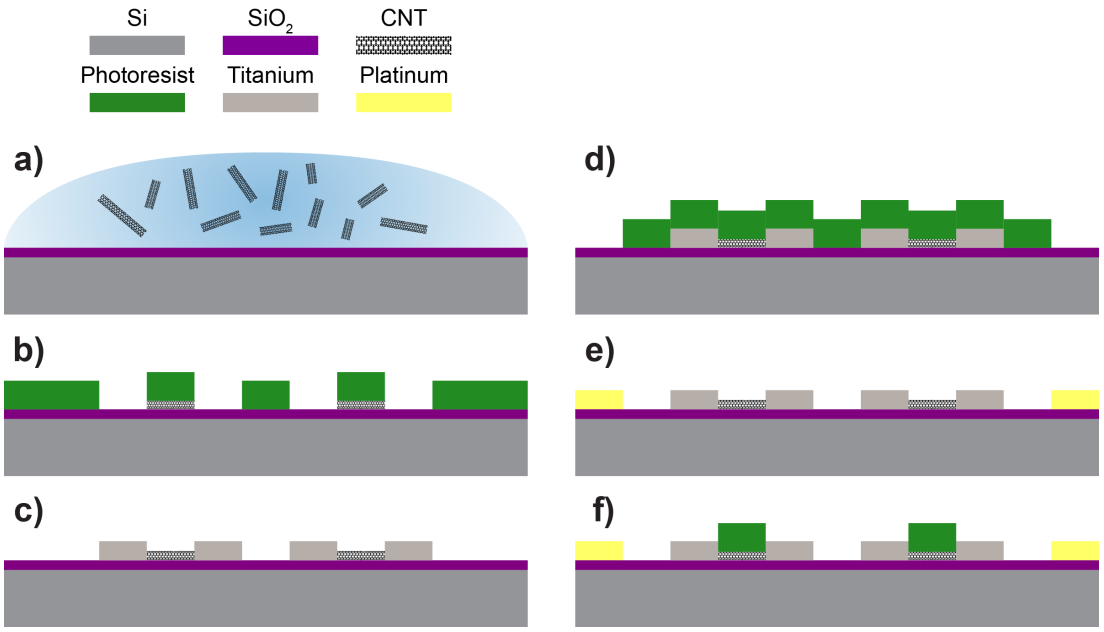

Figure 4.3: a) Spin-casting of carbon nanotubes in organic solvent. b) Lithography patterning for source and drain titanium electrical contacts. c) Titanium deposition and subsequent photoresist removal. d) Patterning for pseudo-reference platinum gate electrodes. e) Platinum deposition and subsequent photoresist removal. f) Patterning for etching of non-passivated nanotubes, outside the device channels, with oxygen plasma.

Lastly, devices are annealed in vacuum (350 °C for 15 minutes) to enhance the nanotube-metal contact and remove residual surfactant from the nanotube sidewalls, rendering them clean for chemical functionalization.

4.4 Results

Refer to Figure 4.6a for a photograph of one 4" wafer produced using fabrication facilities at Cornell University. Before wafer dicing, we are able to construct a spatial distribution of

single-nanotube crossings to ascertain spin uniformity. As depicted in Figure 4.4, the spread of single-nanotube crossings is approximately 11 to 16%, with the highest yield observed in the center of the wafer.

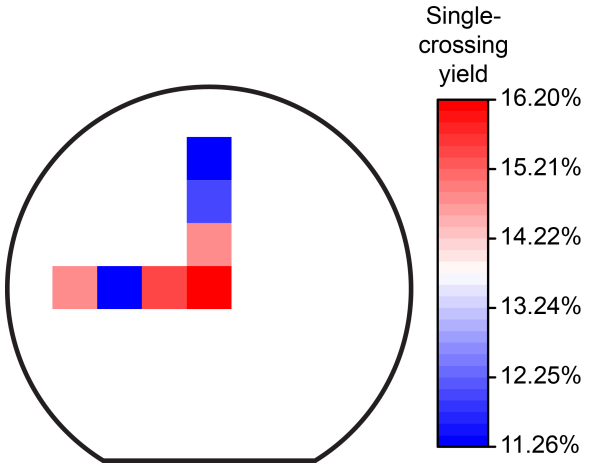

Figure 4.4: Estimated 4" wafer yield of single-nanotube crossings as a function of wafer location. Wafer flat is shown. Seven chips were inspected by SEM in a reverse 'L' shape on the wafer.

Wafers are subsequently diced into individual die for further metrology and electrical characterization. A representative set of die (colored squares in Figure 4.6b) is chosen to validate the simulation results experimentally and to identify single nanotube crossings. All electrode pairs on three of these chips are imaged with SEM. The statistical results from these scans are overlaid with simulations (repeated ten times) of the same electrode geometry and CNT surface concentration (0.13 CNTs/μm^2), showing comparable single-crossing yields (Figure 4.5).

Back-gated current-voltage (I-V) measurements in air are performed to ensure the smFET devices electrically conduct after all processing steps. A constant source-drain voltage of 100 mV is applied while the back-gate voltage (V_{bg}), applied to the heavily-doped p^{++} Silicon substrate, is swept in air from –10 to +10 V.

Representative micrographs of nanotube crossings, taken at various locations on a single die, are shown in Figure 4.6c, illustrating the reproducibility of single-device crossings across the electrode array. SEM images of electrode arrays are captured only at electrode sites which exhibit good back-gating characteristics (I_{on} / I_{off} exceeding $\sim 10^3$ for p-type

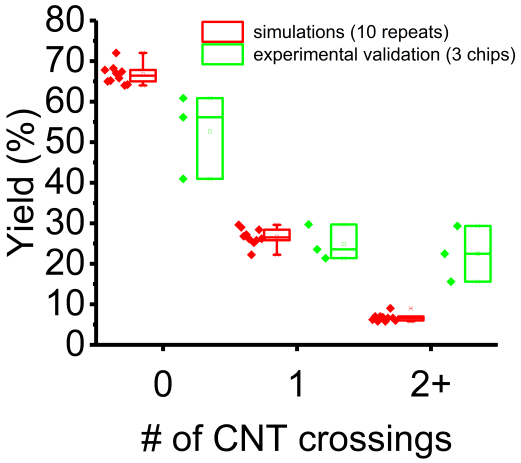

Figure 4.5: Boxplots are shown in red for the number of CNT crossings resulting from spin-cast simulations (run ten times), and in green for the number of crossings experimentally validated with full SEM scans of three die.

semiconducting devices and ∼1-100 for semi-metallic (ambipolar) devices) and show appreciable current levels in the single to hundreds of nA range (see Figure 4.7).

Histograms (Figure 4.6d) are drawn from this population of devices. Note that the single-crossing yield estimate from simulations (26.8%) in Figure 4.2 is higher than the experimental single-crossing yield (13 ± 3.9%) shown in Figure 4.6d. This discrepancy can be attributed to the fact that simulations only predict the nanotube distribution before lithography; they do not account for nanotubes which do not electrically conduct yet appear to be trapped between source-drain electrodes in an SEM image.

The number of zero-crossings is high, which is to be expected from a random-placement-based spin-cast deposition approach. Statistics roughly conform to a zero-inflated Poisson distribution, defined as:

$$P(k) = \begin{cases} \sigma + (1-\sigma)e^{-\lambda} & k = 0 \\ \frac{(1-\sigma)\lambda^k e^{-\lambda}}{k!} & k > 0 \end{cases} \tag{4.1}$$

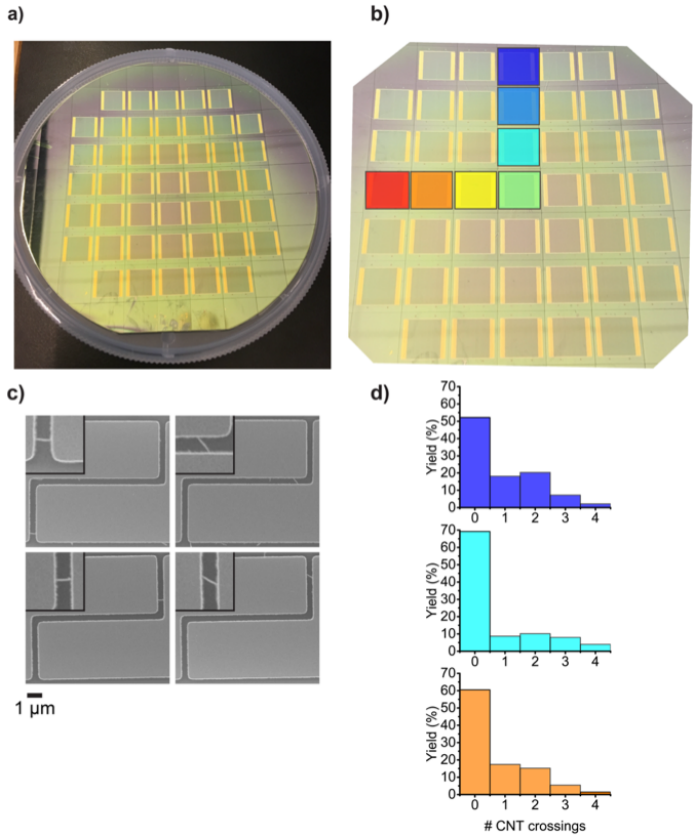

Figure 4.6: a) Top-down photograph of fully processed 100-mm Si/SiO_2 wafer, comprised of 45 individual 1×1.1 cm^2 reticles. b) Representative chips for electrical characterization, mapping out a reverse 'L' shape on the wafer. Since the wafer is radially symmetric, the statistics collected from these chips constitute a representative sample set. c) Representative SEM scans of single-nanotube crossings. Insets show a zoomed-in view. d) Histograms of three of the seven representative die on the wafer (colors match the filled squares in panel a). The non-zero crossings are verified with both SEM imaging and back-gated I-V sweeps.

4.4.1 Chip Preparation for Testing

After initial electrical characterization and the identification of single-nanotube devices, we perform point functionalization of the characterized devices to create smFETs using the nanowell method outlined earlier [59]. In short, devices are patterned with PMMA nanowells 30 nm wide and 30 nm deep over the nanotubes and subsequently exposed to FBDP to create single attachment sites on the exposed nanotube sidewalls in the wells. Chips are then wirebonded to interface with the custom printed circuit board (see Chapter 2).

The same type of PDMS microfluidic chamber used in Section 3.4 is employed here.

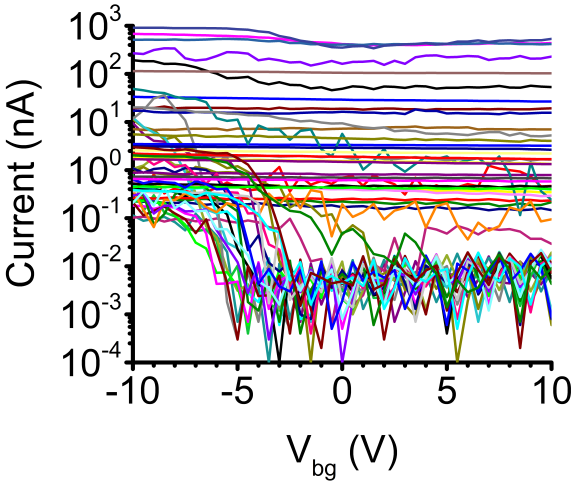

Figure 4.7: Back-gated transport characteristics of aqueous CNT suspensions. I-V measurements in air for 56 representative single-crossing nanotube devices, with the silicon back-gate swept from –10 V to +10 V and a constant V_{sd} of 100 mV. A mix of semi-conducting and semi-metallic tubes is evident.

Once PDMS is peeled from the corresponding SU-8 mold, it is cut and affixed to the fabricated chip surface using micromanipulators to precisely control its placement. Temperature is controlled inside a custom acrylic enclosure with parallel resistive silicone heaters (12 V_{max}), a DC fan, and a thermocouple, as described in subsection 2.4.2.

4.4.2 Device Characterization in Electrolyte

Electrolytic-gated I-V characteristics (Figure 4.8) are measured in 100 mM alkaline sodium phosphate (PB) buffer at pH 8.0. Devices are operated in the triode regime with a fixed source-drain bias (V_{sd} = 100 mV) and variable solution gate (V_{lg}) bias relative to the source potential that is swept from –0.5 to 0.5 V on platinum electrodes. These devices show the same semi-metallic and semiconducting gating behavior evidenced by back-gated electrical measurements.

Output curves for one representative device at three V_{lg} biases (–100 mV, –300 mV, and –500 mV) appear in Figure 4.9a, showing resistive behavior across the bias range. This confirms that the typical V_{sd} voltage applied during smFET device operation (100 mV) is in the triode regime. The majority of devices show source-drain resistances in the range of 0.2 to 5 MΩ, as evidenced by Figure 4.9b-d. Measurements of test structures show the

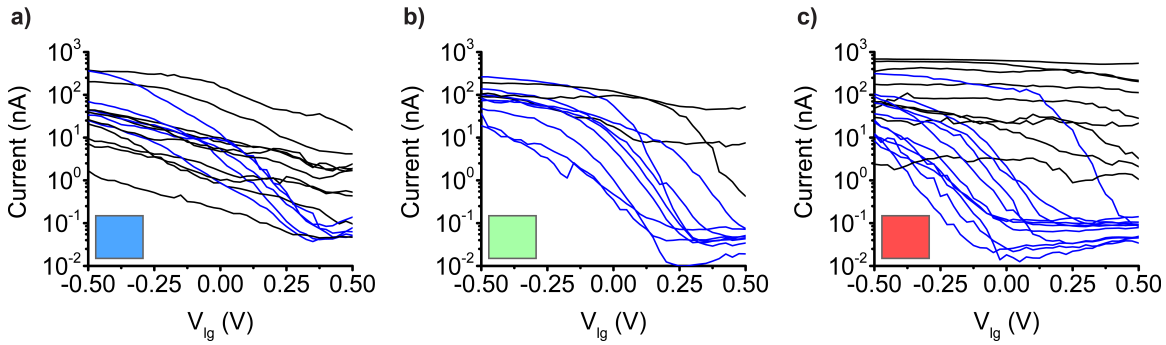

Figure 4.8: Devices on three wirebonded chips are characterized in electrolyte. Liquid gate sweeps of a) 11, b) 11, and c) 20 unsorted nanotubes deposited on three wirebonded chips are recorded. The colored square in each panel corresponds to the same squares from Figure 4.6. Semi-metallic devices are highlighted in black; semiconducting in blue.

end-to-end bond pad resistance is roughly 80 kΩ before vacuum annealing, which improves to 57 kΩ after. Thus, we are confident that the nanotube resistance is the dominant lumped element of the nanotube-electrode interface.

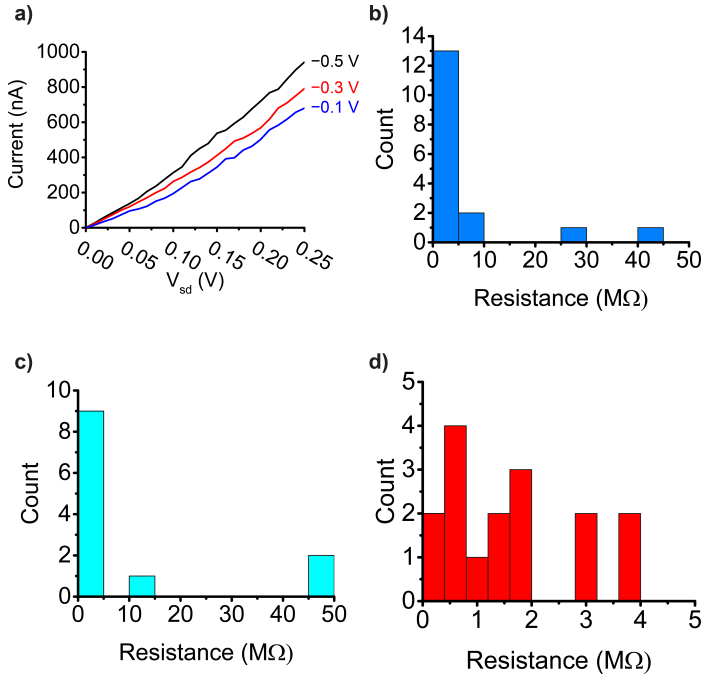

Figure 4.9: I-V_{sd} family of curves measurements in water for one representative single-crossing nanotube device and three liquid gate voltages.

4.4.3 Thermodynamics of Single-molecule DNA Hybridization-Melting

After initial I-V sweeps in the sensing buffer, devices are incubated within the microfluidic cell with 20-mer probe DNA overnight (10 μM) to covalently tether a single DNA strand to the generated attachment site. I-V sweeps are recorded again, after which 20-mer fully complementary target DNA is introduced into the microfluidic cell.

To demonstrate the ability of the spin-cast smFET to function as a fully electronic single-molecule transducer, we sense temporal probe-target DNA interactions through repeated hybridization and melting in an aqueous electrolyte. This sensing modality was also explained thoroughly in Chapter 3. In previous electrostatic single-molecule studies [99], this sensing was attained with a bias-dependent modulation scheme, whereby the bias between the device and the surrounding electrolyte was varied to promote DNA unzipping. In short, in a dominantly temperature-controlled salt environment, the hybridization equilibrium constant $\mathrm{K}_{eq} = \mathrm{k}_{hyb} \,/\, \mathrm{k}_{melt}$ of the reaction, related to the free energy change ΔG°, is thermally actuated and is governed by the van't Hoff expression (Equation 3.5). With the addition of positive solution bias versus the nanotube, the energy barrier for the reaction is lowered and is proportional to the magnitude of the applied bias. This bias dependence can be modeled according to Kramers' rate model for thermodynamics as

$$K_{eq} = e^{\frac{-\Delta G^{\circ} - Q_{eff} V_{lg}}{k_B T}} \tag{4.2}$$

where $\mathrm{Q}_{eff}\mathrm{V}_{lg}$ represents the amount by which the energy barrier reduces [76,100]. Melting is preferred relative to hybridization ($K_{eq} < 1$) as more positive solution bias is applied, due to electrostatic repulsion of the negatively charged DNA backbone from the nanotube surface [69, 101].

Figure 4.10a presents real-time signatures and idealized fits of the source-drain current at three disparate V_{lg} values and one fixed temperature (T = 40 °C), revealing two-state hybridization-melting events manifested as RTN-like behavior. Transitions between the two discrete conductance states define hybridization (k_{hyb}) and melting (k_{melt}) rates which slightly deviate from a well-characterized two-state model of hybridization and melt-

ing. Real-time control measurements of the probe molecule in the presence of 100 nM fully non-complementary DNA do not show any two-state RTN-like activity, as displayed in Figure 4.24.

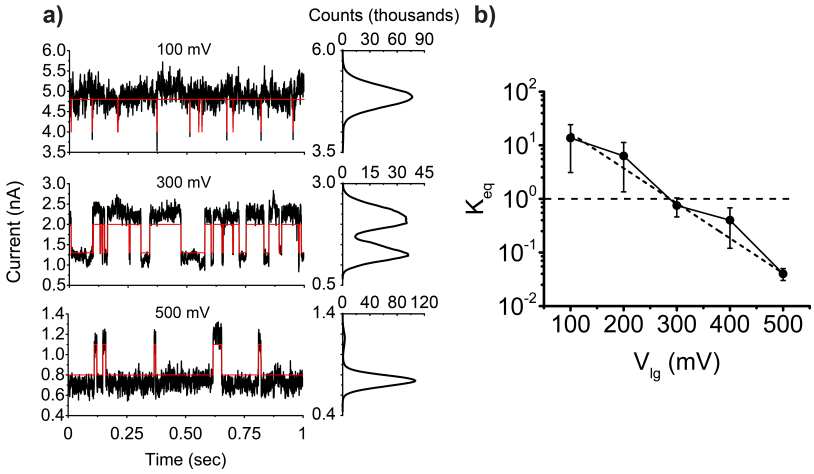

Figure 4.10: Thermodynamics of DNA duplex association and dissociation. a) 1-second transient current recording from a defected spin-cast smFET in the presence of 100 nM complementary DNA, showing clear two-state behavior over the bias range and measurement interval. $V_{sd} = 100$ mV is used. Histograms are computed for the shown measurement interval. At low gate bias, the DNA mostly resides in the upper (hybridized) current state (∼4.8 nA). As the bias increases, transitions to the lower (melted) current state become more frequent. The temperature maintained in the electrolyte is 40 °C. The total recording time at each gate bias is 5 minutes. b) The hybridization equilibrium constant K_{eq} as a function of solution gate bias from 100 to 500 mV for T = 40 °C. The calculated electrostatic melting potential E_m (287 mV) gives the minimum electrolyte potential needed to force the DNA duplex to preferentially melt. Over 1000 events are analyzed at each bias point. Error bars represent the standard deviation calculated from at least five segments of 60-sec conductance measurements exhibiting two-state activity.

Figure 4.10b illustrates the bias-dependent equilibrium constant for one smFET transducer measured at various V_{lg} values (0 V to 0.5 V) and two monitored system temperatures (40 and 50 °C). In both instances, the equilibrium constant is modulated by more than two orders of magnitude solely by varying the solution bias. Additionally, when the electrolyte is maintained at the higher temperature, melting of the DNA target from the tethered probe occurs at lower solution biases compared to melting at the low temperature, since the solution at thermal equilibrium is closer to the theoretical melting temperature of the DNA duplex (T_m = 49.4 °C, from the same nearest-neighbor calculation used in Section 3.3.1). This argument is consistent with melting curves extracted from ensemble

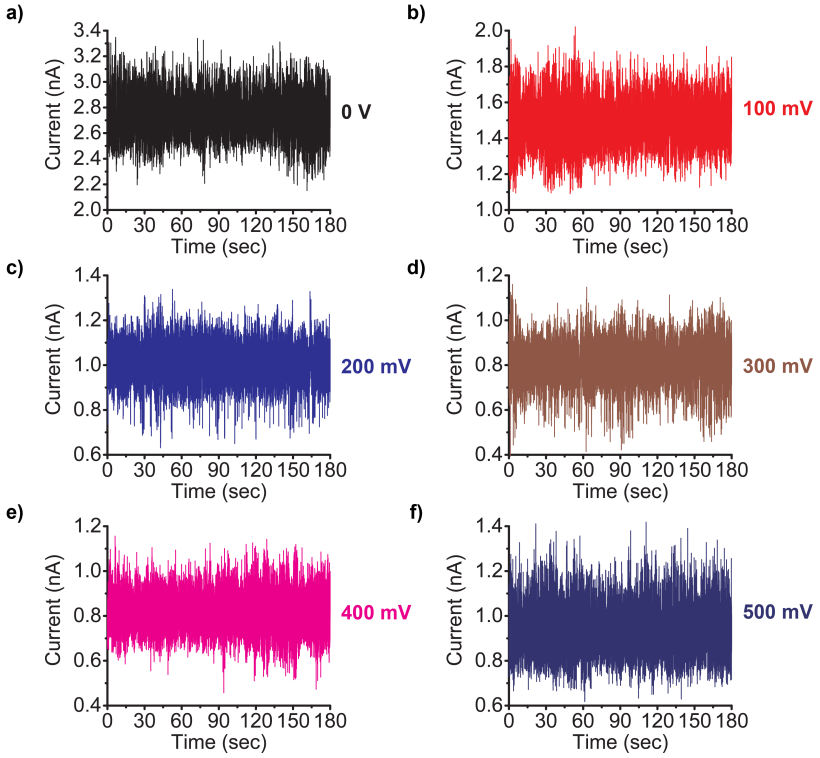

Figure 4.11: Control measurements of an smFET exposed to 20-mer fully non-complementary target DNA strands. Recordings are depicted for V_{lg} of a) 0 V, b) +100 mV, c) +200 mV, d) +300 mV, e) +400 mV, and f) +500 mV. The recording length is 180 seconds.

experiments. Hence, we can affect the thermodynamics of the reaction by using applied solution bias instead of temperature modulation.

4.4.4 SEM Image Analysis

In various parts of this study, diluted nanotube concentrations (in ng/mL) are correlated with observed nanotube densities (in CNTs/μm^2). To make this conversion, SEM images are post-processed in ImageJ using a ridge detection algorithm [102]. In Figure 4.12, the results of this analysis for one SEM image are overlaid on the original image.

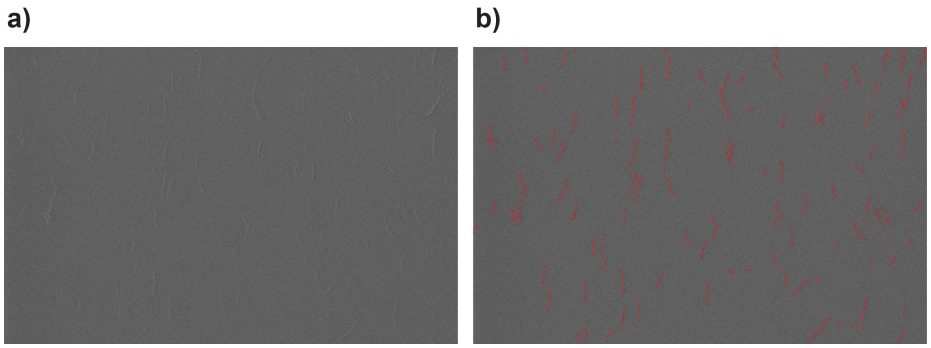

Figure 4.12: Ridge detection algorithm for finding nanotubes in SEM images. a) original image and b) image overlaid with red lines delineating nanotubes found by the ridge detection algorithm.

4.5 Comparative Study of Polymer-wrapped, Chiral-sorted SWCNTs

Although aqueous SWCNTs were used in this study, significant effort was devoted to using polymer-wrapped nanotubes suspended in 1,2-dichlorobenzene (DCB). Cleaned 1×1 cm^2 oxidized Silicon (Si/SiO_2) substrates are used to test spinning conditions for these nanotubes. Suspensions of commercially available as-grown, polymer-wrapped nanotubes in toluene (IsoSol-S100) are purchased from NanoIntegris, Inc. These CNTs are diluted in 1,2-dichlorobenzene (DCB), as depicted in Figure 4.13. We have chosen this solvent on account of its effectiveness in dispersing SWCNTs without additional polymer [103, 104]. These suspensions are stable and over a period longer than one month. Suspensions are then briefly sonicated before spinning; limiting the sonication time is advantageous to minimize nanotube damage and to prevent decomposition/polymerization of the solvent which would otherwise foul the sample surface [105].

Figure 4.14 shows atomic force microscope (AFM) images of two concentrations of CNTs suspended in 1,2-dichlorobenzene (DCB), 5 μg/mL and 500 ng/mL, post-spinning. As shown for the higher concentration, the nanotubes aggregate, forming networks that are not conducive to the smFET topology. In contrast, the separation between nanotubes is larger for the lower concentration, making it easier to electrically contact individual CNTs. Although these nanotubes show measurable D peaks (via Raman mapping), their G^+/D

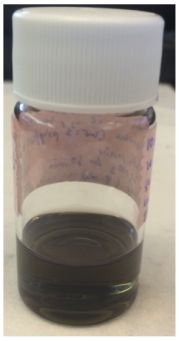

Figure 4.13: Glass vial containing nanotubes suspended in organic solvent. The concentration is fairly high, as evidenced by the grayish color.

ratios are modest: ∼30–40, by inspection (refer to Figure 4.15).

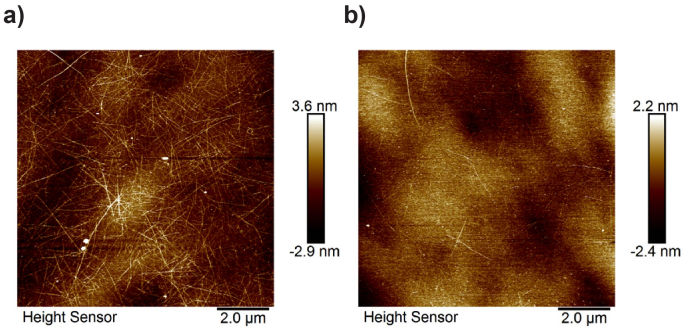

Figure 4.14: Representative AFM images of spin-cast SWCNTs in 1,2-DCB on 1×1 cm^2 Si/SiO_2 surfaces for two concentrations, a) 5 μg/mL, and b) 500 ng/mL.

4.5.1 1×1 cm^2 Die Fabrication

Device arrays are fabricated with nanotubes spun on cleaned 1×1 cm^2 Si/SiO_2 (500 μm of heavily p-doped Silicon and 285 nm of thermally grown silicon oxide) chips. CNTs are diluted by 500× in 1,2-dichlorobenzene and sonicated for a few minutes before spin-coating on 1x1 cm2 Si/SiO_2 die. The resulting suspension is spun using a two-step process: 400 rpm and 100 rpm/second for 60 seconds, followed by 6,000 rpm and 10,000 rpm/second for 20 seconds. Then, bi-layer electron-beam resist is spun on the chip surface (copolymer EL7 at 4000 rpm for 1 minute, followed by 950K PMMA A2 at 2000 rpm for 1 minute) and exposed using a Nanobeam nB4 lithography tool. The rest of the process follows Figure 4.3.

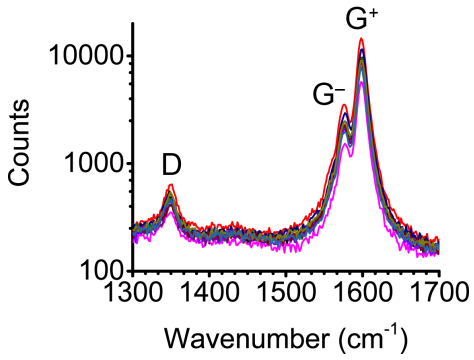

Figure 4.15: Raman scans of 11 individual spin-cast semiconducting SWCNTs. The D (disorder mode), G^- (atomic displacement in the circumferential direction), and G^+ (atomic displacement along the tube) peaks are labeled. In contrast to metallic nanotubes, which have a broad G^- peak, the G^- line shape for these semiconducting tubes is narrow and Lorentzian [106].

4.5.2 Test Electrode Arrays

To converge on reasonable values for both suspension concentration and electrode width, we fabricate test electrode arrays of varying electrode width (5, 10, and 20 μm) and a fixed 1 μm electrode gap in the center of bare Si/SiO_2 samples. Unlike the aqueous SWCNT suspensions, the average nanotube length is expected to be $\sim$ 1 μm, thereby validating the choice of patterned electrode spacing. Three samples are prepared, each with the aforementioned electrode pattern and different concentrations of nanotubes in DCB: 0.03 ± 0.01 CNTs/μm^2, 0.05 ± 0.01 CNTs/μm^2, and 0.23 ± 0.03 CNTs/μm^2.

Histograms at each concentration are constructed from more than 50 nanotubes located by SEM. The data for the highest concentration point (0.23 ± 0.03 CNTs/μm^2) is fit with a Poisson distribution (Figure 4.16a), whereas the lower concentrations (0.05 ± 0.02 and 0.03 ± 0.01 CNTs/μm^2) are fit with a zero-inflated Poisson distribution (Figure 4.16b and c, respectively), owing to the high probability of zero nanotube transits [34] that the spin conditions afford. When using the highest concentration, the expected value of nanotube transits increases with electrode width. Furthermore, the spread of nanotubes is high as well, consistent with the expectation that longer electrodes will trap more nanotubes between them. As the concentration decreases, the distribution of nanotubes becomes narrower, and zero transits are roughly three times more probable than single transits.

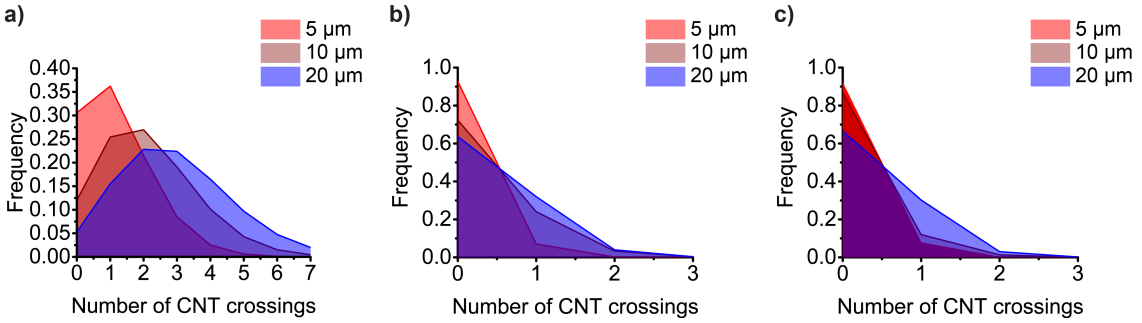

Figure 4.16: Frequency of nanotube crossings as a function of electrode width and average nanotube densities of (a) 0.23, (b) 0.05, and (c) 0.03 CNTs/μm^2.

4.5.3 SEMs, Histograms, and Poisson Statistics

Representative SEM micrographs of nanotube crossings, captured at various locations on one chip, are shown in Figure 4.17, illustrating the reproducibility of single-device crossings across the electrode array. Zero-inflated Poisson statistics are used to assess the frequency of nanotube crossings. σ represents the probability of additional zeros (compared to a standard, non-zero-inflated Poisson distribution), λ is the mean, and k is the discrete random variable.

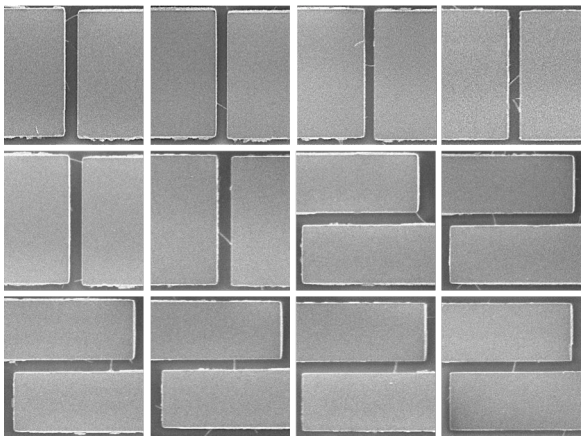

Figure 4.17: SEM gallery, laid out in a 3×4 grid. Both horizontally- and vertically-oriented electrodes are depicted. All images were taken from one fabricated chip, showing that achieving single transits is reproducible.

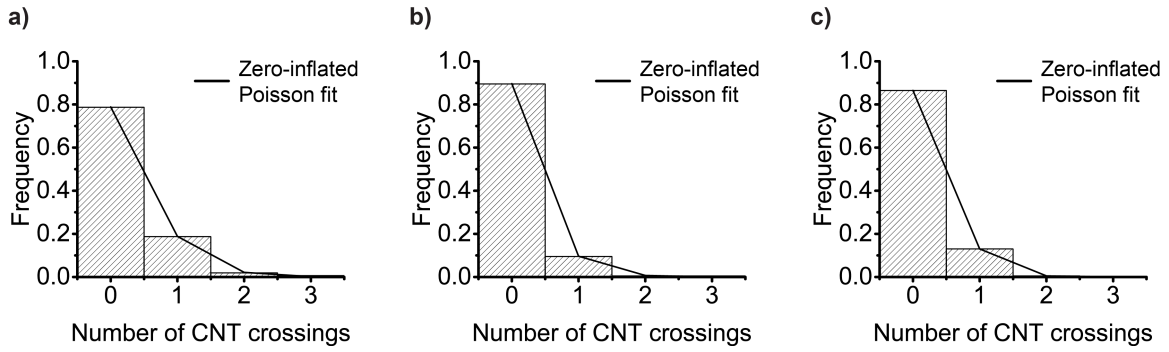

Figure 4.18: Electrode pairs (N > 150) were imaged with SEM on three separate fabricated samples, each with 0.05 CNTs/μm^2 deposited. Zero-inflated Poisson fits were used for each nanotube distribution.

4.5.4 Electrical Characterization

All devices identified by SEM show appreciable current levels in the single to tens of nA range. The transport characteristics (I_{sd}–V_{bg}) of different devices tend to be heavily p-type and have similar conductance levels, as evidenced in Figure 4.19. Note that I_{sd} (as opposed to I_{ds}) is used to match the nomenclature used for p-type MOSFETs.

The homogeneity of nanotubes from chirality-based sorting with conjugated polymers [107] is evident in these electrical measurements. This standardization of electronic properties is crucial for scalability of this platform to larger electrode arrays, such as an active CMOS array, where mitigating device-to-device variability is desired.

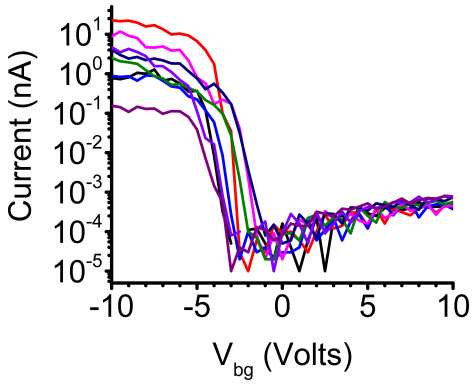

Figure 4.19: Back-gated I-V measurements in air for eight representative single-crossing nanotube devices, with the silicon back-gate swept from –10 V to 10 V and a constant V_{sd} of 200 mV.

However, compared to spin-cast nanotubes from aqueous suspension, the maximum

current levels of the devices made from nanotubes in organic solvent are substantially lower. This may indicate improper electrical contact.

4.5.5 Electrical Sorting of Single-, Double-, and Triple-Nanotube Crossings

Once the polymer-wrapped nanotubes are contacted by electrode metal (Ti), gate metal (Pt) is deposited, and devices are annealed in vacuum, liquid-gated I-V curves are measured in alkaline 100 mM phosphate buffer (pH 8.0), as depicted in Figure 4.20a. Here, we use a fixed source drain bias (V_{sd} = 100 mV) and sweep the solution gate (V_{lg}, relative to the source potential) from –0.5 to 0.5 V on both platinum gate electrodes, which are electrically shorted together.

With electrical measurements alone, it is possible to differentiate between single, double, and triple nanotube crossings. Oftentimes, the constant-current method [108] is used to select the value of I_{sd} at a specific overdrive voltage, $V_{ov} = V_{lg} - |V_{th}|$, where the threshold voltage $|V_{th}|$ becomes the relevant sorting metric for devices. Due to its simplicity – only one current value needs to be chosen – this approach is appealing in industrial semiconductor fabrication lines, where many wafers need to be processed and quickly characterized. However, since this technique relies on an arbitrary choice of overdrive voltage, we instead use the transconductance ($g_m = \partial I_{sd} / \partial V_{lg}$) in the triode regime, where g_m is expected to be proportional to the number of nanotubes and relatively insensitive to V_{lg}, as a well-defined sorting metric to differentiate the number of nanotube crossings. The peak transconductance for each device is extracted from the slope of the line tangent to the linear portion of the corresponding I-V sweep.

For each device in Figure 4.20a, corresponding transconductances are shown in Figure 4.20b. The distribution of peak transconductances are shown in Figure 4.20c for devices characterized (with electron microscopy) as trapping one, two, and three nanotubes between electrode pairs. In the plots shown in 4.20c, it is possible to declare devices with transconductances of less than 50 nS to be single-nanotube devices.

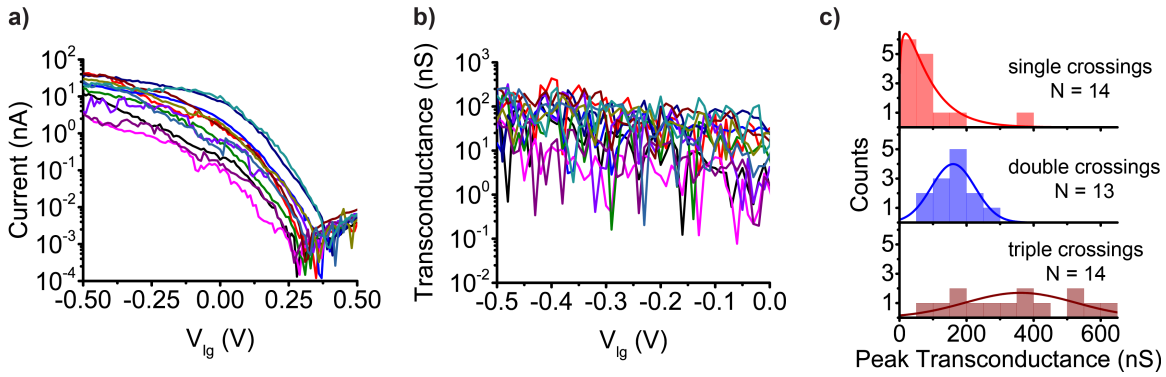

Figure 4.20: a) Solution-gated I-V measurements for twelve representative single-crossing nanotube devices, with the platinum solution gate swept from –0.5 V to 0.5 V and a constant V_{sd} of 200 mV. b) Transconductance values in nS for the same twelve devices. The x-axis of the graphic is clipped to 0 V, since peak transconductances are reached at negative V_{lg} values and most of the devices turn 'off' at more positive values. c) Histograms of peak transconductances for single-, double-, and triple-crossings. Single-crossings are fit to a gamma distribution (solid red line), while both double- and triple-crossings are fit to normal distributions (solid blue and green lines, respectively).

While large variances are observed (for these modest sample sizes) which increase with the number of tubes (as expected), we are confident we can electronically screen for single-nanotube crossings by using the proposed screening method. This type of electrical sorting could by useful for the first round of electrical testing on an active (CMOS) substrate, where candidate smFETs could be quickly identify candidate smFETs.

4.5.6 2" Wafer Assessment

We adapted our spin-cast recipe for depositing polymer-wrapped nanotubes on the surface of 2"–diameter Si/SiO_2 wafers. Each wafer contains at least twelve 1×1 cm^2 reticles (Figure 4.21). We collected SEM images as a function of distance from the primary wafer flat at 52 representative spots on the wafer (26 in a vertical line and 26 in a horizontal line). Figure 4.22 shows a color map associated with the nanotube density in a horizontal and vertical line across a 2" wafer when nanotubes are spun at a concentration of 200 ng/mL. In comparison to the density calculated (0.05 CNTs/μm^2) for the same nanotube concentration spun previously on 1×1 cm^2 samples, the density on the wafers is consistent, having a mean of 0.07 ± 0.01 CNTs/μm^2.

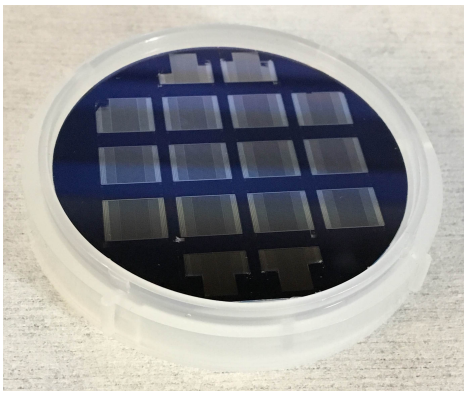

Figure 4.21: Photograph of fully processed 2" wafer, comprised of 12 individual 1×1 cm^2 chips/die.

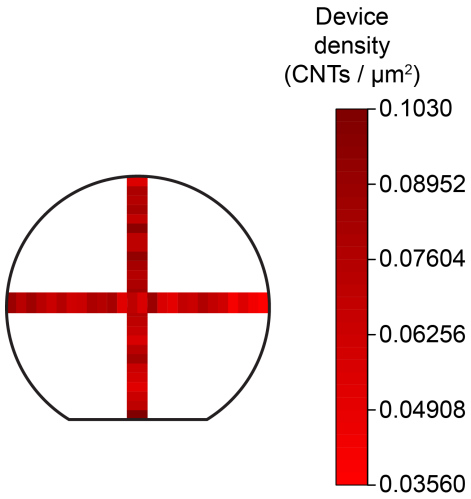

Figure 4.22: 2" wafer density mapping. Twenty-six SEM images are collected starting at the bottom wafer edge and moving north along the wafer. The wafer is rotated 90°, and 26 new images are collected.

4.5.7 Thermodynamic Study

Similar to the studies conducted in Section 4.4.3, thermodynamic measurements are performed on spin-cast smFETs fabricated from CNTs suspended in DCB (see Figure 4.23).

Control measurements are shown in Figure 4.24, showing no reliable two-state RTN-like behavior at any solution bias.

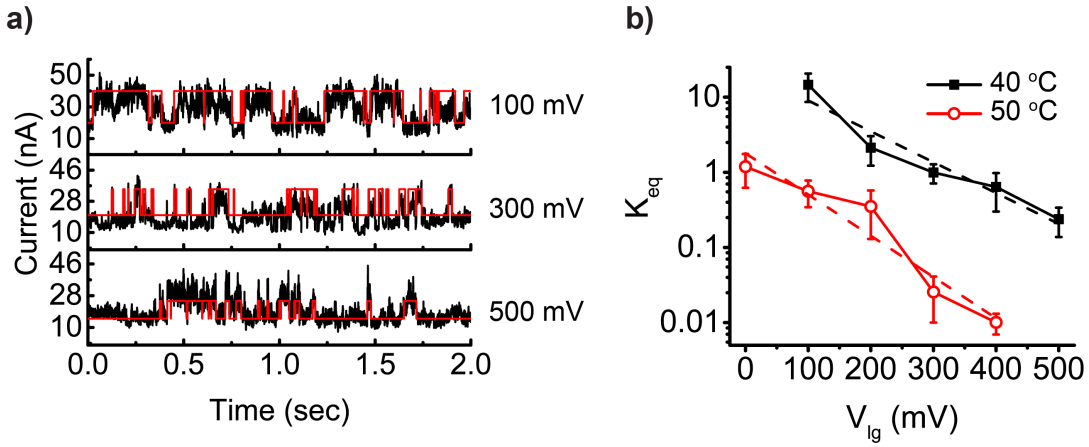

Figure 4.23: spincast smFET thermodynamic measurements with electrostatic control. a) Transient recordings at 3 distinct bias points: 100, 300, and 500 mV. These recordings are from one device measured with a matrix of conditions (five bias points, two temperatures). b) Equilibrium constant K_{eq} as a function of positive solution gate bias for two different temperatures. The black curve (40 °C) shows higher rates than the red curve (50 °C) across the swept range, since at the lower temperature, the DNA duplex needs more energy to melt.

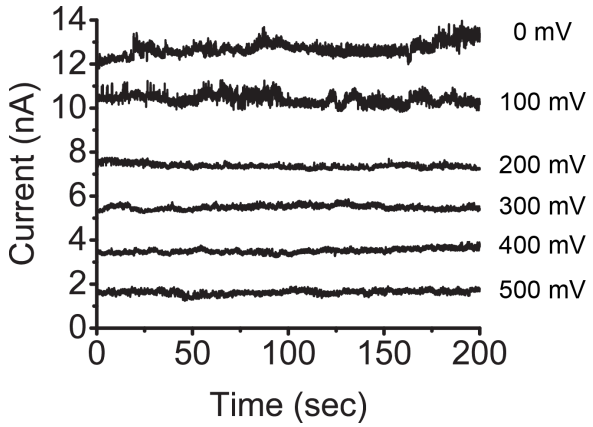

Figure 4.24: spincast smFET control measurements with electrostatic control over a positive solution bias range (0 to 500 mV). Plots are offset for viewing clarity.

4.6 In-house Preparation of Polymer-wrapped, Chiral-sorted SWCNTs

Rather than rely on commercially available SWCNTs in one organic solvent (typically toluene), we attempted to prepare suspensions of polymer-wrapped nanotubes in various organic solvents. Preparation protocols involve two main steps: sonication (to forcefully break apart nanotube agglomerates), and centrifugation (to sort heavy particulates from individual SWCNTs, which have a lower mass). Tip sonicators are preferred to bath sonicators because the ultrasonic power is applied more locally to the solution. Power levels depend on the solvent's viscosity and concentration, among other factors. After centrifugation, the supernatant is collected and either used as-is or diluted in an organic solvent. Typical organic solvents include chloroform, N-Methyl-2-pyrrolidone (NMP), dimethylformamide (DMF), and toluene. According to Bahr et al., SWCNTs are soluble in the first three solvents at room temperature at concentrations exceeding 1 mg/mL [103]. Yet, in toluene, un-derivatized SWCNTs (i.e. pristine SWCNTs, which do not contain artificially induced defect sites along the sidewalls) are insoluble at reasonable concentrations and thus require polymers to improve their solubility.

Conjugated polymers are prevalent for this purpose. Via wrapping with π-conjugated polymers [109, 110, 111], semiconducting single-walled CNTs with specific chiral indices are preferentially extracted [93] from organic solvents; metallic SWCNTs are not affected in the same way. One main family of polymer for this extraction process is polyfluorene (PFO) and associated variants (refer to Figure 4.25). Various alkyl chain lengths have been tested with, ranging from PF6 (6 carbon atoms) to PF18 (18 carbon atoms). In the past, only small-diameter nanotubes (0.8–1.2 nm) were able to be separated, but recent advances have shown efficiency in extracting large-diameter (>1.3 nm) SWCNTs through the use of long alkyl chains (>15 carbon atoms).

Aqueous nanotube suspensions can be prepared as well – typically with surfactants such as sodium dodecyl sulfate (SDS) [112], anionic sodium dodecylbenzenesulfonate (SDBS

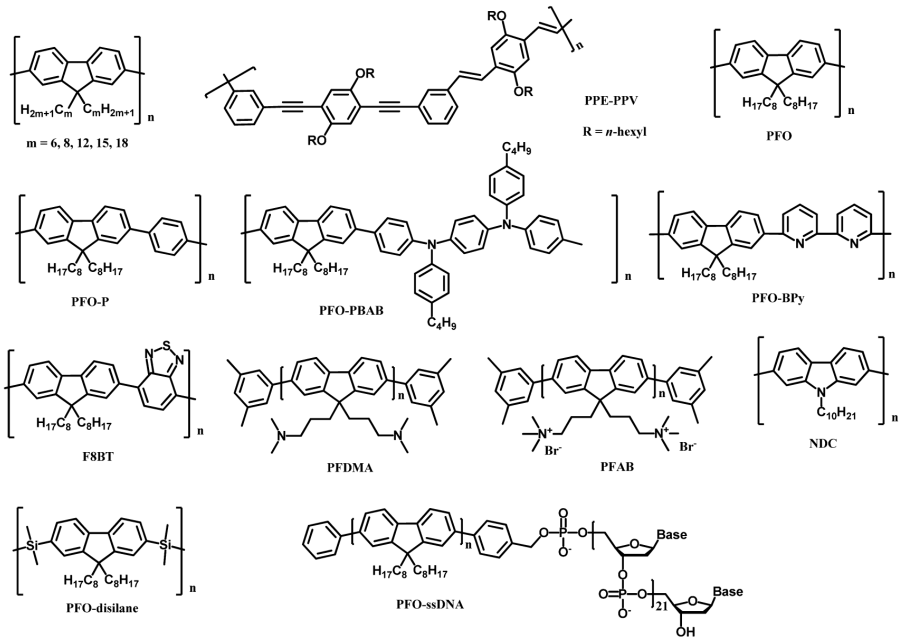

Figure 4.25: Semiconducting SWCNT sorting via PFO and other conjugated polymers. Reproduced from [109].

or NaDDBS) [113], or sodium cholate (SC) [114] to enhance solubility. Polymer-wrapped solutions tend to yield nearly homogeneous chiral populations. In general, the polymer-to-solvent ratio of polymer-wrapped suspensions is less than the surfactant-to-water ratio.

4.7 Enhancements to This Study

Efforts to expand the spin-cast scheme to 300-mm wafers with a semiconductor foundry are ongoing. This transition entails further optimization of solution concentration, solution volume, and wafer pre-treatment conditions.

Further enhancements to this study include:

- Modifying fabrication steps to enhance baseline conductance levels
- Increasing the sensor count per fabricated chip
- Increasing the number of chips by refining process flows for 4" wafer-scale fabrication
- If wafer pre-treatment with oxygen plasma becomes impractical for 300-mm wafers, other adhesion strategies will be explored. One such approach is chemical modification

of the SiO_2 wafer surface before spin-casting with 1% or 2% 3-(Aminopropyl)triethoxysilane (APTES), a small molecule which forms a self-assembled monolayer (SAM) on silicon-based surfaces [115] and renders them functionalized for nanotubes to stick to [89].

4.8 Spin-cast Summary

In conclusion, we have presented a foundry-compatible fabrication process for creating single-molecule field-effect transistors from a suspension of single-walled CNTs in either DI water or a mixture of toluene and 1,2-dichlorobenzene. We have verified that these devices operate as single-molecule transducers with localized charge sensitivity in the vicinity of a generated sidewall defect by extracting thermodynamic behavior as a function of temperature and solution bias. This is the first known demonstration of single-molecule sensing with individually contacted spin-cast nanotubes. Uniform spin-coating is achieved on 4" wafer. While our fabrication currently focuses on smFET arrays formed on passive Si/SiO2 substrates, this approach can be applied to fabrication in the far-back-end of a CMOS process flow, displacing more difficult fabrication approaches used to co-integrate smFET devices and CMOS electronics [34], and paving the way for large-scale manufacturing of smFET CMOS arrays for genomic identification.

Chapter 5

Summary

In conclusion, we have demonstrated single-molecule sensing of probe-target DNA-DNA interactions using customized carbon nanotube field-effect transistors. We have further elucidated the utility of a real-time, multiplexed data acquisition platform capable of detecting sequential hybridization and melting events from as many as 58 smFET devices with 40 μs temporal resolution. From the work presented in Chapters 3 and 4, there is substantial evidence that these smFETs are suited for studying single-molecule dynamics over long timescales. Rapid prototyping of smFET devices can occur due to the transition to wafer-scale production.

5.1 Future Work

Future work is warranted in many areas. In terms of measurement electronics, the measurement parasitics can be improved, as the solution capacitance remains fairly high. One improvement would be to passivate the Schottky barriers, which are highly sensitive interfaces of the nanotube to the contact metal (Ti), with PMMA, thereby protecting the electrodes from coupling to the solution above them. Ideally, the PMMA layer should remain intact. In all of the studies presented, the PMMA was removed via heating on a hotplate after the diazonium reaction, but that step is not mandatory – especially if the experimental electrolytes will only be aqueous (non-organic). With this refinement, only 30

nm along the axis of the nanotube would be exposed to the electrolyte, thereby mitigating non-specific adsorption and extraneous biomolecular interactions during single-molecule experiments.

The software can certainly be improved, especially in terms of calibrating the offset potentials of each measurement channel. Improper tuning of the source and drain DACs will generate a substantial erroneous current. For low current (single nA) devices, making this change is critical, since the error represents a relatively large fraction of the baseline device current.

On-chip temperature sensing should be accomplished. As alluded to in Section 2.4, RTDs were fabricated and roughly calibrated, but they were never implemented in DNA sensing experiments. More extensive calibration is justified.

More streamlined data analysis protocols should be implemented. Although I am satisfied with the existing algorithms I have coded, more effort is needed to benchmark the iterative detection algorithm and understanding its fundamental limits as an analysis tool. At a certain point, the SNR of an smFET real-time recording will be prohibitively low, precluding idealized trace fitting and subsequent kinetic rate extraction. With enough devices, and in future iterations of the measurement platform, these low-SNR devices can be omitted from any analysis routine.

Regulated functionalization schemes need to be developed. It would be nice to avoid using PMMA nanowells, which likely leave a SWCNT sidewall coated with residual polymer due to the lack of annealing post-development.

The dynamics and kinetics of DNA association/dissociation should be further scrutinized. The set of devices (either CVD-grown or spin-cast) which have shown reliable two-state RTN due to successive DNA hybridization/melting events is small. We have recently taken steps to fabricate smFETs on 4" wafers by streamlining the fabrication approach, as discussed in Chapter 4, with the ultimate goal being to enhance device throughput.

Low-concentration studies are imminent. Such studies will help unravel the limit of detection (LOD) of an smFET. The capture rate (M^{-1} s^{-1}) is concentration dependent,

where one can assume a linear relationship between the kinetic rate and the concentration. At low (sub-nM) target concentrations, the measurement time must be considerably increased to allow for ample event transitions. It is possible that a consensus needs to be formed amongst the device population to collect statistics over these long recording times. Improved data analysis algorithms are particularly critical, possibly involving in-line analysis while data is piped from the FPGA memory to the PC.

5.2 Publications

As a result of this work, I have co-authored the following journal publications, in chronological order:

1. D. Bouilly, J. Hon, N. S. Daly, S. Trocchia, S. Vernick, J. Yu, S. Warren, Y. Wu, R. L. Gonzalez, Jr., K. L. Shepard, C. Nuckolls, Single-Molecule Reaction Chemistry in Patterned Nanowells, *Nano Letters* (2016)

2. S. Vernick, S. M. Trocchia, S. B. Warren, E. F. Young, D. Bouilly, R. L. Gonzalez, Jr., C. Nuckolls, K. L. Shepard, Electrostatic melting in a single-molecule field-effect transistor with applications in genomic identification, *Nature Communications* (2017)

    - This work contributed heavily to the text in Chapter 3.

Bibliography

[1] S. Iijima, "Helical microtubules of graphitic carbon," *Nature*, vol. 354, no. 6348, pp. 56–58, 1991.

[2] M. F. L. De Volder, S. H. Tawfick, R. H. Baughman, and A. J. Hart, "Carbon Nanotubes: Present and Future Commercial Applications," *Science*, vol. 339, no. 6119, 2013.

[3] A. Eatemadi, H. Daraee, H. Karimkhanloo, M. Kouhi, N. Zarghami, A. Akbarzadeh, M. Abasi, Y. Hanifehpour, and S. W. Joo, "Carbon nanotubes: properties, synthesis, purification, and medical applications." *Nanoscale Research Letters*, vol. 9, no. 1, p. 393, 2014.

[4] M. Rahmandoust and M. R. Ayatollahi, *Characterization of Carbon Nanotube Based Composites under Consideration of Defects*, ser. Advanced Structured Materials. Springer International Publishing, 2015.

[5] M. J. O'Connell, *Carbon nanotubes: properties and applications.* CRC/Taylor & Francis, 2006, vol. 43, no. 19.

[6] J.-Y. Park, "Band Structure and Electron Transport Physics of One-Dimensional SWNTs," in *Carbon Nanotube Electronics*, 2009, pp. 1–42.

[7] T. Wang Odom, J.-L. Huang, and C. M. Lieber, "Single-Walled Carbon Nanotubes From Fundamental Studies to New Device Concepts," *Ann. N.Y. Acad. Sci*, vol. 960, pp. 203–215, 2002.

[8] M. J. Biercuk, S. Ilani, C. M. Marcus, and P. L. McEuen, *Electrical Transport in Single-Wall Carbon Nanotubes.* Berlin, Heidelberg: Springer Berlin Heidelberg, 2008, pp. 455–493.

[9] S. A. Hodge, M. K. Bayazit, K. S. Coleman, and M. S. P. Shaffer, "Unweaving the rainbow: a review of the relationship between single-walled carbon nanotube molecular structures and their chemical reactivity," *Chemical Society Reviews*, vol. 41, no. 12, p. 4409, 2012.

[10] N. Yang, X. Chen, T. Ren, P. Zhang, and D. Yang, "Carbon nanotube based biosensors," *Sensors and Actuators B: Chemical*, vol. 207, pp. 690–715, 2015.

[11] A. Star, E. Tu, J. Niemann, J.-c. P. Gabriel, C. S. Joiner, and C. Valcke, "Label-free detection of DNA hybridization using carbon nanotube network field-effect transistors," *Proceedings of the National Academy of Sciences of the United States of America*, vol. 103, no. 4, pp. 921–926, 2006.

[12] A. Star, J.-C. P. Gabriel, K. Bradley, and G. Grüner, "Electronic Detection of Specific Protein Binding Using Nanotube FET Devices," *Nano Letters*, vol. 3, no. 4, pp. 459–463, 2003.

[13] B. Veigas, E. Fortunato, and P. Baptista, "Field Effect Sensors for Nucleic Acid Detection: Recent Advances and Future Perspectives," *Sensors*, vol. 15, no. 5, pp. 10 380–10 398, 2015.

[14] T. Sharf, J. W. Kevek, T. DeBorde, J. L. Wardini, and E. D. Minot, "Origins of Charge Noise in Carbon Nanotube Field-Effect Transistor Biosensors," *Nano Letters*, vol. 12, no. 12, pp. 6380–6384, 2012.

[15] E. Katz and I. Willner, "Integrated Nanoparticle-Biomolecule Hybrid Systems: Synthesis, Properties, and Applications," *Angewandte Chemie International Edition*, vol. 43, no. 45, pp. 6042–6108, 2004.

[16] W. Yang, P. Thordarson, J. J. Gooding, S. P. Ringer, and F. Braet, "Carbon nanotubes for biological and biomedical applications," *Nanotechnology*, vol. 18, no. 41, p. 412001, 2007.

[17] D. Tasis, N. Tagmatarchis, A. Bianco, and M. Prato, "Chemistry of carbon nanotubes," pp. 1105–1136, 2006.

[18] B. R. Goldsmith, J. G. Coroneus, V. R. Khalap, A. A. Kane, G. A. Weiss, and P. G. Collins, "Conductance-controlled point functionalization of single-walled carbon nanotubes," *Science*, vol. 315, no. 5808, pp. 77–81, 2007.

[19] M. S. Strano, C. A. Dyke, M. L. Usrey, P. W. Barone, M. J. Allen, H. Shan, C. Kittrell, R. H. Hauge, J. M. Tour, and R. E. Smalley, "Electronic Structure Control of Single-Walled Carbon Nanotube Functionalization," *Science*, vol. 301, no. 5639, pp. 1519–1522, 2003.

[20] J. Gavrilyuk, H. Ban, M. Nagano, W. Hakamata, and C. F. Barbas, "Formylbenzene Diazonium Hexafluorophosphate Reagent for Tyrosine-Selective Modification of Proteins and the Introduction of a Bioorthogonal Aldehyde," *Bioconjugate Chemistry*, vol. 23, no. 12, pp. 2321–2328, 2012.

[21] C.-S. Lee, S. E. Baker, M. S. Marcus, W. Yang, M. A. Eriksson, and R. J. Hamers, "Electrically Addressable Biomolecular Functionalization of Carbon Nanotube and Carbon Nanofiber Electrodes," *Nano Letters*, vol. 4, no. 9, pp. 1713–1716, 2004.

[22] N. Nair, W.-J. Kim, M. L. Usrey, and M. S. Strano, "A Structure-Reactivity Relationship for Single Walled Carbon Nanotubes Reacting with 4-Hydroxybenzene Diazonium Salt," *Journal of the American Chemical Society*, vol. 129, no. 13, pp. 3946–3954, 2007.

[23] H. Wilson, S. Ripp, L. Prisbrey, M. A. Brown, T. Sharf, D. J. T. Myles, K. G. Blank, and E. D. Minot, "Electrical monitoring of sp3 defect formation in individual carbon nanotubes," *The Journal of Physical Chemistry C*, vol. 120, no. 3, pp. 1971–1976, jan 2016.

[24] R. J. Chen, Y. Zhang, and D. Wang, "Noncovalent Sidewall Functionalization of Single-Walled Carbon Nanotubes for Protein Immobilization," *Journal of the American Chemical Society*, vol. 123, no. 16, pp. 3838–3839, 2001.

[25] T. J. Olsen, Y. Choi, P. C. Sims, O. T. Gul, B. L. Corso, C. Dong, W. A. Brown, P. G. Collins, and G. A. Weiss, "Electronic measurements of single-molecule processing by DNA polymerase I (Klenow Fragment)," *Journal of the American Chemical Society*, vol. 135, no. 21, pp. 7855–7860, 2013.

[26] Y. Choi, I. S. Moody, P. C. Sims, S. R. Hunt, B. L. Corso, I. Perez, G. A. Weiss, and P. G. Collins, "Single-Molecule Lysozyme Dynamics Monitored by an Electronic Circuit," *Science*, vol. 335, no. 6066, pp. 319–324, 2012.

[27] R. Haddad, M. Holzinger, A. Maaref, and S. Cosnier, "Pyrene functionalized single-walled carbon nanotubes as precursors for high performance biosensors," *Electrochimica Acta*, vol. 55, no. 27, pp. 7800–7803, 2010.

[28] D. E. Makarov, "The Kinetics of Chemical Reactions: Single-Molecule Versus "Bulk" View," *Single Molecule Science*, pp. 19–28, 2015.

[29] I. Tinoco and R. L. Gonzalez, "Biological mechanisms, one molecule at a time." *Genes & Development*, vol. 25, no. 12, pp. 1205–31, 2011.

[30] J. Rosenstein, S. Sorgenfrei, and K. L. Shepard, "Noise and bandwidth performance of single-molecule biosensors," pp. 1–7, 2011.

[31] R. Roy, S. Hohng, and T. Ha, "A Practical Guide to Single Molecule FRET," *Nature Methods*, vol. 5, no. 6, pp. 507–516, 2008.

[32] S. Sorgenfrei, C.-y. Chiu, R. L. Gonzalez, Y.-J. Yu, P. Kim, C. Nuckolls, and K. L. Shepard, "Label-free single-molecule detection of DNA-hybridization kinetics with a carbon nanotube field-effect transistor." *Nature Nanotechnology*, vol. 6, no. 2, pp. 126–32, 2011.

[33] Y. Choi, T. J. Olsen, P. C. Sims, I. S. Moody, B. L. Corso, M. N. Dang, G. A. Weiss, and P. G. Collins, "Dissecting Single-Molecule Signal Transduction in Carbon Nanotube Circuits with Protein Engineering," *Nano Letters*, vol. 12, no. 2, pp. 625–631, 2013.

[34] S. B. Warren, S. Vernick, E. Romano, and K. L. Shepard, "Complementary Metal-Oxide-Semiconductor Integrated Carbon Nanotube Arrays: Toward Wide-Bandwidth Single-Molecule Sensing Systems," *Nano Letters*, vol. 16, no. 4, pp. 2674–2679, 2016.

[35] S. J. Holden, S. Uphoff, J. Hohlbein, D. Yadin, L. Le Reste, O. J. Britton, and A. N. Kapanidis, "Defining the Limits of Single-Molecule FRET Resolution in TIRF Microscopy," *Biophysical Journal*, vol. 99, no. 9, pp. 3102–3111, 2010.

[36] T. E. Ouldridge, P. Sulc, F. Romano, J. P. K. Doye, and A. A. Louis, "DNA hybridization kinetics: zippering, internal displacement and sequence dependence," *Nucleic Acids Research*, vol. 41, no. 19, pp. 8886–8895, 2013.

[37] X. Zhang, D. C. Kim, J. Yujizhou, T. N. Hone, D. Chenet, B. Kim, J. Yu, J. Tang, C. Nuckolls, and J. Hone, "Fabrication of hundreds of field effect transistors on a single carbon nanotube for basic studies and molecular devices," *Journal of Vacuum Science & Technology B, Nanotechnology and Microelectronics: Materials, Processing, Measurement, and Phenomena*, vol. 31, p. 06FI01, 2013.

[38] A. Arun, P. Salet, and A. M. Ionescu, "A Study of Deterministic Positioning of Carbon Nanotubes by Dielectrophoresis," *Journal of Electronic Materials*, vol. 38, no. 6, pp. 742–749, 2009.

[39] R. Krupke, F. Hennrich, H. B. Weber, M. M. Kappes, and H. V. Lo, "Simultaneous Deposition of Metallic Bundles of Single-walled Carbon Nanotubes Using Ac-dielectrophoresis," *Nano Letters*, vol. 3, no. 8, pp. 1019–1023, 2003.

[40] S. Sorgenfrei, I. Meric, S. Banerjee, A. Akey, S. Rosenblatt, I. P. Herman, and K. L. Shepard, "Controlled dielectrophoretic assembly of carbon nanotubes using real-time electrical detection," *Applied Physics Letters*, vol. 94, no. 5, 2009.

[41] S. Sorgenfrei and K. Shepard, "Single-Molecule Electronic Detection Using Nanoscale Field-Effect Devices," *2011 48th ACM/EDAC/IEEE Design Automation Conference (DAC)*, pp. 712–717, 2011.

[42] A. Dudina, F. Seichepine, Y. Chen, A. Stettler, A. Hierlemann, and U. Frey, "Switch-matrix-based Monolithic CMOS Platform Featuring a Large Array of Carbon Nanotube Sensor Elements and a 96-channel Readout Circuitry," *Procedia Engineering*, vol. 168, pp. 916–919, 2016.

[43] E. T. McAdams, J. Jossinet, R. Subramanian, and R. G. E. McCauley, "Characterization of gold electrodes in phosphate buffered saline solution by impedance and noise measurements for biological applications," *Annual International Conference of the IEEE Engineering in Medicine and Biology - Proceedings*, pp. 4594–4597, 2006.

[44] A. J. Bard and L. R. Faulkner, *Electrochemical methods: fundamentals and applications*. Wiley, 2001.

[45] M. Pachchigar, "Design Considerations for a Transimpedance Amplifier," pp. 1–6, 2008.

[46] E. S. Snow, J. P. Novak, M. D. Lay, and F. K. Perkins, "1/f Noise in Single-Walled Carbon Nanotube Devices," *Applied Physics Letters*, vol. 85, no. 18, pp. 4172–4174, 2004.

[47] J. SantaLucia and D. Hicks, "The thermodynamics of DNA structural motifs," *Annual Review of Biophysics and Biomolecular Structure*, vol. 33, no. 1, pp. 415–440, 2004.

[48] Q. Wang and W. E. Moerner, "Single-molecule motions enable direct visualization of biomolecular interactions in solution," *Nature Methods*, vol. 11, no. 5, pp. 555–8, 2014.

[49] N. F. Dupuis, E. D. Holmstrom, and D. J. Nesbitt, "Single-Molecule Kinetics Reveal Cation-Promoted DNA Duplex Formation Through Ordering of Single-Stranded Helices," *Biophysj*, vol. 105, no. 3, pp. 756–766, 2013.

[50] J. S. Schreck, T. E. Ouldridge, F. Romano, P. Šulc, L. P. Shaw, A. A. Louis, and J. P. K. Doye, "DNA hairpins destabilize duplexes primarily by promoting melting rather than by inhibiting hybridization," *Nucleic Acids Research*, vol. 43, no. 13, pp. 6181–6190, 2015.

[51] K. Marimuthu and R. Chakrabarti, "Sequence-dependent theory of oligonucleotide hybridization kinetics," *The Journal of Chemical Physics*, vol. 140, no. 17, p. 175104, 2014.

[52] X. Tang, S. Bansaruntip, N. Nakayama, E. Yenilmez, Y.-l. Chang, and Q. Wang, "Carbon Nanotube DNA Sensor and Sensing Mechanism," *Nano Letters*, vol. 6, no. 8, pp. 1632–1636, 2006.

[53] J. E. Weber, S. Pillai, M. K. Ram, A. Kumar, and S. R. Singh, "Electrochemical impedance-based DNA sensor using a modified single walled carbon nanotube electrode," *Materials Science and Engineering: C*, vol. 31, no. 5, pp. 821–825, 2011.

[54] F. Albertorio, M. E. Hughes, J. A. Golovchenko, and D. Branton, "Base dependent DNA-carbon nanotube interactions: activation enthalpies and assembly-disassembly control," *Nanotechnology*, vol. 20, no. 39, p. 395101, 2009.

[55] J. Mannik, B. R. Goldsmith, A. Kane, and P. G. Collins, "Chemically induced conductance switching in carbon nanotube circuits," *Physical Review Letters*, vol. 97, no. 1, 2006.

[56] S. Sorgenfrei, C. Y. Chiu, C. Nuckolls, and K. L. Shepard, "Charge sensing using point-functionalized carbon nanotube transistors for single-molecule detection," *Proceedings of the 2011 IEEE/NIH Life Science Systems and Applications Workshop, LiSSA 2011*, pp. 63–66, 2011.

[57] E. Papadopoulou, M. Meneghello, P. Marafini, R. P. Johnson, T. Brown, and P. N. Bartlett, "The effect of temperature on electrochemically driven denaturation monitored by SERS," *Bioelectrochemistry*, vol. 106, pp. 353–358, 2015.

[58] R. P. Johnson, R. Gao, T. Brown, and P. N. Bartlett, "The effect of base-pair sequence on electrochemically driven denaturation," *Bioelectrochemistry*, vol. 85, pp. 7–13, 2012.

[59] D. Bouilly, J. Hon, N. S. Daly, S. Trocchia, S. Vernick, J. Yu, S. Warren, Y. Wu, R. L. Gonzalez, K. L. Shepard, and C. Nuckolls, "Single-Molecule Reaction Chemistry in Patterned Nanowells," *Nano Letters*, vol. 16, no. 7, pp. 6–12, 2016.

[60] G. T. Hermanson, *Bioconjugate techniques.* Academic Press, 2008.

[61] M. S. Dresselhaus, G. Dresselhaus, R. Saito, and A. Jorio, "Raman spectroscopy of carbon nanotubes," *Phys. Rep.*, vol. 409, no. 2, p. 47, 2005.

[62] A. Jorio, R. Saito, J. H. Hafner, C. M. Lieber, M. Hunter, T. McClure, G. Dresselhaus, and M. S. Dresselhaus, "Structural (n,m) Determination of Isolated Single-Wall Carbon Nanotubes by Resonant Raman Scattering," *Physical Review Letters*, vol. 86, no. 6, pp. 1118–1121, 2001.

[63] P. L. McEuen, M. S. Fuhrer, and H. Park, "Single-walled carbon nanotube electronics," pp. 78–85, 2002.

[64] C. Plesa and C. Dekker, "Data analysis methods for solid-state nanopores," *Nanotechnology*, vol. 26, no. 8, p. 84003, 2015.

[65] M. Levitus, "Chemical Kinetics at the Single-Molecule Level," *Journal of Chemical Education*, vol. 88, no. 2, pp. 162–166, 2011.

[66] L. Prisbrey, D. Roundy, K. Blank, L. S. Fifield, and E. D. Minot, "Electrical characteristics of carbon nanotube devices prepared with single oxidative point defects," *Journal of Physical Chemistry C*, vol. 116, no. 2, pp. 1961–1965, 2012.

[67] T. Sharf, N.-p. Wang, J. W. Kevek, M. A. Brown, H. Wilson, S. Heinze, and E. D. Minot, "Single Electron Charge Sensitivity of Liquid-Gated Carbon Nanotube Transistors," *Nano Letters*, vol. 14, no. 9, pp. 4925–4930, 2014.

[68] J. Hooyberghs, P. Van Hummelen, and E. Carlon, "The effects of mismatches on hybridization in dna microarrays: determination of nearest neighbor parameters," *Nucleic acids research*, vol. 37, no. 7, pp. e53–e53, 2009.

[69] V. Brabec and E. Paleček, "Interaction of nucleic acids with electrically charged surfaces," *Biophysical Chemistry*, vol. 4, no. 1, pp. 79–92, 1976.

[70] P. Valenta and H. W. Nürnberg, "The electrochemical behaviour of DNA at electrically charged interfaces," *Biophysics of structure and mechanism*, vol. 1, no. 1, pp. 17–26, 1974.

[71] J. Kim and J.-S. Shin, "Probing the Transition State for Nucleic Acid Hybridization Using Φ-Value Analysis," *Biochemistry*, vol. 49, no. 16, pp. 3420–3426, 2010.

[72] H. Eyring, "The Activated Complex in Chemical Reactions," *Journal of Chemical Physics*, vol. 3, pp. 107–115, 1934.

[73] K. J. Laidler and M. C. King, "the Development of Transition-State Theory," pp. 2657–2664, 1983.

[74] H. A. Kramers, "Brownian motion in a field of force and the diffusion model of chemical reactions," *Physica*, vol. 7, no. 4, pp. 284–304, 1940.

[75] E. Evans, "Probing the relation between forcelifetimeand chemistry in single molecular bonds," *Annual review of biophysics and biomolecular structure*, vol. 30, no. 1, pp. 105–128, 2001.

[76] J. Mathé, H. Visram, V. Viasnoff, Y. Rabin, and A. Meller, "Nanopore unzipping of individual DNA hairpin molecules." *Biophysical Journal*, vol. 87, no. 5, pp. 3205–3212, 2004.

[77] J. Nakane, M. Wiggin, and A. Marziali, "A nanosensor for transmembrane capture and identification of single nucleic acid molecules." *Biophys. J.*, vol. 87, no. 1, pp. 615–621, 2004.

[78] A. F. Sauer-Budge, J. A. Nyamwanda, D. K. Lubensky, and D. Branton, "Unzipping kinetics of double-stranded DNA in a nanopore," *Physical Review Letters*, vol. 90, no. 23, p. 238101, 2003.

[79] A. Tikhomirova, I. V. Beletskaya, and T. V. Chalikian, "Stability of DNA Duplexes Containing GG, CC, AA, and TT Mismatches," *Biochemistry*, vol. 45, no. 35, pp. 10 563–10 571, 2006.

[80] D. Axelrod and M. Wang, "Reduction-of-dimensionality kinetics at reaction-limited cell surface receptors," *Biophysical Journal*, vol. 66, no. 3, pp. 588–600, 1994.

[81] V. Chan, D. J. Graves, and S. E. McKenzie, "The biophysics of DNA hybridization with immobilized oligonucleotide probes." *Biophysical Journal*, vol. 69, no. 6, pp. 2243–2255, 1995.

[82] D. Erickson, D. Li, and U. J. Krull, "Modeling of DNA hybridization kinetics for spatially resolved biochips," *Analytical Biochemistry*, vol. 317, no. 2, pp. 186–200, 2003.

[83] J.-L. Sikorav, H. Orland, and A. Braslau, "Mechanism of Thermal Renaturation and Hybridization of Nucleic Acids: Kramers' Process and Universality in Watson-Crick Base Pairing," *The Journal of Physical Chemistry B*, vol. 113, no. 12, pp. 3715–3725, 2009.

[84] C. Nicolai and F. Sachs, "Solving Ion Channel Kinetics with the QuB Software," *Biophysical Reviews and Letters*, vol. 08, no. 03n04, pp. 191–211, 2013.

[85] J. E. Bronson, J. Fei, J. M. Hofman, R. L. Gonzalez, C. H. Wiggins, and et Al., "Learning rates and states from biophysical time series: a Bayesian approach to model selection and single-molecule FRET data." *Biophysical Journal*, vol. 97, no. 12, pp. 3196–205, 2009.

[86] C. Raillon, P. Granjon, M. Graf, L. J. Steinbock, and a. Radenovic, "Fast and automatic processing of multi-level events in nanopore translocation experiments." *Nanoscale*, vol. 4, no. 16, pp. 4916–24, 2012.

[87] S. A. McKinney, C. Joo, and T. Ha, "Analysis of single-molecule FRET trajectories using hidden Markov modeling." *Biophysical Journal*, vol. 91, no. 5, pp. 1941–51, 2006.

[88] L. S. Liyanage, H. Lee, N. Patil, S. Park, S. Mitra, Z. Bao, and H.-S. P. Wong, "Wafer-Scale Fabrication and Characterization of Thin-Film Transistors with Polythiophene-Sorted Semiconducting Carbon Nanotube Networks," *ACS Nano*, vol. 6, no. 1, pp. 451–458, 2012.

[89] C. Wang, J. Zhang, K. Ryu, A. Badmaev, L. G. De Arco, and C. Zhou, "Wafer-scale fabrication of separated carbon nanotube thin-film transistors for display applications," *Nano Letters*, vol. 9, no. 12, pp. 4285–4291, 2009.

[90] G. S. Tulevski, A. D. Franklin, D. Frank, J. M. Lobez, Q. Cao, H. Park, A. Afzali, S.-j. Han, J. B. Hannon, and W. Haensch, "Toward High-Performance Digital Logic Technology with Carbon Nanotubes," *ACS Nano*, vol. 8, no. 9, pp. 8730–8745, 2014.

[91] T. Haeberle, A. M. Munzer, F. Buth, J. Antonio Garrido, A. Abdellah, B. Fabel, P. Lugli, and G. Scarpa, "Solution processable carbon nanotube network thin-film transistors operated in electrolytic solutions at various pH," *Applied Physics Letters*, vol. 101, no. 22, p. 223101, 2012.

[92] J. K. Rosenstein, S. G. Lemay, and K. L. Shepard, "Single-molecule bioelectronics," *Wiley Interdisciplinary Reviews: Nanomedicine and Nanobiotechnology*, vol. 7, no. 4, pp. 475–493, 2015.

[93] M. Tange, T. Okazaki, and S. Iijima, "Selective Extraction of Large-Diameter Single-Wall Carbon Nanotubes with Specific Chiral Indices by Poly(9,9-dioctylfluorene-alt-benzothiadiazole)," *Journal of the American Chemical Society*, vol. 133, no. 31, pp. 11 908–11 911, 2011.

[94] K. S. Mistry, B. A. Larsen, J. L. Blackburn, N. Renewable, U. States, and U. States, "High-Yield Dispersions of Single-Walled Carbon Nanotubes with Tunable Narrow Chirality Distributions," *ACS Nano*, vol. 7, no. 3, pp. 2231–2239, 2013.

[95] S. Park, G. Pitner, G. Giri, J. H. Koo, J. Park, K. Kim, H. Wang, R. Sinclair, H. S. P. Wong, and Z. Bao, "Large-area assembly of densely aligned single-walled carbon nanotubes using solution shearing and their application to field-effect transistors," *Advanced Materials*, vol. 27, no. 16, pp. 2656–2662, 2015.

[96] S. P. Schießl, N. Fröhlich, M. Held, F. Gannott, M. Schweiger, M. Forster, U. Scherf, and J. Zaumseil, "Polymer-sorted semiconducting carbon nanotube networks for high-performance ambipolar field-effect transistors," *ACS Applied Materials and Interfaces*, vol. 7, no. 1, pp. 682–689, 2015.

[97] Q. N. Thanh, H. Jeong, J. Kim, J. Kevek, Y. Ahn, S. Lee, E. D. Minot, and J.-Y. Park, "Transfer-printing of as-fabricated carbon nanotube devices onto various substrates," *Advanced Materials*, vol. 24, no. 33, pp. 4499–4504, 2012.

[98] P. Vichchulada, M. A. Cauble, E. A. Abdi, E. I. Obi, Q. Zhang, and M. D. Lay, "Sonication power for length control of single-walled carbon nanotubes in aqueous suspensions used for 2-dimensional network formation," *The Journal of Physical Chemistry C*, vol. 114, no. 29, pp. 12 490–12 495, 2010.

[99] S. Vernick, S. M. Trocchia, S. B. Warren, E. F. Young, D. Bouilly, R. L. Gonzalez, C. Nuckolls, and K. L. Shepard, "Electrostatic melting in a single-molecule field-effect transistor with applications in genomic identification," *Nature Communications*, vol. 8, p. 15450, 2017.

[100] B. McNally, M. Wanunu, and A. Meller, "Electromechanical unzipping of individual dna molecules using synthetic sub-2 nm pores," *Nano Letters*, vol. 8, no. 10, pp. 3418–3422, 2008.

[101] R. P. Johnson, N. Gale, J. A. Richardson, T. Brown, and P. N. Bartlett, "Denaturation of dsDNA immobilised at a negatively charged gold electrode is not caused by electrostatic repulsion," *Chemical Science*, vol. 4, pp. 1625–1632, 2013.

[102] C. Steger, "An Unbiased Detector of Curvilinear Structures," *IEEE Trans. Pattern Anal. Mach. Intell.*, vol. 20, no. 2, pp. 113–125, 1998.

[103] J. L. Bahr, E. T. Mickelson, M. J. Bronikowski, R. E. Smalley, and J. M. Tour, "Dissolution of small diameter single-wall carbon nanotubes in organic solvents?" *Chemical Communications*, no. 2, pp. 193–194, 2001.

[104] S. B. Fagan, A. G. Souza Filho, J. O. G. Lima, J. Mendes Filho, O. P. Ferreira, I. O. Mazali, O. L. Alves, and M. S. Dresselhaus, "1,2-Dichlorobenzene interacting with carbon nanotubes," *Nano Letters*, vol. 4, no. 7, pp. 1285–1288, 2004.

[105] S. Niyogi, M. a. Hamon, D. E. Perea, C. B. Kang, B. Zhao, S. K. Pal, a. E. Wyant, M. E. Itkis, and R. C. Haddon, "Ultrasonic Dispersions of Single-Walled Carbon Nanotubes," *Journal of Physical Chemistry B*, vol. 107, no. 34, pp. 8799–8804, 2003.

[106] F. Hennrich, R. Krupke, S. Lebedkin, K. Arnold, R. Fischer, D. E. Resasco, and M. M. Kappes, "Raman Spectroscopy of Individual Single-Walled Carbon Nanotubes from Various Sources," *Journal of Physical Chemistry B*, vol. 109, pp. 10 567–10 573, 2005.

[107] J. Ding, Z. Li, J. Lefebvre, F. Cheng, J. L. Dunford, P. R. L. Malenfant, J. Humes, and J. Kroeger, "A hybrid enrichment process combining conjugated polymer extraction and silica gel adsorption for high purity semiconducting single-walled carbon nanotubes (SWCNT)," *Nanoscale*, vol. 7, no. 38, pp. 15 741–15 747, 2015.

[108] A. Ortiz-Conde, F. J. García Sánchez, J. J. Liou, A. Cerdeira, M. Estrada, and Y. Yue, "A review of recent MOSFET threshold voltage extraction methods," pp. 583–596, 2002.

[109] W. Gomulya, G. D. Costanzo, E. J. F. de Carvalho, S. Z. Bisri, V. Derenskyi, M. Fritsch, N. Frhlich, S. Allard, P. Gordiichuk, A. Herrmann, S. J. Marrink, M. C. dos Santos, U. Scherf, and M. A. Loi, "Semiconducting single-walled carbon nanotubes on demand by polymer wrapping," *Advanced Materials*, vol. 25, no. 21, pp. 2948–2956, 2013.

[110] W. Gomulya, J. Gao, M. A. Loi *et al.*, "Conjugated polymer-wrapped carbon nanotubes: physical properties and device applications," *Eur. Phys. J. B*, vol. 86, no. 10, pp. 1–13, 2013.

[111] S. K. Samanta, M. Fritsch, U. Scherf, W. Gomulya, S. Z. Bisri, and M. A. Loi, "Conjugated polymer-assisted dispersion of single-wall carbon nanotubes: the power of polymer wrapping," *Accounts of chemical research*, vol. 47, no. 8, pp. 2446–2456, 2014.

[112] L. Vaisman, H. D. Wagner, and G. Marom, "The role of surfactants in dispersion of carbon nanotubes," *Advances in colloid and interface science*, vol. 128, pp. 37–46, 2006.

[113] K. Yang, Z. Yi, Q. Jing, R. Yue, W. Jiang, and D. Lin, "Sonication-assisted dispersion of carbon nanotubes in aqueous solutions of the anionic surfactant sdbs: The role of sonication energy," *Chinese Science Bulletin*, vol. 58, no. 17, pp. 2082–2092, 2013.

[114] J. G. Clar, S. A. Gustitus, S. Youn, C. A. Silvera Batista, K. J. Ziegler, and J. C. J. Bonzongo, "Unique toxicological behavior from single-wall carbon nanotubes separated via selective adsorption on hydrogels," *Environmental science & technology*, vol. 49, no. 6, pp. 3913–3921, 2015.

[115] R. M. Pasternack, S. Rivillon Amy, and Y. J. Chabal, "Attachment of 3-(aminopropyl) triethoxysilane on silicon oxide surfaces: dependence on solution temperature," *Langmuir*, vol. 24, no. 22, pp. 12 963–12 971, 2008.